Dissertation zur Erlangung des Doktorgrades
der Fakultät für Chemie und Pharmazie
der Ludwig-Maximilians-Universität München

Synthesis, Characterization and DFT Analysis of Stable {FeNO}^{7} Compounds

Bianca Maria Aas

aus

Gräfelfing, Deutschland

2018

Erklärung

Diese Dissertation wurde im Sinne von § 7 der Promotionsordnung vom 28. November 2011 von Herrn Prof. Dr. Peter Klüfers betreut.

Eidesstattliche Versicherung

Diese Dissertation wurde eigenständig und ohne unerlaubte Hilfe erarbeitet.

München, den 29.05.2018

Bianca Maria Aas

Dissertation eingereicht am 19.02.2018

1. Gutachter: Prof. Dr. Peter Klüfers

2. Gutachter: Prof. Dr. Hans-Christian Böttcher

Mündliche Prüfung am 20.04.2018

Diese Arbeit wurde in der Zeit von Mai 2014 bis Februar 2018 am Department für Chemie der Ludwig-Maximilians-Universität München am Lehrstuhl für Bioanorganische Chemie und Koordinationschemie unter Anleitung von Herrn Prof. Dr. Peter Klüfers durchgeführt.

Table of Contents

List of Figures

List of Tables

List of Schemes

Abbreviations and Conventions

ATR	attenuated total reflection
bs	broken symmetry
calcd	calculated
CDA	charge decomposition analysis
cGKs	cGMP-dependent protein kinases
cGMP	cyclic guanosine monophosphate
COSMO	conductor-like screening model
COSMO-RS	conductor-like screening model for real solvents
DFT	density functional theory
DMF	*N,N*-dimethylformamide
DOS	density of states
eNOS	endothelial nitric oxide synthase
Exp	experiment
FAB	fast atom bombardment
FO	fragment orbital
GTP	guanosine triphosphate
Hb	desoxy-hemoglobin
HOMO	highest occupied molecular orbital
iNOS	inducible nitric oxide synthase
IR	infrared
L	ligand
LUMO	lowest unoccupied molecular orbital
m	medium
Me	methyl
MO	molecular orbital
MPA	mulliken population analysis
MS	mass spectrometry
NADPH	nicotinamide adenine dinucleotide phosphate

NMR	nuclear magnetic resonance
nNOS	neuronal nitric oxide synthase
NORs	nitric oxide reductases
NOS	nitric oxide synthase
NPA	natural population analysis
OC-6	octahedron (IUPAC polyhedral symbol)
Tf	trifluoromethylsulfonyl
PDEs	phosphodiesterases
ppm	parts per million
QTAIM	quantum theory of atoms in molecules
RNS	reactive nitrogen species
rt	room temperature
s	strong
sGC	soluble guanylate cyclase
TD-DFT	time dependent density functional theory
TEA	triethylamine
THF	tetrahydrofuran
UV/VIS	ultraviolet-visible
$\tilde{\nu}$	wavenumber
vs	very strong
vw	very weak
w	weak
δ	chemical shift

- The octahedrally coordinated complex compounds are named according to the IUPAC convention.[1]
- All complex compounds are visualized with the same color code: iron atoms are drawn in orange, oxygen atoms in red, nitrogen atoms in blue, carbon atoms in gray and hydrogen atoms in white.
- The hydrogen-bond pattern of the crystal structures is described with the descriptors $R_d^a(n)$ as defined by graph-set analysis.[2,3] The number of atoms *n* involved in the respective ring pattern is specified in parentheses. The number of hydrogen-bond donors is given in the subscript (*d*) and the number of hydrogen-bond acceptors is given in superscript (*a*).
- The canonical molecular orbitals of the nitrosyl-iron compounds are analyzed using the following coordinate system: the z-axis is defined along the Fe–N vector of the Fe–N–O moiety.

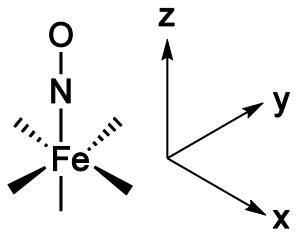

Overview of chelating ligands and their abbreviations

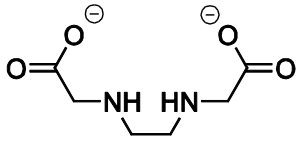

edda

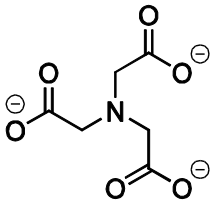

nta

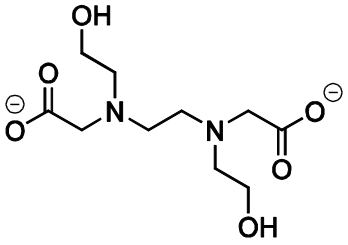

bhedda

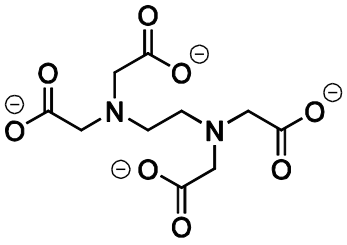

edta

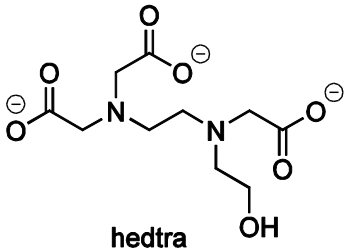

hedtra

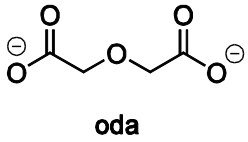

oda

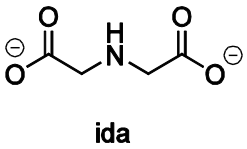

ida

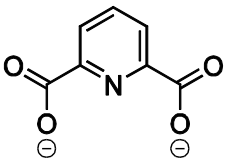

dipic

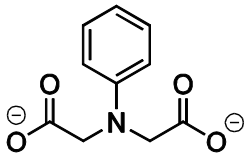

phida

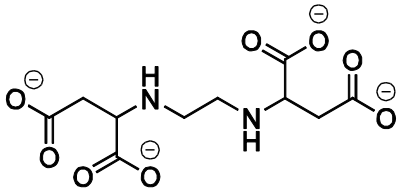

edds

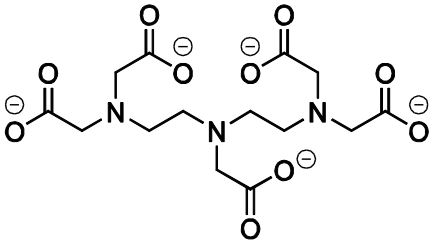

dtpa

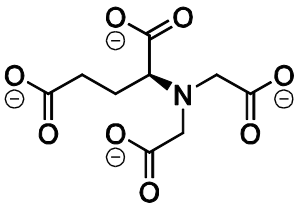

AcGlu

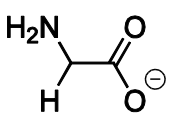

gly

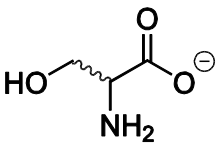

ser

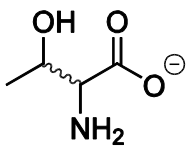

thr

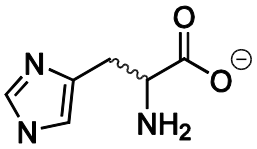

his

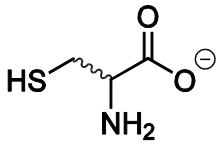

cys

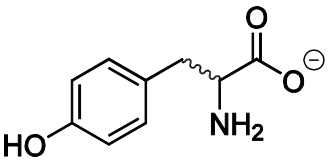

tyr

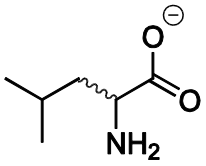

leu

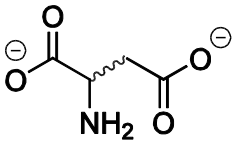

asp

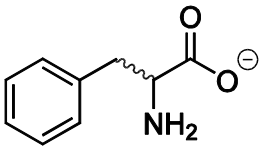

phe

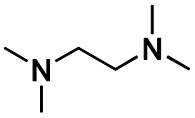

tmeda

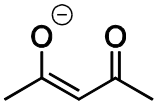

acac

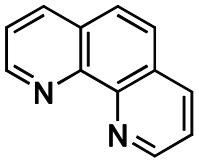

phen

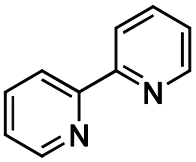

bpy

acac	acetylacetonato
AcGlu	*N*,*N*-bis(carboxymethyl)-L-glutamato
asp	aspartato
bhedda	*N*,*N*′-bis(2-hydroxyethyl)ethylenediamine-*N*,*N*′-diacetato
bpy	2,2′-bipyridine
cys	cysteinato
dipic	pyridine-2,6-dicarboxylato
dtpa	diethylenetriaminepentaacetato
edda	ethylenediamine-*N*,*N*′-diacetato
edds	ethylenediamine-*N*,*N*′-disuccinato
edta	ethylenediamine-*N*,*N*,*N*′,*N*′-tetraacetato
gly	glycinato
hedtra	*N*-(2-hydroxyethyl)ethylenediamine-*N,N′,N*′-triacetato
his	histidinato
ida	iminodiacetato
leu	leucinato
nta	nitrilotriacetato
oda	oxodiacetato
phe	phenylalaninato
phen	1,10-phenanthroline
phida	*N*-phenyliminodiacetato
ser	serinato
thr	threoninato
tmeda	*N*,*N*,*N*′,*N*′-tetramethylethylenediamine
tyr	tyrosinato

Overview of numbered compounds

Stable $\{FeNO\}^7$(S = 3/2) complexes with aminecarboxylates

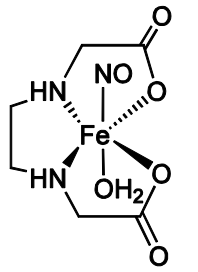

1a

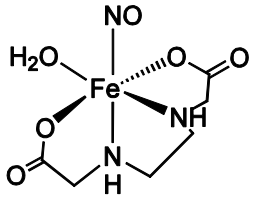

1b

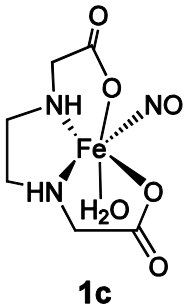

1c

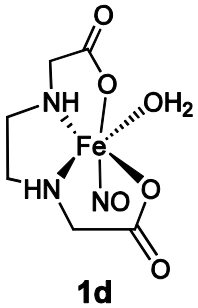

1d

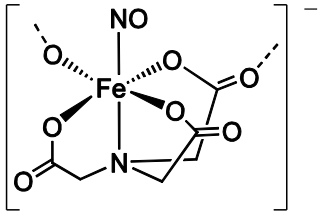

2

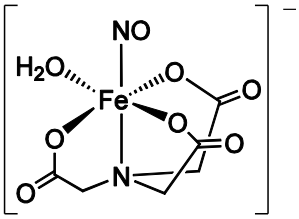

2i

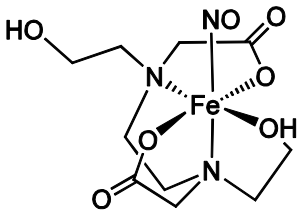

3

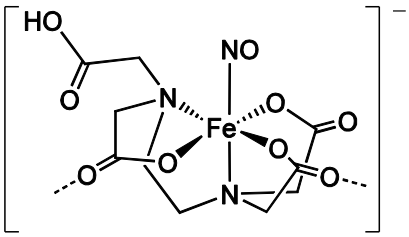

4

1a (*OC*-6-44)-aquaethylenediamine-*N,N′*-diacetatonitrosyliron

1b (*OC*-6-14)-aquaethylenediamine-*N,N′*-diacetatonitrosyliron

1c (*OC*-6-42)-aquaethylenediamine-*N,N′*-diacetatonitrosyliron

1d (*OC*-6-42)-aquaethylenediamine-*N,N′*-diacetatonitrosyliron

2 (*OC*-6-11)-nitrilotriacetatonitrosylferrate

2i (*OC*-6-21)-aquanitrilotriacetatonitrosylferrate

3 (*OC*-6-14)-*N,N′*-bis(2-hydroxyethyl)ethylenediamine-*N,N′*-diacetatonitrosyliron

4 (*OC*-6-31)-ethylenediamine-*N,N,N′,N′*-tetraacetatonitrosylferrate

Iron(II) complexes with aminecarboxylates

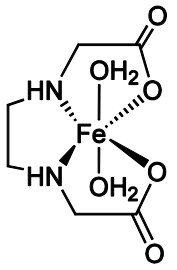

5a

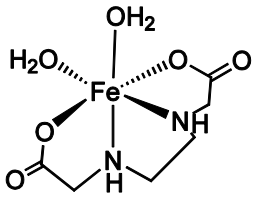

5b

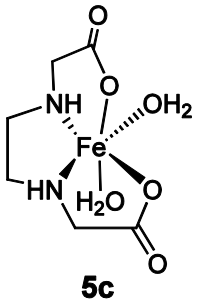

5c

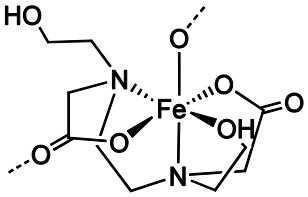

6

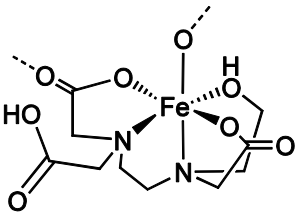

7

5a (*OC*-6-33)-diaquaethylenediamine-*N,N′*-diacetatoiron(II)

5b (*OC*-6-13)-diaquaethylenediamine-*N,N′*-diacetatoiron(II)

5c (*OC*-6-32)-diaquaethylenediamine-*N,N′*-diacetatoiron(II)

6 (*OC*-6-13)-*N,N′*-bis(2-hydroxyethyl)ethylenediamine-*N,N′*-diacetatoiron(II)

7 (*OC*-6-31)-*N*-(2-hydroxyethyl)ethylenediamine-*N,N′,N′*-triacetatoiron(II)

Selected less stable $\{FeNO\}^7$(S = 3/2) complexes with mixed N,O-chelators and aqua ligands, adopted from Reference [4]

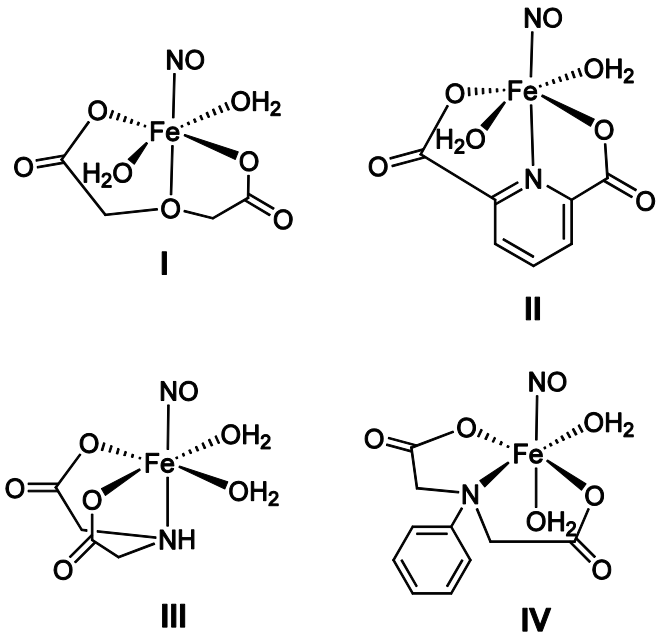

I (*OC*-6-14)-diaquanitrosyloxodiacetatoiron

II (*OC*-6-12)-diaquadipicolinatonitrosyliron

III (*OC*-6-22)-diaquaiminodiacetatonitrosyliron

IV (*OC*-6-14)-diaquanitrosyl-*N*-phenyliminodiacetatoiron

1 Introduction

1.1 The chemical biology of nitric oxide

Long known for its toxigenic and environmentally destructive properties[5–8], the small molecule nitric oxide (NO) attracted worldwide research interest due to its important role as a cellular signaling molecule in mammals. Nitric oxide is involved in several physiological processes in the human body, where it acts as a regulator of blood pressure, as an immune defense agent and as a neurotransmitter in the central nervous system. Because of its regulatory effects in the cardiovascular and nervous system, nitric oxide was declared molecule of the year by the journal *Science* in 1992.[9,10] Six years later, in 1998, the American scientists Furchgott, Ignarro and Murad were awarded the Nobel Prize in Physiology or Medicine "for their discoveries concerning nitric oxide as a signaling molecule in the cardiovascular system".[11–14] Ongoing research continued in order to understand the cellular mechanisms that regulate the formation and the reactivity of the small hormone NO.

NO is biosynthesized endogenously by the oxidation of L-arginine to L-citrulline with the enzyme nitric oxide synthase (NOS) (Scheme 1.1). NADPH and molecular oxygen are involved as co-substrates.[15]

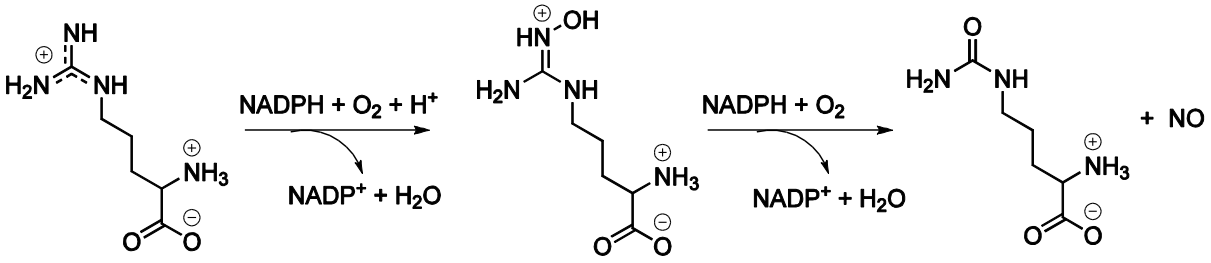

L-arginine *N*-ω-hydroxy-arginine L-citrulline

Scheme 1.1: The endogenous formation of NO from oxidation of L-arginine by the nitric oxide synthase (NOS).[15]

In humans, three isoforms of the NOS enzyme are known: neuronal NOS of the nervous system (nNOS), inducible NOS of the immune system (iNOS) and endothelial NOS of the cardiovascular system (eNOS).[16–18] While the constitutive isoforms eNOS and nNOS produce only low amounts of NO in the cell, the induction of iNOS can lead to sustained NO fluxes in the micromolar range that can be cytotoxic.[19] Under hypoxic conditions, the reduction of nitrite (NO_2^-) can serve as an alternative oxygen-independent source for low levels of NO in the cell.[20]

Once produced, the small NO molecule quickly diffuses across cell membranes and reacts with diverse cellular targets, which leads to various biological implications (see Figure 1.1). Most NO-regulated physiological processes are initiated by the activation of soluble guanylate cyclase (sGC), an Fe^{II} heme protein (Figure 1.2 and Scheme 1.2). There are several studies in literature that focus on elucidating the molecular mechanism of the sGC activation in order to emphasize its role in the development of novel

therapeutic agents.[18,21–24] It is presumed that the nitrosylation of sGC at the distal site of the enzyme causes bond cleavage between the proximal His ligand and the low-spin Fe^{II} heme center, which activates the conversion of GTP to cGMP. The second messenger cGMP then modulates phosphodiesterases (PDEs), ion-gated channels or cGMP-dependent protein kinases to regulate vasodilation and neurotransmission.[18]

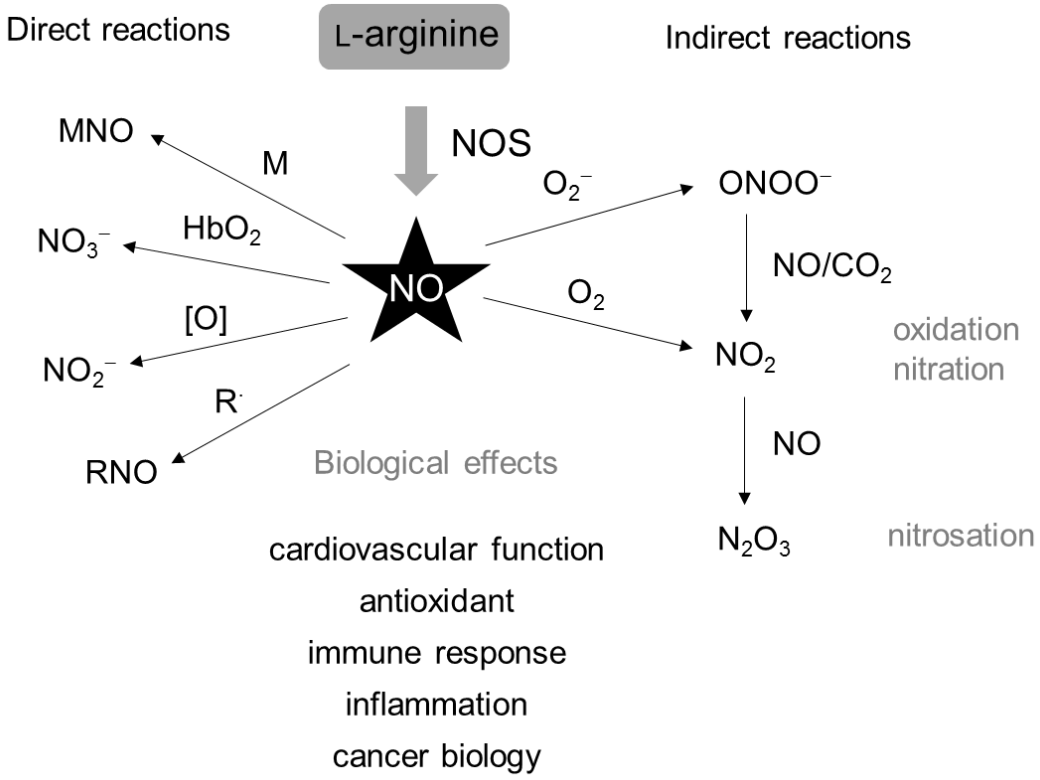

Figure 1.1: Direct and indirect reactions of NO with important cellular targets and their biological implications. Redrawn from Reference [25].

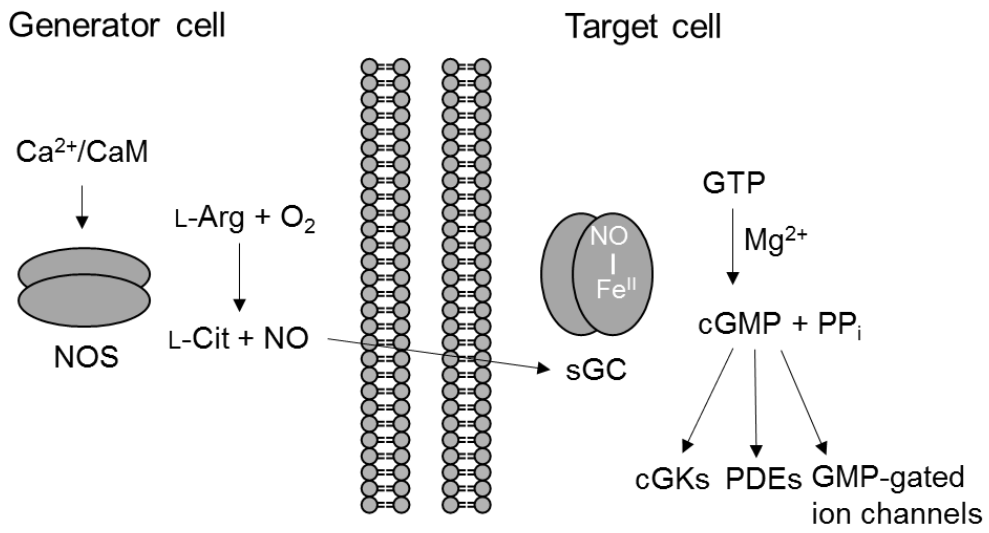

Figure 1.2: The nitric oxide / cyclic GMP (NO/cGMP) signaling pathway. Nitric oxide synthase (NOS) catalyzes the biosynthesis of L-arginine (L-Arg) to L-citrulline (L-Cit) and nitric oxide (NO). Ca^{2+}/calmodulin (CaM) activates the NOS by a structural change that enables a continual electron flow. The endogenously produced NO diffuses across cell membranes and binds to the Fe^{II} heme center of soluble guanylate cyclase (sGC). This results in significant increase of the second messengers cGMP and pyrophosphate (PPi). cGMP activates the cGMP-dependent protein kinases (cGKs), phosphodiesterases (PDEs) and ion-gated channels. Redrawn from Reference [18].

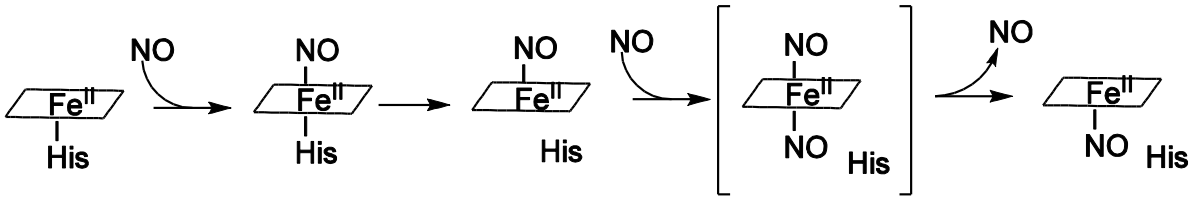

Scheme 1.2: Reaction scheme of NO-binding to the Fe^{II} heme center of soluble guanylate cyclase (sGC). The presumed dinitrosyl intermediate is shown in brackets. Adopted from Reference [24].

Blood-sucking insects profit from NO's ability to widen the blood vessels: they inject nitric oxide loaded nitrophorines (NO-binding Fe^{III} heme enzymes) into the bloodstream of their victims. The Fe–NO linkage of these Fe^{III} heme enzymes is, however, weaker than the linkage in the formerly discussed Fe^{II} heme enzymes. Thus, NO is released from the nitrophorines in the bloodstream, the blood vessels dilate and the bloodsuckers benefit from the increased blood flow.[26] NO interacts also with various other heme proteins including hemoglobin, cyclooxygenase, cytochrome P450 and cytochrome c oxidase.[27] For instance, the reaction of NO with oxyhemoglobin (HbO_2) to nitrate (NO_3^-) and methemoglobin serves as a major regulatory mechanism for the *in-vivo* NO detoxification.[17,28,29] High levels of NO trigger the formation of reactive nitrogen species (RNS), typically by the oxidation of the NO molecule. Nitrogen dioxide (NO_2), dinitrogen trioxide (N_2O_3), and the powerful oxidant peroxynitrite ($ONOO^-$) are essential

RNS.[17,30] These species act as potent nitrating, nitrosating and oxidizing agents that may initiate cancer, septic shock and other diseases.[17,30] But they play an important role as antitumorigenic mediators as well.[16]

In order to get a better understanding of the cellular processes that are associated with the formation and the reactivity of the hormone NO, the properties of NO as a ligand must be taken into consideration. The next chapter focuses on the role of nitric oxide as a ligand in metal complexes.

1.2 General properties and coordination chemistry of nitric oxide

NO is produced on a large scale as an intermediate in the Ostwald process, in which nitric acid is synthesized from ammonia.[31] The formation of nitric oxide from oxygen and nitrogen is a strongly endothermic reaction (Scheme 1.3).[32]

$$\tfrac{1}{2}\,N_2 + \tfrac{1}{2}\,O_2 \longrightarrow NO \qquad \Delta_f H^\circ = +90.4\ \text{kJ mol}^{-1}$$

Scheme 1.3: The endothermic reaction of oxygen and nitrogen to nitric oxide.

Due to its odd number of eleven valence electrons, NO is a paramagnetic free radical. It has a bond order of 2.5, a N–O bond length of 1.15 Å and its stretching vibration band is found at 1875 cm^{-1}.[33,34] At ambient temperature, NO is a colorless gas that reacts immediately with molecular oxygen into the brown gas NO_2. Because of its weak dipole moment, NO is poorly soluble in water (1.93–1.95 · 10^{-6} mol cm^{-3}).[35] The Lewis structures of NO are illustrated in Scheme 1.4.

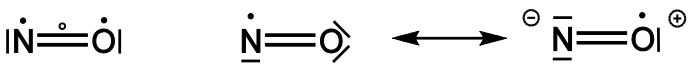

Scheme 1.4: Lewis structures of nitric oxide.

The radical character of NO makes it a highly chemically reactive species. Stabilization of the unpaired electron can be achieved upon the reaction with other compounds bearing unpaired electrons or upon the reaction with transition-metal complexes to generate nitrosyl-metal complexes.

The various properties of NO as a ligand in metal complexes become apparent from its molecular orbital (MO) diagram (Figure 1.3). The unpaired electron, which is responsible for the radical character, is located in one of the two 1π* orbitals. The frontier orbitals 2σ (HOMO−1) and 1π* (HOMO) are suitable for forming binding and antibinding interactions with the d orbitals of a transition metal. Because of their larger lobes on the nitrogen atom, coordination in a *κN*-binding mode is favored under normal conditions. The 2σ orbital can form a σ interaction with the symmetrically matching e orbitals of the metal and the energetically higher, degenerated 1π* orbitals can interact with the metal t_2 orbitals to two π-type bonds.

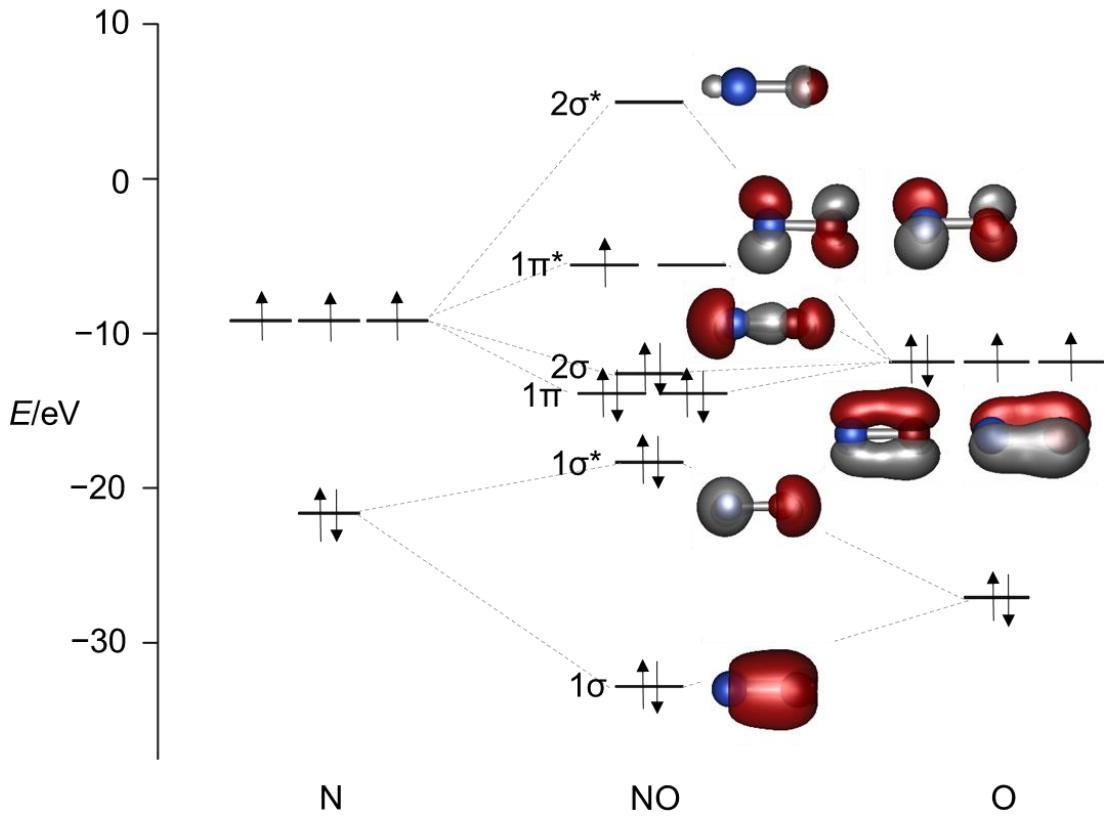

Figure 1.3: Molecular orbital (MO) scheme of the neutral NO radical. The nitrogen atom is illustrated in blue, the oxygen atom in red. Up-arrows symbolize α-spin electrons, down-arrows β-spin electrons. The unpaired electron, which is responsible for the redox activity of the ligand, is located in one of the degenerated 1π* orbitals. Orbitals were calculated with TPSSh/def2-tzvp, isovalue 0.14.

Upon coordination to a metal center, NO can easily be oxidized to the nitrosonium cation NO^+ or reduced to the nitroxyl anion NO^-. Thus, NO is a so-called non-innocent, redox-active ligand.[36] Four coordination modes with either linear or bent M−N−O moieties are possible: the NO ligand can coordinate linearly as NO^+, weakly bent as neutral $NO^\bullet$, strongly bent as $^1NO^-$ and linear or weakly bent as $^3NO^-$.[34,37] The analogy of the $^3NO^-$ ligand to the $^3O_2$ ligand is used, for example, to model the structure of biochemical non-heme iron oxygenases.[38]

Characteristic spectroscopic and structural parameters can be useful to draw conclusions about the electronic state of the complex in question. For instance, the N–O stretching vibration bands, the M–N and the N–O bond distances as well as the M–N–O bond angles, derived from X-ray crystallography, can provide helpful information for identifying the bonding mode in the nitrosyl compounds.[34]

Depending on the geometry of the M–N–O moiety, different bonding interactions define the metal-nitrosyl fragment (Figure 1.4, the z-axis is defined along the M–N vector of the M–N–O group). The doubly occupied 2σ orbital donates electron density into the d_{z^2} orbital of the metal to generate a σ bond (σ-basicity of the NO ligand). The 1π* orbitals interact as electron donors or electron acceptors with the symmetrically matching metal d_{xz} and d_{yz} orbitals either to two π-bonding interactions (linear M–N–O moiety) or to one π-bonding interaction and one σ-bonding interaction with a strong metal d_{z^2} orbital

participation (bent M–N–O moiety).[34,37,39] In the case of a linear NO^+ ligand and an electron-rich metal center, strong backdonation from the d_{xz} and d_{yz} metal orbitals into the 1π* orbitals of NO prevails. Hence, the NO ligand can also interact as a π acid.

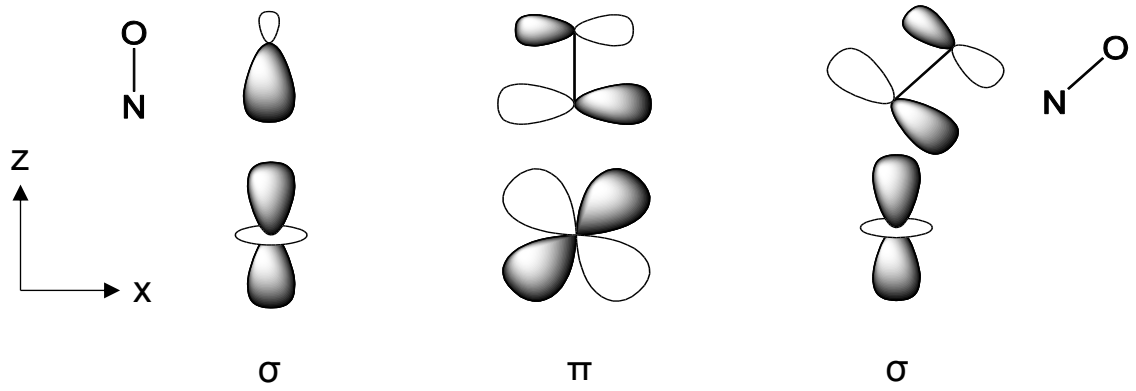

Figure 1.4: The possible bonding interactions of the metal-nitrosyl bond. Left: σ bond ($2\sigma + d_{z^2}$), middle: π bond(s) ($1\pi^*_{xz} + d_{xz}$ and $1\pi^*_{yz} + d_{yz}$ in a linear M–N–O moiety), right: σ-bonding interaction in a bent M–N–O moiety ($1\pi^*_{yz} + d_{z^2}$).

In order to avoid the problem of assigning a physical oxidation state to the central metal atom and to the NO ligand, the Enemark-Feltham nomenclature was established in 1974.[39] In this context, the metal-nitrosyl complex is classified as a $\{M(NO)_x\}^n$ fragment, whereby *x* is the number of binding NO ligands and *n* is the sum of the electrons in the d orbitals of the metal and in the 1π* orbitals of the NO ligand. Using this formalism, the NO-binding Fe^{II} heme center of sGC may be described as a low-spin $\{FeNO\}^7$ center and the NO-binding Fe^{III} heme center of the nitrophorines as a low-spin $\{FeNO\}^6$ center.[26] The exact bonding mode in NO-binding heme enzymes is still a subject of ongoing research discussions.[40–42]

1.3 Relevance of high-spin nitrosyl-iron compounds

This thesis focuses on the synthesis and the theoretical description of the bonding mode of high-spin nitrosyl-iron(II) compounds. These species are thought to be relevant intermediates in the anaerobic respiration and NO detoxification process performed by microorganisms.[15,43–47] They play, moreover, an important role in the so-called BioDeNOx process that is a proven method for NO_x removal from industrial flue gases.[48–57] The electronic structure of the high-spin nitrosyl-iron complexes differs from the previously described low-spin species that are found within the NO-bound iron heme enzymes (see chapter 1.1). In literature, their bonding mode is commonly described as a high-spin Fe^{III} ($S = 5/2$) that is antiferromagnetically coupled to a $^3NO^-$ ligand ($S = 1$).[58–67] This results in an overall spin state of $S = 3/2$. According to the Enemark-Feltham notation, the complexes can be designated as $\{FeNO\}^7(S = 3/2)$ or as quartet-$\{FeNO\}^7$ species.

1.3.1 Nitric oxide reductases

Chapter 1.1 demonstrates the essential role of NO as a signaling molecule in mammals. In contrast to mammalian species, many microorganisms possess NO-reducing enzymes that catalyze the two-electron reduction of two NO molecules to the less-toxic N_2O as part of their anaerobic respiration process or as a detoxifying strategy (Scheme 1.5).[15,43–47]

$$2\ NO + 2\ e^- + 2\ H^+ \xrightarrow{NORs} N_2O + H_2O$$

Scheme 1.5: The two-electron reduction of NO to N_2O performed by the nitric oxide reductases (NORs).

Three different types of nitric oxide reductases (NORs) were identified: the NO reductases of denitrifying bacteria (NorBC, qNOR and qCu_ANOR)[43,45], the fungal P450 NO reductase (P450nor)[44,68,69] and the flavodiiron NO reductases of non-denitrifying bacteria, archaea, and protozoans (FNORs)[15,70,71]. While the enzymes NorBC, qNOR and qCu_ANOR catalyze NO reduction predominantly as part of anaerobic respiration, FNORs have evolved in order to protect the non-denitrifying organisms against exogenously produced NO. This allows the pathogens to proliferate in the human body.[15]
The subsequent part of this chapter provides a brief insight into the proposed catalytic mechanisms of the NO reduction processes (Schemes 1.6–1.8). The active sites of the different NORs enzymes are shown in Figure 1.5.

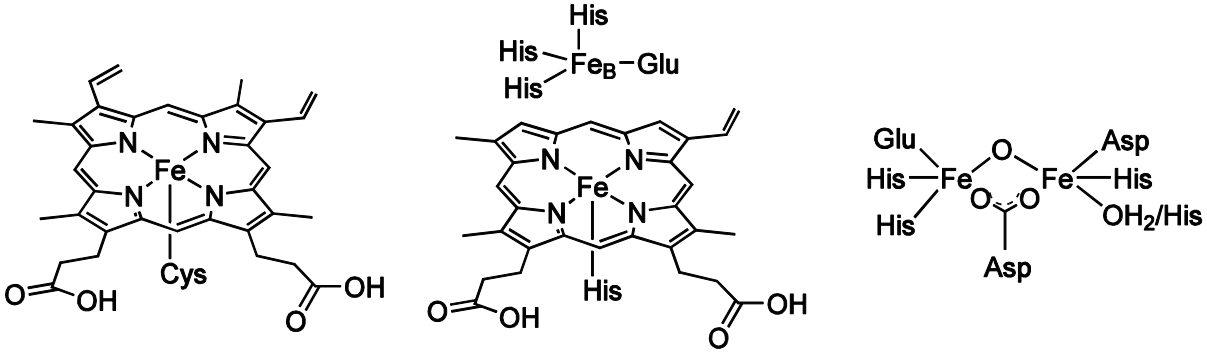

Figure 1.5: The iron-containing active sites of the different NORs. Left: fungal P450 NO reductase (P450nor), middle: bacterial nitric oxide reductases (NorBC, qNOR, qCu_ANOR), right: flavodiiron NO reductases (FNORs). The FNORs of some microorganisms possess an additional His ligand instead of the non-bridging H_2O.[15,43,44]

In P450nor (a cytochrome P450-type enzyme) NO reduction occurs at a mononuclear low-spin Fe^{III} heme center. NO binds upon the formation of a $\{FeNO\}^6$ species in the catalytically active state of the enzyme. The activation is followed by hydride-transfer from the cofactor NAD(P)H to the $\{FeNO\}^6$ complex, which results in an $\{FeHNO\}^8$ intermediate. Either this intermediate or an analogous double-protonated species, which can be described as Fe^{IV}–$NHOH^-$ or Fe^{III}–$NHOH^{\cdot}$ complex, reacts with a second NO molecule upon N–N bond formation to the product species N_2O.[44,47,72,73]

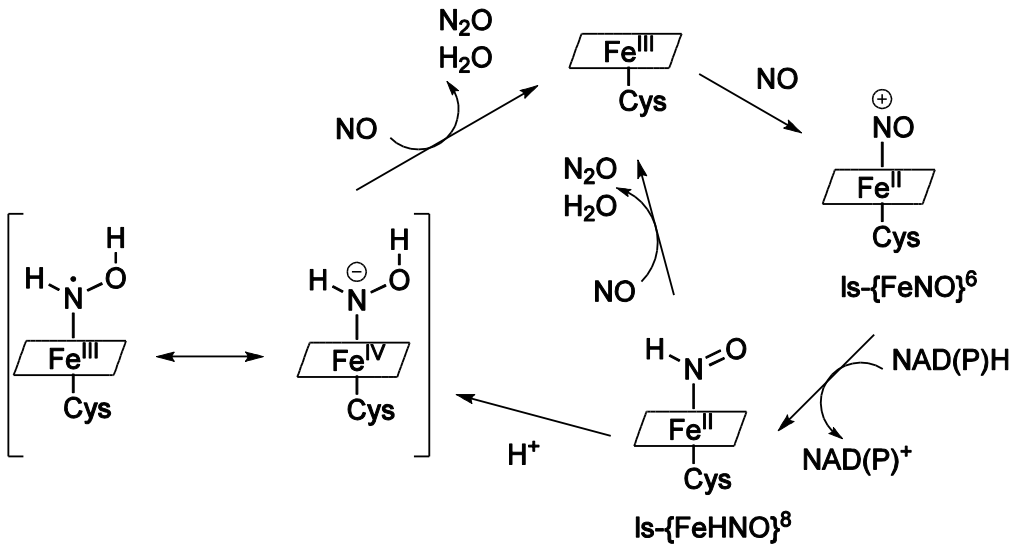

Scheme 1.6: Proposed mechanism for the N_2O formation in fungal P450nor. Redrawn from Reference [47].

The three classes of bacterial respiratory NORs (NorBC, qNOR and qCu_ANOR) share the same active site, but vary in their electron donors and internal electron-transfer sites. The active site of the bacterial NO reductase enzymes consists of a heme and a non-heme (Fe_B) iron motif.[43,45,74] Three overall mechanisms have been proposed for these enzymes (Scheme 1.7): the NO activation can occur either at both the non-heme (Fe_B) center and the heme iron center (*trans* mechanism) or at a single iron site (*cis* heme b3 mechanism and *cis* FeB mechanism). In contrast to the *cis* Fe_B mechanism, in which both NO molecules are suspected to bind to the Fe_B site, the *cis* heme b3 mechanism involves the electrophilic attack of a second NO molecule to the initially generated heme-bound NO species. All of these mechanisms include the formation of a hyponitrite dianion intermediate and the concomitant oxidation of both iron centers prior to the release of N_2O.[75] Most studies in literature presume a non-heme $\{FeNO\}^7$ as well as a heme $\{FeNO\}^7$ intermediate during the NO reduction process.[76–78] It is however worth mentioning that there is some discussion about a non-heme $\{FeNO\}^8$ and a heme $\{FeNO\}^6$ center as transient species in a redox-type coupling process within the *trans* mechanism.[46,47]

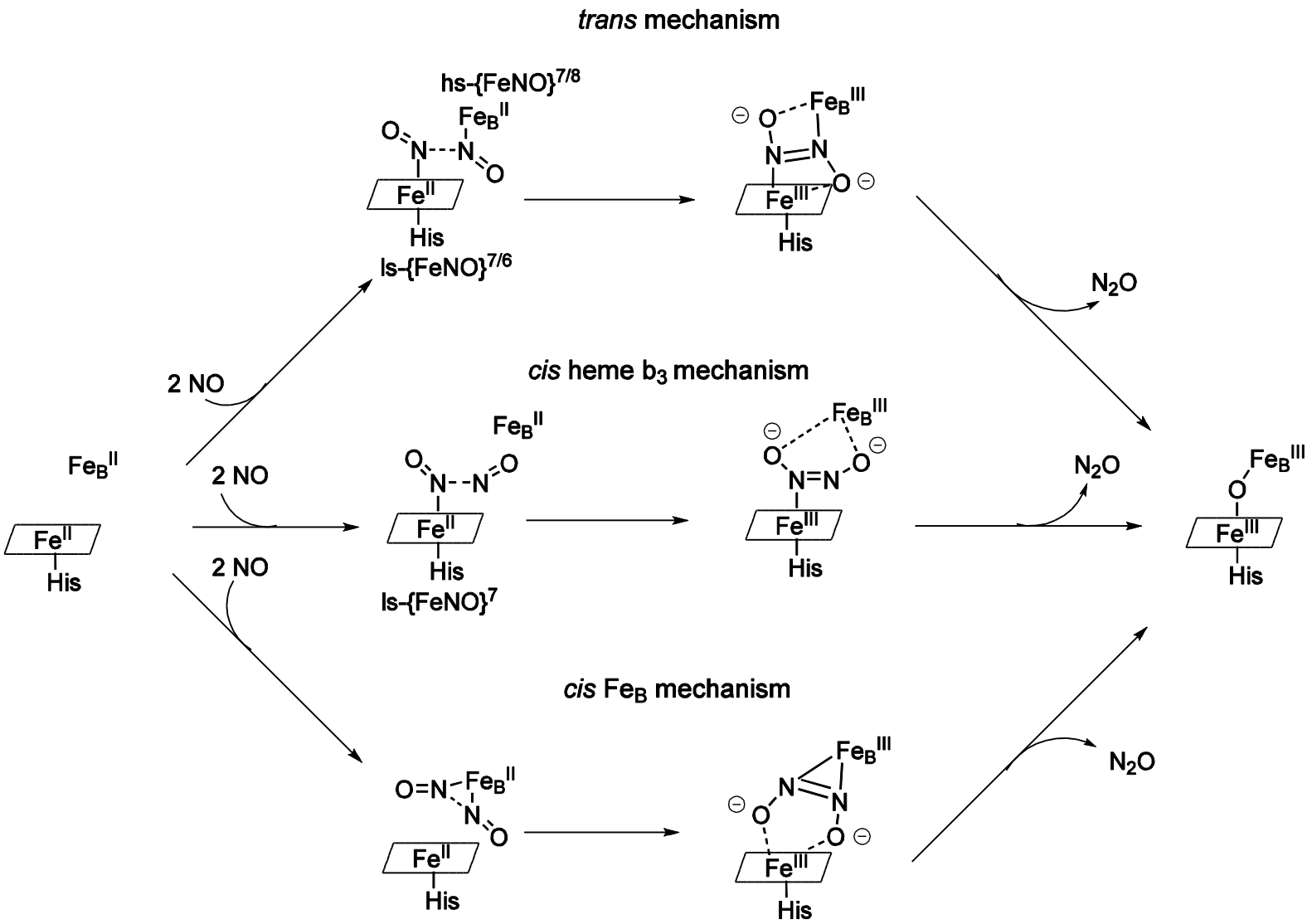

Scheme 1.7: The three proposed mechanisms for the N_2O formation in bacterial respiratory NORs.[75]

Flavodiiron NO reductases (FNORs) contain a non-heme diiron active site with a flavin mononucleotide (FMN) cofactor in close proximity that enables fast electron transfer between the cofactor and the diiron core.[15,70,71] The exact mechanism of NO reduction in FNORs is still a subject of discussion in the literature.[15,46] Three probable mechanisms are shown in Scheme 1.8. For one thing, NO reduction can be achieved via the formation of a semi-bridging mononitrosyl high-spin [Fe^{II}{FeNO}^{7}] intermediate that reacts with a second NO molecule to N_2O (bridging mononitrosyl mechanism).[46,47,79,80] Otherwise, the reaction of two NO molecules with the catalytically active diferrous form of the enzyme results in a high-spin [{FeNO}^{7}]$_2$ intermediate. This intermediate can generate N_2O via the coupling of the two Fe–N–O moieties (diferrous dinitrosyl mechanism). In an alternative mechanism, the high-spin [{FeNO}^{7}]$_2$ intermediate is reduced to a so-called super-reduced high-spin [{FeNO}^{8}]$_2$ species by the FMN cofactor, which performs N–N coupling in order to release N_2O (super-reduced mechanism).[46,47,81,82]

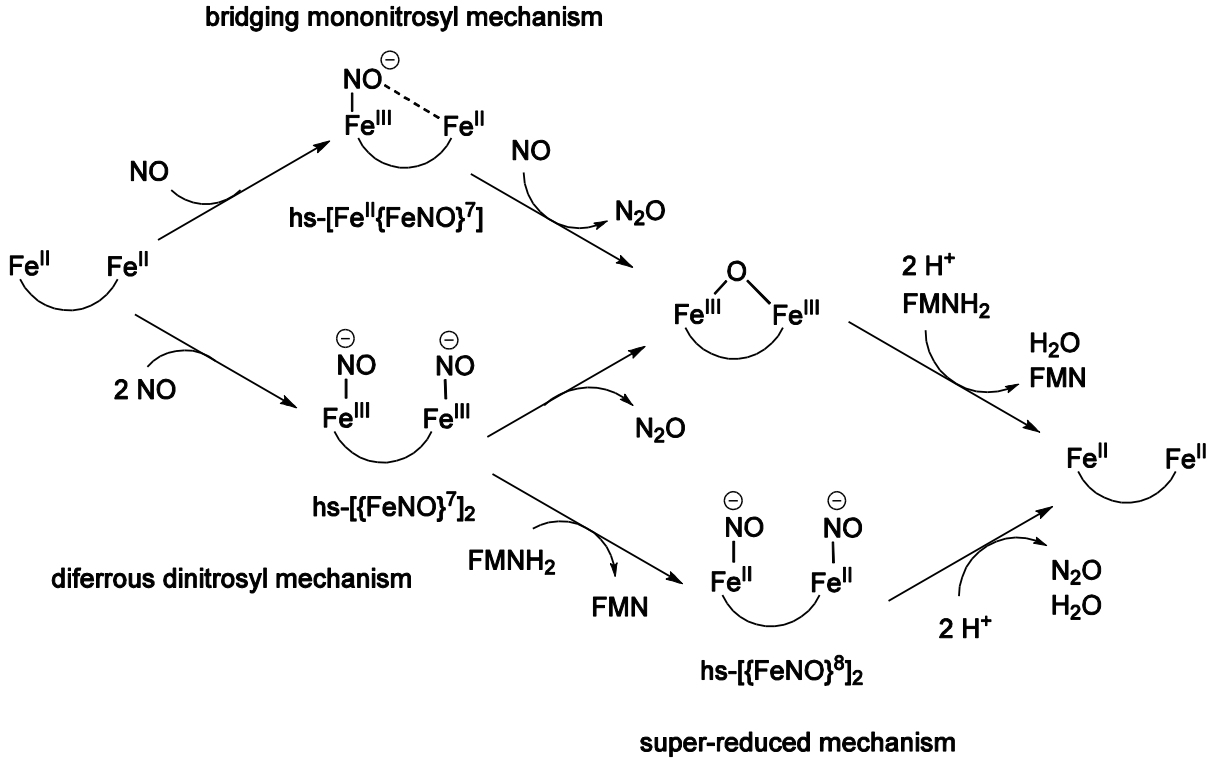

Scheme 1.8: Three proposed mechanisms for the N_2O formation in FNORs. Copied from Reference [83].

1.3.2 {FeNO}^{7}(S = 3/2) complexes with aminecarboxylato co-ligands

In the 1980s, aminecarboxylato co-ligands were discovered to induce a markedly increased stability of {FeNO}^{7}(S = 3/2) complexes against NO release. The research activities in this field were motivated by the concept that the enhanced Fe–NO binding of the complexes makes them a suitable agent for the removal of NO from power-plant-flue gas streams.[84,85] In the 2000s, the van Eldik group published several studies on spectroscopic, thermodynamic as well as kinetic data of aqueous {FeNO}^{7}(S = 3/2) complexes with aminecarboxylates.[86–90] The research group investigated the reactivity of aqueous iron(II) chelates against nitric oxide and oxygen, whereby co-ligands of various denticity such as edta, nta and ida were used. The {FeNO}^{7}(S = 3/2) complexes were synthesized by treating an aqueous buffered reaction solutions of iron(II) salts and aminecarboxylato co-ligands with gaseous nitric oxide and the formation of the Fe–NO linkage was followed by IR and UV/Vis spectroscopy. Van Eldik's group determined the stability constants K_{NO} for the nitrosyl complexes and, moreover, the oxidation sensitivity of the iron(II) aminecarboxylate species. It was found that the stability of the Fe–NO linkage roughly correlates with the sensitivity of the respective aqueous solution to oxidation by O_2. The research group stated that the higher stability of the Fe–NO linkage is connected with a higher Fe^{III} character of the {FeNO}^{7}(S = 3/2) species. Nevertheless, all of these studies were not supported by structural information on the complexes.

The stability constants K_{NO} of the nitrosyl compounds were determined in the following manner: K_{NO} is generally based on the reaction equilibrium between the $[Fe^{II}(L)_n]$ and $[Fe^{II}(L)_n(NO)]$ complexes (Formula 1.1, L = aminecarboxylato co-ligand). K_{NO} is thus defined according to Formula 1.2:

$$[Fe^{II}(L)_n] + NO \underset{k_2}{\overset{k_1}{\rightleftharpoons}} [Fe^{II}(L)_n(NO)] \tag{1.1}$$

$$K_{NO} = \frac{k_1}{k_2} = \frac{c_{[Fe^{II}(L)_n(NO)]}}{c_{[Fe^{II}(L)_n]} \cdot c_{[NO]}} \tag{1.2}$$

The equilibrium concentrations of the $[Fe^{II}(L)_n]$ and $[Fe^{II}(L)_n(NO)]$ species were identified by means of UV/Vis spectroscopy and the concentration of free nitric oxide in solution with a NO electrode. The oxidation of the complex compounds was also followed by UV/Vis spectroscopy. The period of time after more than about 80% of the $[Fe^{II}(L)_n]$ species was oxidized to the corresponding $[Fe^{III}(L)_n]$ complex, was defined as "qualitative oxidation time". A correlation between the K_{NO} values and the "qualitative oxidation time" of the complexes is illustrated in Figure 1.6.

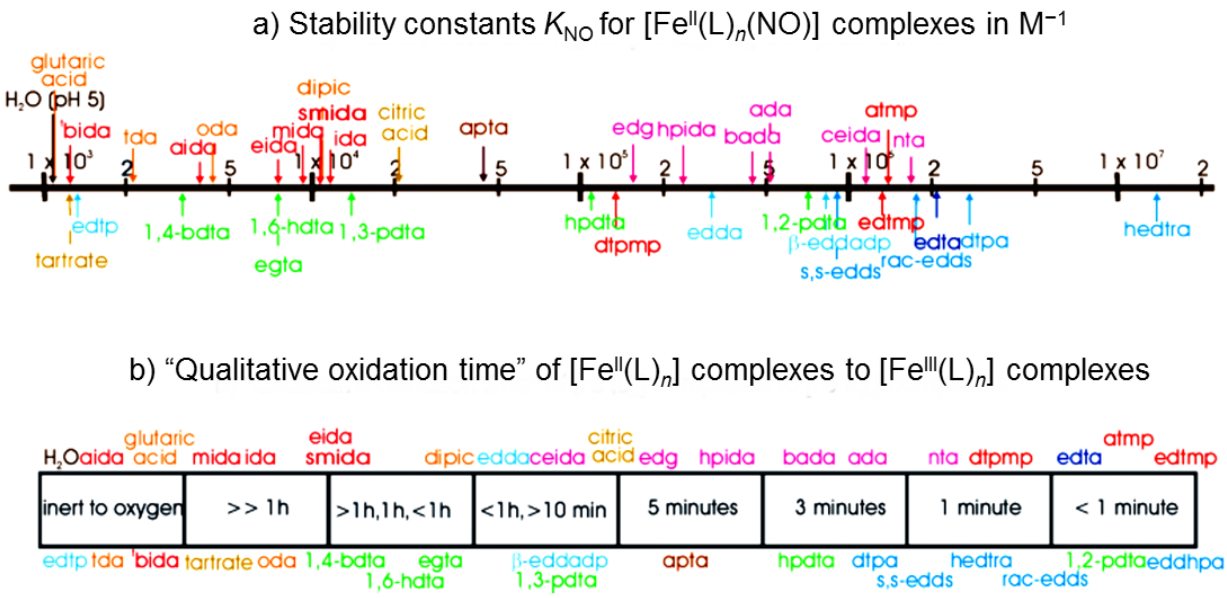

Figure 1.6: The stability constants K_{NO} of the $[Fe^{II}(L)_n(NO)]$ complexes (a) and the "qualitative oxidation time" of $[Fe^{II}(L)_n]$ complexes to $[Fe^{III}(L)_n]$ complexes (b). The period of time after more than about 80% of the $[Fe^{II}(L)_n]$ species was oxidized to the corresponding $[Fe^{III}(L)_n]$ complex was defined as "qualitative oxidation time". L = aminecarboxylato co-ligand. The various groups of chelate ligands are presented in different colors (see Reference [87] for further details). The survey is copied from Reference [87].

It is a known fact that the emission of nitrogen oxides (NO_x), produced from combustion of coal and fuel oils, causes harmful environmental complications such as acid rain, the depletion of the ozone layer and photochemical pollution.[5–7] The chemical-absorption-biological-reduction (CABR) process or simply BioDeNOx process is a cost-efficient and "green" technology for NO_x disposal from coal-fired power plants.[48–57] Herein, the NO removal is accomplished via the complexation to aqueous iron(II) chelates, whereupon edta is commonly used as the chelating agent. The technology takes advantage of the efficient binding of NO to the $[Fe^{II}(edta)]^{2-}$ species in order to increase the solubility of free NO in aqueous solution. This is of particular importance since the removal efficiency of NO is hindered by the mass transfer from gas to liquid phase, which is attributed to the high Henry's constant of NO.[91] The principle of the BioDeNOx technology is shown in Figure 1.7. NO is absorbed by the $[Fe^{II}(edta)]^{2-}$ species in a wet-separator (or scrubber in the field of engineering science) and subsequently reduced to harmless N_2 by microbial denitrification in a bioreactor. As seen from van Eldik's studies, the high reactivity of the $[Fe^{II}(edta)]^{2-}$ species against NO is associated with a high oxygen sensitivity of the NO scavenger. Thus, the $[Fe^{III}(edta)]^{-}$ complex, which is formed by the reaction with oxygen in the flue gas, is regenerated to the $[Fe^{II}(edta)]^{2-}$ species in a microbial iron-reduction step, whereby a suitable reductant serves as an electron donor (ethanol, for example).

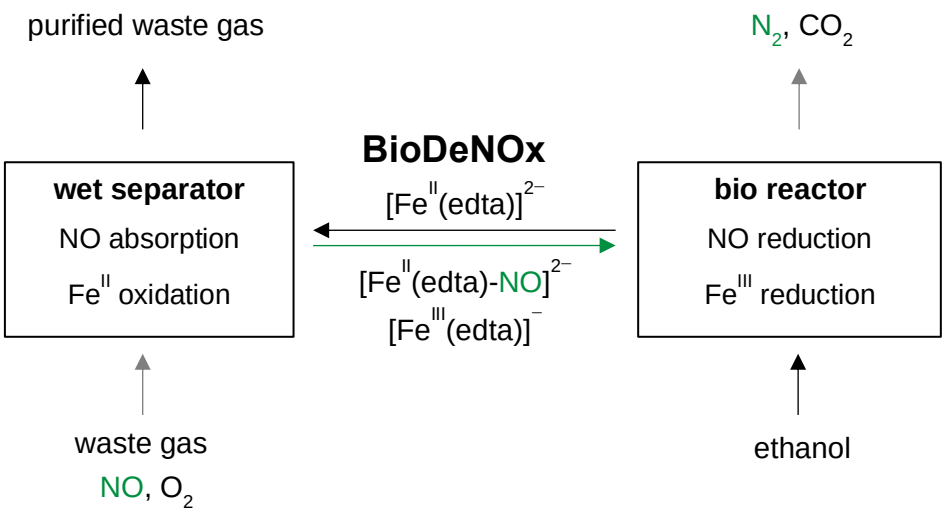

Figure 1.7: The principle of the BioDeNOx process. Redrawn from Reference [53].

The tentative chromophore of the "brown ring", $[Fe(H_2O)_5NO]^{2+}$, is a well-known representative of $\{FeNO\}^7$ (S = 3/2) complexes. It is observable in the qualitative nitrate test, performed commonly in undergraduate education (Figure 1.8). In a sulfuric acid solution that contains Fe^{II} ions, nitrate ions (NO_3^-) are reduced to NO and Fe^{II} ions are oxidized to Fe^{III} ions. The *in-situ* generated NO binds excess $[Fe(H_2O)_6]^{2+}$ and the tentative chromophore of the brown ring, $[Fe(H_2O)_5NO]^{2+}$, becomes apparent as a brown, ring-shaped coloring in the test tube (see Figure 1.8).[86,92] X-ray structure analysis of this cation has not been available as yet but calculations and spectroscopic data indicate a linear Fe–N–O moiety with an electronic structure between high-spin $[Fe^{III}(H_2O)_5(^3NO^-)]^{2+}$ and high-spin $[Fe^{II}(H_2O)_5(NO)]^{2+}$.[86,92–96]

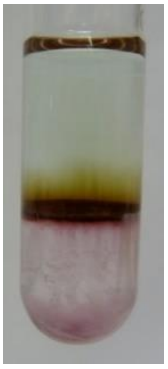

$$3\ Fe^{2+} + NO_3^- + 4\ H_3O^+ \longrightarrow 3\ Fe^{3+} + NO + 6\ H_2O$$

$$[Fe(H_2O)_6]^{2+} + NO \rightleftharpoons [Fe(H_2O)_5(NO)]^{2+}$$

Figure 1.8: The "brown-ring test". The tentative chromophore of the "brown ring", $[Fe(H_2O)_5NO]^{2+}$, is a well-known representative of $\{FeNO\}^7$ (S = 3/2) complexes. The picture is presented with kind permission from Prof. Dr. Peter Klüfers.

1.4 Scope of thesis

This thesis is focused on the examination of the molecular structures and the electronic configuration of octahedrally coordinated $\{FeNO\}^7$(S = 3/2) complexes. Even though about three dozen single-crystal X-ray analyses on these compounds can be found in literature, only eight species have been crystallized from an aqueous solution.[4,46,60,81,97–115] M. Wolf of the Klüfers group succeeded in synthesizing crystalline quartet-$\{FeNO\}^7$ compounds with derivatives of iminodiactetate (ida) as co-ligands and aqua ligands that complete the octahedral coordination sphere. These are the first crystalline $\{FeNO\}^7$(S = 3/2) complexes with aqua co-ligands.[4,115] According to van Eldik's studies, the species rank among the less-stable $\{FeNO\}^7$(S = 3/2) compounds with aminecarboxylates (left hand side of the upper series in Figure 1.6 on page 12).[87,89] A detailed analysis of the bonding situation with quantum-chemical calculations revealed that the Fe–NO bonding is best described as a mostly covalent interaction with a neutral NO^0 ligand antiferromagnetically coupled to an Fe^{II} center.[4,115] However, structural information on the stable subclass in the van Eldik series is still lacking (right-hand side of the upper series in Figure 1.6 on page 12). An important representative beyond this subclass is the Fe/edta/NO species. Its relevance in the application-oriented flue gas area in engineering science was mentioned in chapter 1.3.2. The speculative molecular structure of the hitherto crystallographically uncharacterized Fe/edta/NO species was already presumed in several publications on the basis of various spectroscopic and computational techniques.[61,62,67,116] Knowledge of its structural chemistry is certainly an essential factor for optimizing NO_x removal efficiency. Furthermore, as seen from chapter 1.3.1, the $\{FeNO\}^7$(S = 3/2) compounds have been proposed as relevant intermediates in the enzymatically catalyzed NO reduction process of microorganisms. Structure analysis on related model complexes can provide helpful insights into the fundamental chemistry of these enzymes. The lack of structural data on $\{FeNO\}^7$(S = 3/2) compounds with the concomitant presence of aqua and nitrosyl ligands becomes particularly apparent in a recent publication by Cracken *et al*..[38] In trying to model the so-called facial triad (two histidine and one carboxylate ligands) of mononuclear non-heme iron oxygenases by aminecarboxylato ligands, advanced EPR technology was used in order to elucidate the structures of the aminecarboxylate-aqua-$\{FeNO\}^7$ model compounds. X-ray analyses on the model complexes would surely have supported the research studies.

Thus, the overall goal of this thesis is to close the knowledge gap about the structural chemistry of stable quartet-$\{FeNO\}^7$ complexes with aminecarboxylates. To elucidate the molecular structure with single-crystal X-ray diffraction, high-purity crystals of the target compounds had to be synthesized. After crystallization, the complex structures were modelled by means of quantum-chemical calculations in order to get insight into their electronic configuration and, furthermore, to analyze structural peculiarities. The X-ray and the computational results were expected to contribute to an understanding of the complex stability and to establish a correlation between the stability and the structure of the nitrosyl compounds. In addition, the $\{FeNO\}^7$(S = 3/2) compounds are model compounds for a DFG priority program that deals with the "influence of local transport processes in chemical reactions in bubble flows". In this context, the Fe–NO reaction system was investigated in two engineering collaborations with Dr. Günter Rinke and Dipl. Ing. Daniela Schurr[117,118] from the Institute for Microprocess Engineering of the

Karlsruhe Institute of Technology and with Prof. Dr. Christian Kähler and M.Sc. Katharina Haase[119] from the Institute of Fluidmechanics and Aerodynamics of the *Bundeswehr* University Munich.

2 Results

2.1 Stable {FeNO}^{7}(S = 3/2) complexes with aminecarboxylates

The first chapter of the RESULTS PART deals with the crystal synthesis, the description of the molecular structures as well as with the IR and UV/Vis characterization of the nitrosyl-iron complexes. During the research for this thesis, four new crystalline quartet-{FeNO}^{7} compounds with the co-ligands ethylenediamine-*N*,*N*′-diacetate (edda), nitrilotriacetate (nta), *N*,*N*′-bis(2-hydroxyethyl)ethylene-diamine-*N*,*N*′-diacetate (bhedda) and ethylenediamine-*N*,*N*,*N*′,*N*′-tetraacetate (edta) were synthesized.

2.1.1 Synthesis of crystalline {FeNO}^{7}(S = 3/2) complexes

The aqueous nitrosyl-iron compounds were synthesized following a published procedure by van Eldik *et al.*[86–89] The chelating ligand in its acid form (LH_n) and sodium or potassium hydroxide as the base were stirred in water before iron(II) sulfate heptahydrate was added in stoichiometric amounts to the aminecarboxylato co-ligand. Immediately after adding the iron salt, the reaction solution was treated with gaseous nitric oxide to avoid the precipitation of the iron(II) aminecarboxylate precursor complex. Within a few minutes the almost colorless precursor solution turned into the characteristic dark green color of the {FeNO}^{7}(S = 3/2) chromophore. Black crystalline {FeNO}^{7}(S = 3/2) complexes were obtained by the isothermal diffusion of acetone or ethanol into the reaction solutions. In general, the aqueous solutions of the nitrosyl species are stable against NO loss upon stripping with inert gas or upon subjection to low pressure. They are stable under inert gas atmosphere but oxidize quite rapidly when exposed to atmospheric oxygen. All crystalline products are air stable. The general synthetic route is shown in Scheme 2.1.

$$FeSO_4 \cdot 7H_2O + LH_n + NO(g) \underset{Na_2SO_4/K_2SO_4}{\overset{NaOH/KOH}{\rightleftharpoons}} [Fe(NO)(L)] + (7+n)\,H_2O$$

Scheme 2.1: Synthetic route to {FeNO}^{7}(S = 3/2) complexes with aminecarboxylates. LH_n: the free acid of the aminecarboxylato co-ligand.

2.1.2 [Fe(edda)(H_2O)(NO)] (**1**)

Black crystals of (*OC*-6-14)-aquaethylenediamine-*N,N*′-diacetatonitrosyliron hemihydrate (**1b** · ½ H_2O) were obtained from an aqueous solution of gaseous nitric oxide and equimolar amounts of iron(II) sulfate heptahydrate and fully neutralized ethylenediamine-*N,N*′-diacetic acid by the diffusion of acetone over three weeks. **1b** · ½ H_2O crystallized in the triclinic space group $P\bar{1}$ with four formula units in the primitive

cell. The asymmetric unit contains two independent complex molecules which do not significantly differ from each other in terms of bond angles and bond lengths. The iron center is octahedrally coordinated by the tetradentate ligand edda via three five-membered chelate rings. Nitric oxide coordinates in *trans* position to a nitrogen donor atom of the chelating ligand and the single free coordination site is occupied by an aqua ligand. The average Fe–N–O angle is 148°. All equatorial donor atoms are tilted away from the nitrosyl ligand, resulting in an average N1–Fe–O2/O3/N3/O91 angle of 96°. The molecular structure in crystals of **1b** · ½ H_2O is shown in Figure 2.1. For reasons of clarity, only one complex molecule is illustrated.

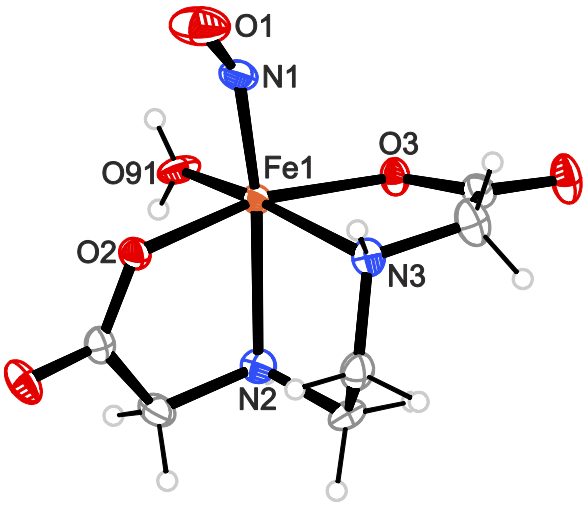

Figure 2.1: ORTEP plot of one of two symmetrically independent molecules in crystals of **1b** · ½ H_2O (50% probability level). Space group: $P\bar{1}$. Interatomic distances (Å) and angles (°) with the standard deviation of the last digit in parentheses: Fe1−N1 1.775(3), Fe1−O2 2.004(2), Fe1−N3 2.173(3), Fe1−N2 2.231(3), Fe1−O3 2.086(2), Fe1−O91 2.070(3), N1−O1 1.163(3), Fe1−N1−O1 147.8(3), N1−Fe1−O2 89.93(11), N1−Fe1−O91 97.26(13), N1−Fe1−O3 101.07(11), N1−Fe1−N3 97.03(12), N1−Fe1−N2 168.61(12). Data of the second independent complex molecule: Fe1'−N1' 1.775(3), Fe1'−O2' 2.019(2), Fe1'−N3' 2.165(3), Fe1'−N2' 2.229(3), Fe1'−O3' 2.089(2), Fe1'−O91' 2.058(3), N1'−O1' 1.158(3), Fe1'−N1'−O1' 148.5(2), N1'−Fe1'−O2' 90.23(11), N1'−Fe1'−O91' 95.53(13), N1'−Fe1'−O3' 100.78(11), N1'−Fe1'−N3' 97.28(12), N1'−Fe1'−N2' 168.43(11). Exact assignment of atoms in the crystallographic data of the second independent complex molecule N1'=N4, N2'=N5, N3'=N6, O1'=O6, O2'=O7, O3'=O8, O91'=O92.

Both complex molecules in the asymmetric unit form hydrogen bonds to neighboring coordination entities. The aqua ligands and the water of crystallization form hydrogen bonds among each other as well as to neighboring non-metal bonded carboxyl-oxygen atoms of carboxylate groups. The hydrogen atoms of the amine groups form hydrogen bonds to neighboring carboxyl-oxygen atoms. Three cyclic motifs are formed with the descriptors $R_6^4(16)$ (tertiary graph-set O93−H931···O9^{i}···H76−N6−Fe2−O92−H922···O93^{iii}−H931^{iii}···O9^{v}···H76^{iii}−N6^{iii}−Fe2^{iii}−O92^{iii}−H922^{iii}), $R_2^2(8)$ (binary graph-set O5···H921^{i}−O92^{i}−Fe2^{i}−N5^{i}−H75^{i}···O3−C4) and $R_1^1(13)$ (unitary graph-set N6−H76···O9^{i}−C12^{i}−O7^{i}−Fe2^{i}−N6^{i}−H76^{i}···O9−C12−O7−Fe2) according to graph-set analysis.[2,3] Table 2.1 gives an overview of all

hydrogen bonds in crystals of **1b**· ½ H_2O and a schematic illustration of the hydrogen-bond network in crystals of **1b**· ½ H_2O is shown in Figure 2.2.

Table 2.1: Hydrogen bonds in crystals of **1b** · ½ H_2O with H···A < r(A) + 2 Å and ∢(DHA) > 110°.

D−H···A	d(D−H)	d(H···A)	d(D···A)	∢(DHA)
N6−H76···O9^{i}	0.76(3)	2.19(3)	2.929(4)	168(4)
N5−H75···O3^{i}	0.88(3)	2.23(3)	3.008(4)	146(3)
N3−H73···O4^{ii}	0.84(3)	2.12(3)	2.944(4)	166(3)
O91−H911···O10^{iii}	0.82(4)	1.90(4)	2.711(4)	167(4)
O91−H912···O10^{iv}	0.73(4)	1.97(4)	2.683(4)	164(4)
O92−H921···O5^{i}	0.72(4)	1.96(4)	2.668(4)	171(5)
O92−H922···O93^{iii}	0.79(5)	1.82(5)	2.604(4)	169(4)
O93−H931···O9^{i}	0.81(4)	1.96(4)	2.762(4)	167(4)
O93−H932···O5^{v}	0.85(5)	1.92(5)	2.703(4)	154(5)

Symmetry code: ^{i} −*x*, −*y*+1, −*z*+1; ^{ii} −*x*+1, −*y*+2, −*z*; ^{iii} −*x*+1, −*y*+1, −*z*+1; ^{iv} *x*, *y*+1, *z*; ^{v} −*x*, −*y*+1, −*z*; ^{vi} *x*+1, *y*, *z*.

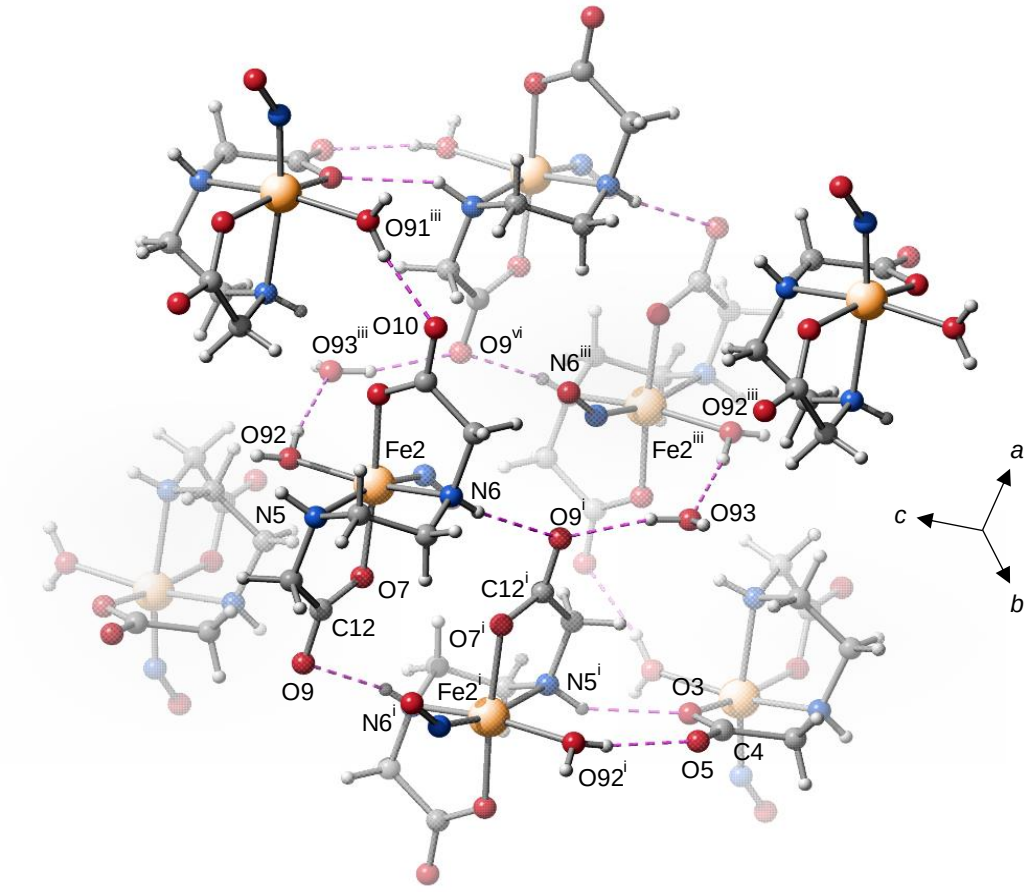

Figure 2.2: SCHAKAL illustration of the hydrogen-bond pattern (dashed pink lines) in crystals of **1b** · ½ H_2O.

2.1.3 $[\{Fe(H_2O)_4\}\{Fe(NO)(nta)\}_2]_{n/n} \cdot 2\ H_2O = [Fe(H_2O)_4(\mathbf{2})_2]_{n/n} \cdot 2\ H_2O$

Greenish-black crystals of the coordination polymer $[Fe(H_2O)_4(\mathbf{2})_2]_{n/n} \cdot 2\ H_2O$ with $[Fe(NO)(nta)]^-$ (**2**) as the nitrosyl-containing building block were obtained from an equimolar solution of iron(II) sulfate heptahydrate, partly neutralized nitrilotriacetic acid and gaseous nitric oxide by the diffusion of acetone and ethanol over one year. The compound crystallized in the orthorhombic space group *Pbca* with eight formula units in the primitive cell. Crystal-structure analysis reveals an Fe/nta molar ratio of 3:2 instead of the supplied 1:1 proportion. However, the equimolar ratio is maintained in the nitrosyl-containing anion $[Fe(nta)(NO)]^-$ (**2**). The structure of the anionic building unit (*OC*-6-11)-nitrilotriacetatonitrosylferrate (**2**) is illustrated in Figure 2.3.

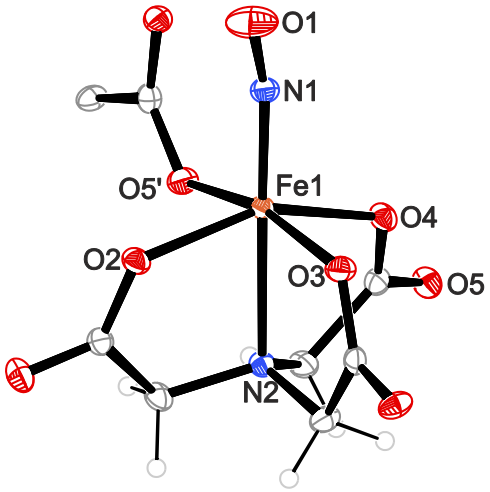

Figure 2.3: ORTEP plot of the anion **2** including a carboxylate residue of an adjacent complex unit in the coordination polymer $[Fe(H_2O)_4(\mathbf{2})_2]_{n/n} \cdot 2\ H_2O$ (50% probability level). Space group *Pbca.* Interatomic distances (Å) and angles (°) with the standard deviation of the last digit in parentheses: Fe1−N1 1.752(3), Fe1−O2 2.072(2), Fe1−N2 2.226(3), Fe1−O3 2.055(2), Fe1−O4 2.086(2), Fe1−O5 2.073(2), N1−O1 1.152(3), Fe1−N1−O1 164.8(3), N1−Fe1−O2 99.01(11), N1−Fe1−O5 100.80(11), N1−Fe1−O4 106.79(11), N1−Fe1−O3 93.21(11), N1−Fe1−N2 172.93(11).

The iron center is coordinated octahedrally by the tetradentate chelating ligand via three five-membered chelate rings and the nitrosyl ligand binds *trans* to the nitrogen donor atom of the chelating ligand. A non-metal bonded carboxyl-oxygen atom from an adjacent $[Fe(nta)(NO)]^-$ building unit fills the remaining coordination site. The bond angle in the Fe–N–O moiety is 165°. All equatorial donor atoms bend away from the nitrosyl group and an average N1–Fe–O2/O3/O4/O5´ angle of 100° results. The entire crystal is a "higher-order" coordination polymer. Pentacoordinate $[Fe(nta)(NO)]^-$ building units attain hexacoordination by forming a one-dimensional, zigzag-shaped polyanion. The lateral carboxylate-oxygen atoms of these polyanions complete planar dicationic $[Fe(H_2O)_4]^{2+}$ moieties—instead of the attempted sodium counterions—to octahedra by two trans linkages from two parallel-arranged polyanions. Alternating blocks of repeating zigzag-shaped ···Fe−NO···Fe−NO···Fe−OH_2···Fe−NO··· Fe−NO··· entities are formed along [001]. These elements are stabilized via hydrogen bonds between

the carboxylate groups of the Fe/NO/nta building blocks and the aqua ligands of the $[Fe(H_2O)_4]^{2+}$ moieties. The water of crystallization forms hydrogen bonds to the aqua ligands of the bridging $[Fe(H_2O)_4]^{2+}$ units as well as to the lateral carboxylate-oxygen atoms of the polyanions. Three cyclic motifs exist with the descriptors $R_4^3(8)$ (quaternary graph-set H931^{ii}···O92−H921···O6^{i}···H911^{vi}−O91^{vi}−H912^{vi}···O93^{ii}), $R_3^3(10)$ (tertiary graph-set O93^{ii}−H932^{ii}···O7^{iii}−C4^{iii}−O3^{iii}−Fe1^{iii}−O2^{iii}···H922−O92···H931^{ii}) and $R_2^2(8)$ (binary graph-set H911^{v}···O6^{iii}−C6^{iii}−O2^{iii}···H922−O92−Fe2−O91^{v}) according to graph-set analysis.[2,3] Figure 2.4 shows the hydrogen-bond network in the coordination polymer and Table 2.2 lists all hydrogen bonds.

Table 2.2: Hydrogen bonds in crystals of $[Fe(H_2O)_4(\mathbf{2})_2]_{n/n} \cdot 2\ H_2O$ with H···A < r(A) + 2 Å and ∢(DHA) > 110°.

D−H···A	d(D−H)	d(H···A)	d(D···A)	∢(DHA)
O92−H921···O6^{i}	0.71	2.01	2.691(3)	159.6
O91−H911···O6^{ii}	0.86	1.91	2.691(3)	149.6
O91−H912···O93^{i}	0.80(5)	1.93(5)	2.700(3)	163(5)
O92−H922···O2^{iii}	0.98(5)	1.85(5)	2.826(3)	173(4)
O93−H931···O92	0.85(5)	2.20(5)	3.048(4)	173(5)
O93−H932···O7^{iv}	0.83(4)	2.10(5)	2.920(3)	166(4)

Symmetry code: ^{i} x+1/2, −y+1/2, −z+1; ^{ii} x+1, y, z; ^{iii} −x+1, −y+1, −z+1; ^{iv} x−1, y, z; ^{v} −x+2, −y+1, −z+1; ^{vi} x−1/2, −y+1/2, −z+1.

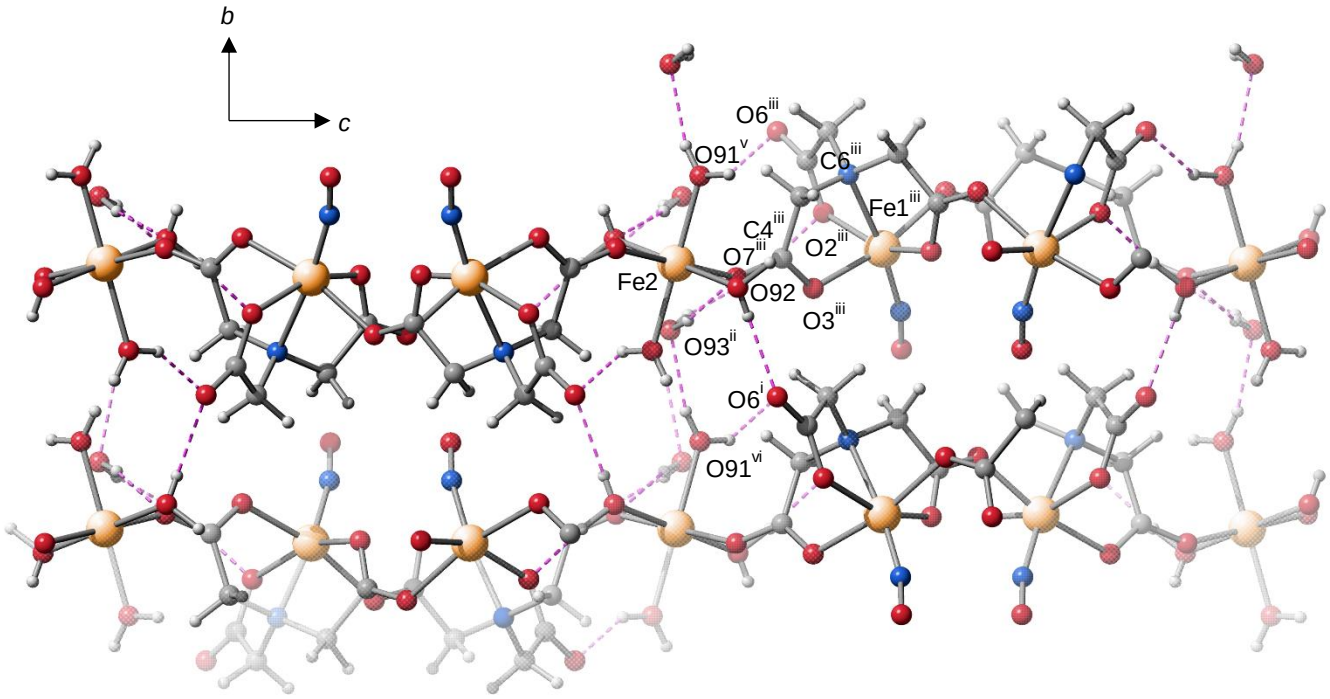

Figure 2.4: SCHAKAL plot of a cutout of the polymeric structure and the hydrogen-bond network (dashed pink lines) in crystals of $[Fe(H_2O)_4(\mathbf{2})_2]_{n/n} \cdot 2\ H_2O$ with view along [100].

2.1.4 [Fe(bhedda)(NO)] (**3**)

The chelating ligand *N*,*N*′-bis(2-hydroxyethyl)ethylenediamine-*N*,*N*′-diacetate (bhedda) was synthesized following a published procedure by Wensel and Meares.[120] *N*,*N*′-bis(2-hydroxyethyl)-*N*,*N*′-ethylenediamine was reacted with two equivalents of bromoacetic acid in an alkaline aqueous solution. The $^{13}C\{^{1}H\}$-NMR spectrum of the reaction solution shows the characteristic chemical shifts for K_2(bhedda) (Table 2.3) but some additional non-assignable signals are found as well (see EXPERIMENTAL PART).

Table 2.3: $^{13}C\{^{1}H\}$-NMR data for K_2(bhedda) in aqueous solution. Chemical shifts δ in ppm.

-<u>C</u>OO	OOC-<u>C</u>H$_2$-N	N-<u>C</u>H$_2$-CH$_2$-OH	N-CH$_2$-<u>C</u>H$_2$-OH	N-<u>C</u>H$_2$-<u>C</u>H$_2$-N
176.4	58.1	57.4	56.6	51.6

The reaction solution was treated with an equivalent molar amount of iron(II) sulfate heptahydrate, referring to *N*,*N*′-bis(2-hydroxyethyl)-*N*,*N*′-ethylenediamine, to form the colorless [Fe^{II}(bhedda)] (**6**) complex in 22% yield. **6** was characterized by X-ray crystallography (see chapter 2.2.2) and mass spectrometry. (FAB$^-$) and (FAB$^+$) mass spectra show the characteristic molecular ion peaks $[M-H]^-$ at 317.2 *m/z* and $[M+H]^+$ at 319.2 *m/z*, respectively. An aqueous solution of **6** was then reacted with gaseous nitric oxide in order to synthesize the nitrosyl-iron complex **3**. The synthetic route is illustrated in Scheme 2.2.

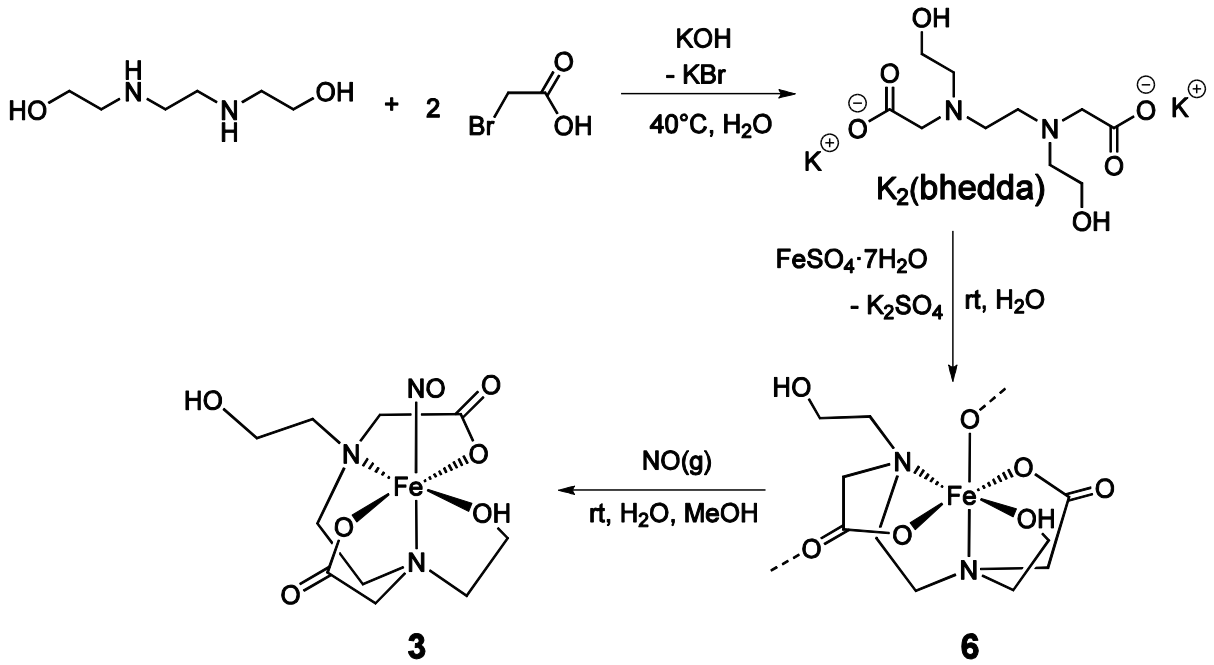

Scheme 2.2: Synthetic route to (*OC*-6-14)-*N*,*N*′-bis(2-hydroxyethyl)ethylenediamine-*N*,*N*′-diacetatonitrosyliron (**3**) and (*OC*-6-13)-*N*,*N*′-bis(2-hydroxyethyl)ethylenediamine-*N*,*N*′-diacetatoiron(II) (**6**).

The crystallization of **3** from aqueous solution was hampered but it succeeded with methanol as the reaction medium. One brownish-black crystal of (*OC*-6-14)-*N,N'*-bis(2-hydroxyethyl)ethylenediamine-*N,N'*-diacetatonitrosyliron(**3**) was isolated from a methanolic solution by the diffusion of acetone over two weeks. The structure solution succeeded in the monoclinic space group $P2_1/c$ with four formula units in the primitive cell. The molecular structure in crystals of **3** is shown in Figure 2.5.

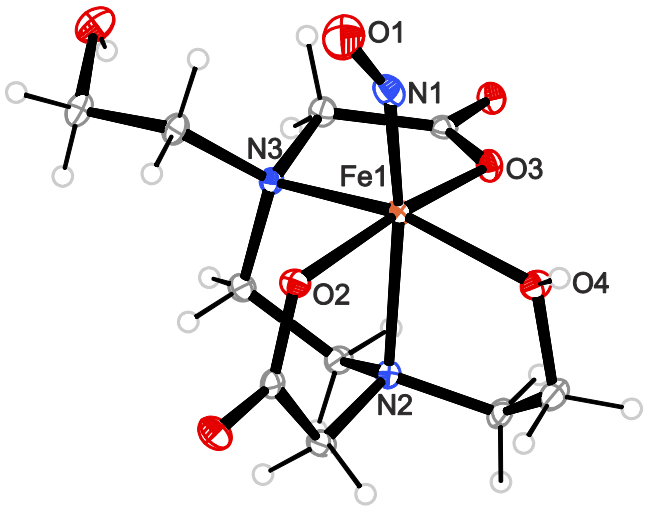

Figure 2.5: ORTEP plot of the molecular structure of the solvent-free mononuclear entity in crystals of **3** (50% probability level). Space group $P2_1/c$. Interatomic distances (Å) and angles (°), the standard deviation of the last digit is given in parentheses: Fe1−N1 1.782(2), Fe1−O2 2.026(1), Fe1−N3 2.242(2), Fe1−N2 2.215(2), Fe1−O3 2.045(1), Fe1−O4 2.079(1), N1−O1 1.134(2), Fe1−N1−O1 150.20(15), N1−Fe1−O2 89.90(6), N1−Fe1−O4 103.95(6), N1−Fe1−O3 101.82(6), N1−Fe1−N3 98.99(6), N1−Fe1−N2 169.22(6).

The asymmetric unit contains one complex molecule of [Fe(bhedda)(NO)] (**3**). **3** consists of an iron atom that is octahedrally coordinated by the nitrosyl ligand and by the potentially hexadentate chelating ligand via the carboxylate-oxygen atoms, the nitrogen donor atoms and the oxygen atom of one hydroxyethyl function. The other hydroxyethyl function bends away from the iron atom in order to attain octahedral coordination. Nitric oxide is bound in *trans* position to a nitrogen donor atom of the bhedda co-ligand. The Fe–N–O bond angle is 150°. All equatorial donor atoms of the chelating ligand are tilted away from the nitrosyl group, the average N1–Fe–O2/O3/O4/N3 angle is 98°. Both hydroxyethyl groups of the co-ligand form hydrogen bonds to acetate groups of adjacent formula units (Figure 2.6 and Table 2.4). A ring motif is formed with the descriptor $R_2^2(12)$ (binary graph-set C7−C8−N3−C9−C10−O7−H87···O2^{i}−Fe1^{i}−O4^{i}−H84^{i}···O6) according to graph-set analysis.[2,3]

Table 2.4: Hydrogen bonds in crystals of **3** with H···A < r(A) + 2 Å and ∢(DHA) > 110°.

D−H···A	d(D−H)	d(H···A)	d(D···A)	∢(DHA)
O7−H87···O2^{i}	0.84	2.08	2.9054(19)	168.4
O4−H84···O6^{ii}	0.81(3)	1.76(3)	2.5495(18)	168(3)

Symmetry code: ^{i} *x*, *y*−1, *z*; ^{ii} *x*, *y*+1, *z*.

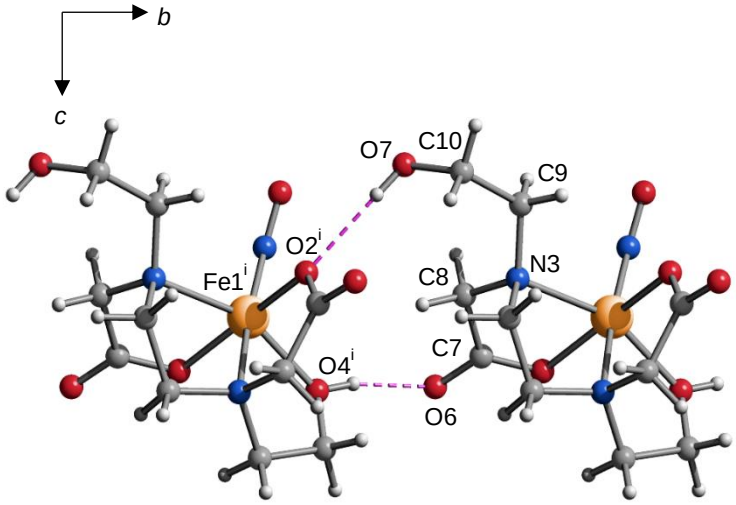

Figure 2.6: SCHAKAL graphic of the hydrogen-bond pattern (dashed pink lines) in crystals of **3** with view along [100].

2.1.5 $[\{Fe(H_2O)_2\}\{Fe(NO)(Hedta)\}_2]_{n/n}$ = $[Fe(H_2O)_2(\mathbf{4})_2]_{n/n}$

Large black crystals of the polymeric compound $[\{Fe(H_2O)_2\}\{Fe(NO)(Hedta)\}_2]_{n/n}$ = $[Fe(H_2O)_2(\mathbf{4})_2]_{n/n}$ were obtained from an equimolar solution of iron(II) sulfate heptahydrate, partly neutralized ethylenediamine-*N*,*N*,*N*′,*N*′-tetraacetic acid and gaseous nitric oxide by the diffusion of acetone over six months. Crystal-structure analysis reveals an Fe/edta molar ratio of 3:2 instead of the supplied 1:1 proportion. The structure solution succeeded in the monoclinic space group $P2_1/c$ with four formula units in the primitive cell. Figure 2.7 shows the structure of the nitrosyl-containing monoanion (*OC*-6-31)-ethylenediamine-*N,N,N′,N′*-tetraacetatonitrosylferrate (**4**). The iron atom is octahedrally coordinated by three carboxylate-oxygen atoms and the two nitrogen donor atoms of the co-ligand via four five-membered chelate rings. Nitric oxide binds in *trans* position to a nitrogen donor atom of the co-ligand. One of the four carboxylate groups is protonated and bends away from the iron center. The Fe–N–O bond angle measures 149°. All equatorial donor atoms of the co-ligand are tilted away from the nitrosyl group and a mean N1–Fe–O2/O3/O4/N3 angle of 99° results. The pH-value relevance of the mother liquor becomes apparent here: fairly acidic conditions have to be met to support the dangling non-deprotonated carboxymethyl function of the $[Fe(H_2O)_2(\mathbf{4})_2]_{n/n}$ species.

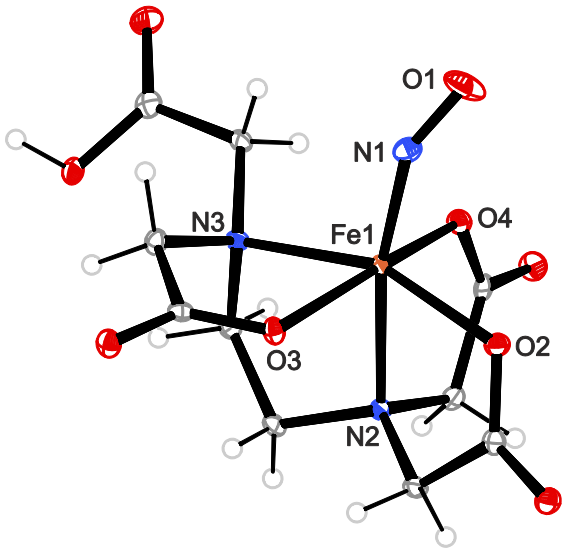

Figure 2.7: ORTEP plot of $[Fe(Hedta)(NO)]^-$ (**4**) monoanions in crystals of $[Fe(H_2O)_2(\mathbf{4})_2]_{n/n}$ (50% probability level). Space group $P2_1/c$. Interatomic distances (Å) and angles (°), the standard deviation of the last digit is given in parentheses: Fe1−N1 1.763(2), Fe1−O2 2.055(2), Fe1−N3 2.241(2), Fe1−N2 2.196(2), Fe1−O3 2.069(2), Fe1−O4 1.999(2), N1−O1 1.158(2), Fe1−N1−O1 148.8(2), N1−Fe1−O2 94.95(7), N1−Fe1−O4 91.70(7), N1−Fe1−O3 102.11(7), N1−Fe1−N3 106.37(7), N1−Fe1−N2 168.53(7). Data of the bridging diaquairon(II) moieties: Fe2−O5 2.141(1), Fe2−O7 2.108(1), Fe2−O91 2.128(2).

Anions **4** and $[Fe(H_2O)_2]^{2+}$ cations—instead of the attempted potassium counterions—form two-dimensional building blocks with layers along [100]. Within these 2D-blocks, a square net of $[Fe(H_2O)_2]^{2+}$ building units is connected via iron-carboxyl-oxygen contacts to square anion assemblies above and below, resulting in the AB_2-type stoichiometry of the compound. The crystal structure is stabilized via hydrogen bonds between the carboxylate groups and the aqua ligands of the bridging $[Fe(H_2O)_2]^{2+}$ moieties. The bonded hydrogen atom of the dangling carboxymethyl function forms a hydrogen bond to a carboxyl-oxygen atom of a neighboring anionic building unit. Three cyclic motifs exist with the descriptors $R_3^3(15)$ (tertiary graph-set $H912^{vi}\cdots O3^{ii}-Fe1^{ii}-N3^{ii}-C9^{ii}-C10^{ii}-O9^{ii}-H89^{ii}\cdots O6^{v}-C4^{v}-O4^{v}-Fe1^{v}-O2^{v}\cdots H911^{vi}-O91^{vi}$), $R_1^1(6)$ (unitary graph-set $O91^{ii}-H912^{ii}\cdots O3^{iv}-C6^{iv}-O7^{iv}-Fe2^{iv}$) and $R_1^1(6)$ (unitary graph-set $O91^{ii}-H911^{ii}\cdots O2-C1-O5-Fe2$) according to graph-set analysis.[2,3] Figure 2.8 illustrates the hydrogen-bond network in the coordination polymer $[Fe(H_2O)_2(\mathbf{4})_2]_{n/n}$ and Table 2.5 lists all hydrogen bonds.

Table 2.5: Hydrogen bonds in crystals of $[Fe(H_2O)_2(\mathbf{4})_2]_{n/n}$ with H···A < r(A) + 2 Å and ∢(DHA) > 110°.

D−H···A	d(D−H)	d(H···A)	d(D···A)	∢(DHA)
O9−H89···O6^{i}	0.90	1.81	2.673(2)	158.4
O91−H911···O2^{ii}	0.98	1.78	2.716(2)	157.0
O91−H912···O3^{iii}	0.91	1.91	2.776(2)	159.0

Symmetry code: ^{i} x+1/2, −y+3/2, z; ^{ii} −x+1, −y, −z; ^{iii} −x+3/2, y−1/2, −z; ^{iv} x−1/2, −y+1/2, z; ^{v} −x+1/2, y−1/2, −z; ^{vi} x−1/2, −y−1/2, z.

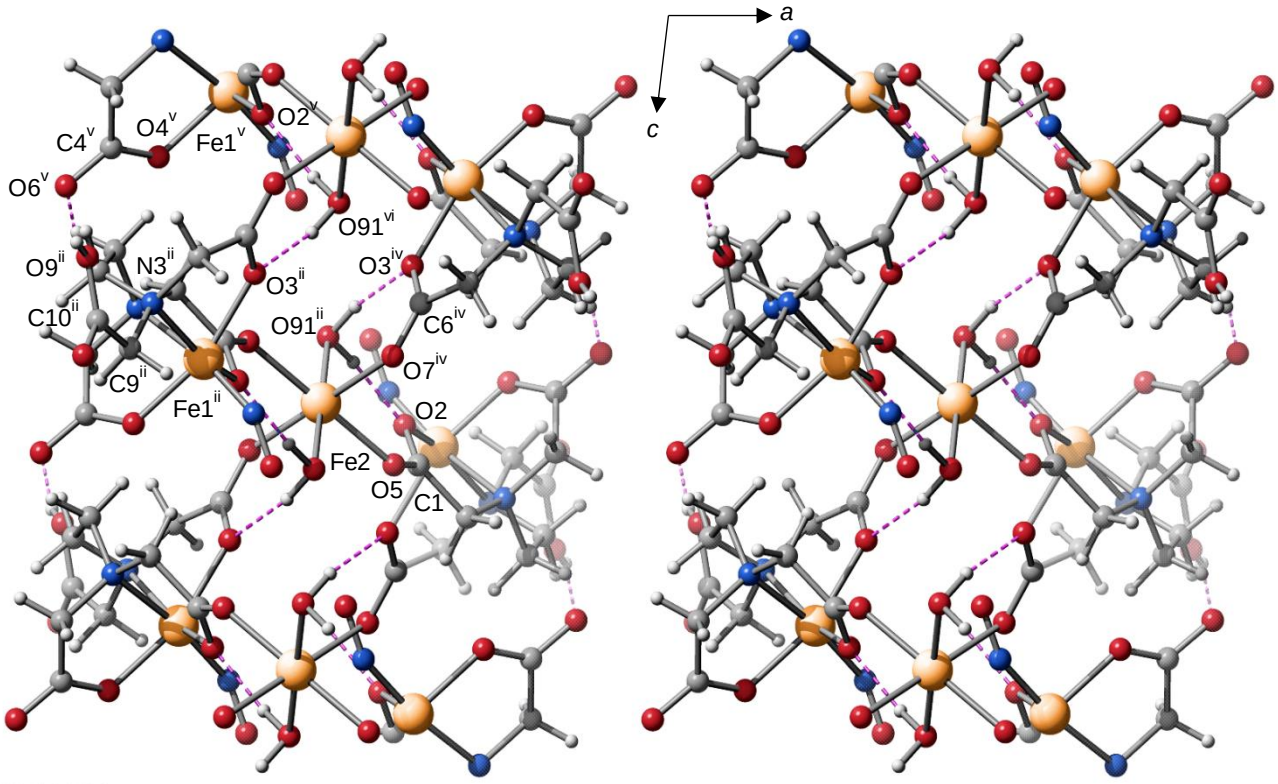

Figure 2.8: SCHAKAL plot of a cutout of the polymeric structure and the hydrogen-bond pattern (dashed pink lines) in crystals of $[Fe(H_2O)_2(\mathbf{4})_2]_{n/n}$ with view along $[0\bar{1}0]$.

2.1.6 IR- and UV/Vis-analytical characterization

Besides X-ray crystallography, the formation of the $\{FeNO\}^7$ (S = 3/2) compounds was analyzed with IR- and UV/Vis spectroscopy. In general, the spectra of the reaction solution as well as of the crystalline compound are in good agreement. A typical UV/Vis-spectrum shows two charge transfer bands around 330 nm and 430 nm and a d-d transition band at around 600 nm. The characteristic N–O stretching vibration bands are found in the range between 1761 cm^{-1} and 1791 cm^{-1}. The IR- and UV/Vis-spectroscopic data are summarized in Table 2.6. Because of the strong water-absorption band in the region of the NO-stretching vibration, IR spectra of the dissolved complexes were recorded in D_2O. Figure 2.9 shows the IR spectrum of the crystalline coordination polymer $[Fe(H_2O)_2(\mathbf{4})_2]_{n/n}$ as well as a comparison of the UV/Vis spectra of the crystalline compound $[Fe(H_2O)_2(\mathbf{4})_2]_{n/n}$ and its mother liquor.

Table 2.6: IR- and UV/Vis-spectroscopic data of complexes **1b**–**4** (sol.: aqueous reaction solution, cry.: crystalline compound). The absorption maxima given in the cry. column were determined from Kubelka-Munk[121]-transformed reflectance spectra. Data for solid-state measurements on **3** are missing because of the low crystal yield.

	$\tilde{\nu}$(NO)/cm^{-1} (sol.)	$\tilde{\nu}$(NO)/cm^{-1} (cry.)	λ/nm (sol.)	λ/nm (cry.)
1(**b**)	1769	1761	342, 435, 617.	414, 430, 644.
2	1793	1791	339, 439, 602.	433, 622.
3	1782	-	337, 422, 650.	-
4	1777	1781	342, 435, 634.	432, 623.

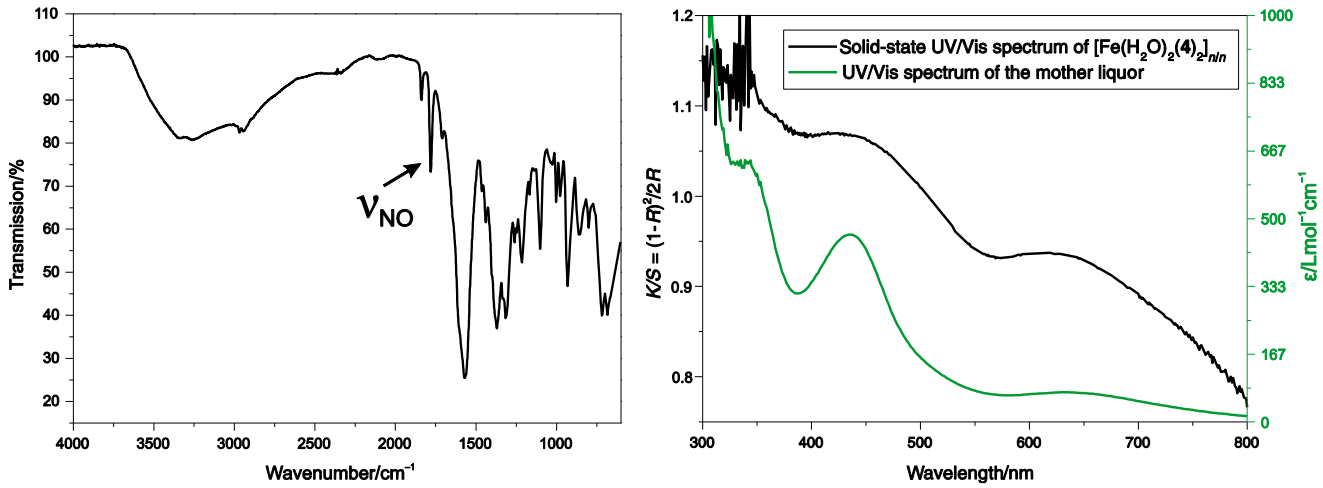

Figure 2.9: Left: IR spectrum of the crystalline coordination polymer $[Fe(H_2O)_2(\mathbf{4})_2]_{n/n}$; right: UV/Vis spectra of the crystalline coordination polymer $[Fe(H_2O)_2(\mathbf{4})_2]_{n/n}$ and its mother liquor.

2.1.7 The crystallization of stable {FeNO}^{7}(S = 3/2) complexes with amine-carboxylates

The pH value of the mother liquors before and after the treatment with gaseous nitric oxide had significant influence on the crystallization process of the nitrosyl-iron compounds. Table 2.7 summarizes the pH values of the mother liquors of complexes **1**−**4** before and after the treatment with nitric oxide. Slightly acidic conditions were necessary to obtain crystalline products. Buffers were not used because of their pronounced tendency to crystallize from aqueous solution. pH values of eight and higher promoted the oxidation of Fe^{II} to Fe^{III} and led to the fast decomposition of the compounds.

Table 2.7: pH values of the aqueous reaction solutions of complexes **1**−**4** before and after NO absorption.

	1	**2**	**3**	**4**
Before NO treatment	6	3−4	4	3−4
After NO treatment	5−6	5	5−6	4−5

The crystallization of the {FeNO}^{7}(S = 3/2) complexes lasted from two weeks for compound **3** to one year for the complex polymer $[Fe(H_2O)_4(\mathbf{2})_2]_{n/n} \cdot 2\ H_2O$. The crystallization of **3**, $[Fe(H_2O)_4(\mathbf{2})_2]_{n/n} \cdot 2\ H_2O$ and $[Fe(H_2O)_2(\mathbf{4})_2]_{n/n}$ was hampered and not reproducible. Compound **3** was isolated as one single crystal, sufficient for a X-ray measurement. Further crystallization experiments under analogous reaction conditions were unsuccessful. Crystal synthesis from the crystalline precursor compound **6** · H_2O was ineffective as well. The polymeric compounds with the nitrosyl-containing building blocks **2** and **4** were merely isolated from mother liquors, as described in the EXPERIMENTAL PART, with acidic conditions and sodium or potassium hydroxide as the base. Even though the anticipated sodium or potassium counterions are not found in the polymeric structures of $[Fe(H_2O)_4(\mathbf{2})_2]_{n/n} \cdot 2\ H_2O$ and $[Fe(H_2O)_2(\mathbf{4})_2]_{n/n}$, crystalline products could not be obtained when lithium hydroxide, cesium hydroxide or rubidium hydroxide were used as bases (acidic conditions were fulfilled). The addition of salts with sterically demanding cations such as bis(triphenylphosphine)iminium chloride and benzyltrimethylammonium hydroxide in order to improve the crystallization tendency had no success. Moreover, the use of choline hydroxide as a base (the choline counterion was expected to form a strong hydrogen-bond network in the crystal structure of the nitrosyl compound) did not lead to a crystalline product. The crystal structures of the polymeric compounds $[Fe(H_2O)_4(\mathbf{2})_2]_{n/n} \cdot 2\ H_2O$ and $[Fe(H_2O)_2(\mathbf{4})_2]_{n/n}$ reveal a 3:2 iron:amine-carboxylate molar ratio instead of the supplied 1:1 proportion. Their mother liquors obviously “lost” some bonded nitric oxide so that one third of the iron atoms can serve as bridging building-block entities. Subsequent crystallization experiments were performed with magnesium sulfate (an aquated magnesium ion was expected to adopt the position of the bridging dicationic $[Fe(H_2O)_{4/2}]^{2+}$ moieties) in order to examine whether the use of exact stoichiometric amounts would accelerate the crystallization of the complex polymers. Magnesium was used because it is not able to form a nitrosyl complex or an aminecarboxylate complex that is more stable than the iron complex. But these crystallization attempts were not effective. Nevertheless, **1b** · ½ H_2O crystallized reproducibly from its mother liquor. The

isothermal diffusion of acetone accelerated the crystallization but the complex was also isolated directly from aqueous solution. Moreover, **1b** · ½ H_2O was obtained from the low-scaled IR reaction mixture with D_2O instead of H_2O as the solvent.

2.1.8 Synthesis of nitrosyl-iron complexes with amino acids

As part of this thesis, the crystallization of nitrosyl-iron complexes with the amino acids gly, ser, thr, asp, cys, tyr, leu, phe, thr and his as co-ligands was attempted. When the complexes were synthesized in aqueous solution with iron(II) sulfate heptahydrate as the iron salt, the dark green reaction solutions of the nitrosyl-iron complexes adopted a distinct red coloring after about one day. This indicated the oxidation of Fe^{II} to Fe^{III}. The red coloring was also observed when methanol or ethanol were used as solvents. Thus, the syntheses were carried out in the absence of water in aprotic polar solvents. Iron(II) triflate was utilized as the anhydrous iron source, TEA as the base and MeCN, DMF or a DMF/MeCN mixture as the solvent. The amino acids were applied in their L-configuration or as racemic mixtures. Racemic mixtures were used in order to raise the number of potential space groups in the case of crystallization. Further syntheses were performed with the bidentate auxiliary ligands acac, tmeda, bpy and phen, whereby the tridentate amino acids his, asp, ser and thr were used as co-ligands. Hence, the coordination of solvent molecules was avoided and the crystallization tendency of the compounds would be increased. When a suspension of the amino acid, iron(II) triflate, TEA and the auxiliary ligand (if desired) was treated with nitric oxide, a color change from yellowish-green (orange when acac was used as the auxiliary ligand, red in the case of bipy or phen) to dark reddish-brown was observed. This was taken as an indicator for the successful formation of a nitrosyl species. The IR-spectra of the reaction solutions showed vibration bands, although of low intensity, in the range of the characteristic N–O stretching vibration of $\{FeNO\}^7$(S = 3/2) complexes. Even though the crystallization of an nitrosyl-iron compound was unsuccessful (see EXPERIMENTAL PART for further details), some amorphous black solids were isolated. The N–O stretching vibration bands of the reaction solutions and the solids are in good agreement (see Table 2.8).

Table 2.8: N–O stretching vibration bands of the solid Fe/gly/NO, Fe/acac/his/NO, Fe/asp/NO, Fe/asp/tmeda/NO and Fe/tyr/NO species as well as of their reaction solutions.

Species	$\tilde{\nu}$(NO)/cm^{-1} (solution)	$\tilde{\nu}$(NO)/cm^{-1} (solid)
Fe/gly/NO	1789, 1740	1799, 1731
Fe/acac/his/NO	1779	1792
Fe/asp/NO	1817	1818
Fe/asp/tmeda/NO	1776	1772
Fe/tyr/NO	1793	1801

2.2 Synthesis of crystalline iron(II) complexes with aminecarboxylates

Crystalline iron(II) complexes were obtained with ethylenediamine-*N*,*N*′-diacetate (edda), *N*,*N*′-bis(2-hydroxyethyl)ethylenediamine-*N*,*N*′-diacetate (bhedda) and *N*-(2-hydroxyethyl)ethylenediamine-*N,N′,N*′-triacetate (hedtra) as co-ligands. The Fe^{II} complexes with edda and bhedda as chelating ligands were synthesized in order to permit structural-data comparison with the corresponding non-polymeric nitrosyl species **1b** and **3** and, moreover, to draw conclusions about how they are influenced in NO-binding. The crystallization of an Fe/hedtra species was aspired to, as the Fe/hedtra/NO complex exhibits the most stable Fe–NO linkage according to van Eldik's survey.[87,89] But the crystallization of an Fe/hedtra/NO species was unsuccessful.

2.2.1 $[Fe^{II}(edda)(H_2O)_2]$ (**5**)

Colorless needle-shaped crystals of (*OC*-6-13)-diaquaethylenediamine-*N,N*′-diacetatoiron(II) (**5b**) were obtained from an aqueous solution of iron(II) sulfate heptahydrate and equimolar amounts of fully neutralized H_2edda by the diffusion of acetone over one week. The complex crystallized in the monoclinic space group $P2_1/n$ with four formula units in the primitive cell. The asymmetric unit contains one complex molecule with an iron central atom that is octahedrally coordinated by the tetradentate edda co-ligand and two aqua ligands, which coordinate in *trans* position to the nitrogen donor atoms of the chelating ligand. The molecular structure resembles the nitrosyl complex **1b**, whereby the aqua ligand O92 occupies the NO position.

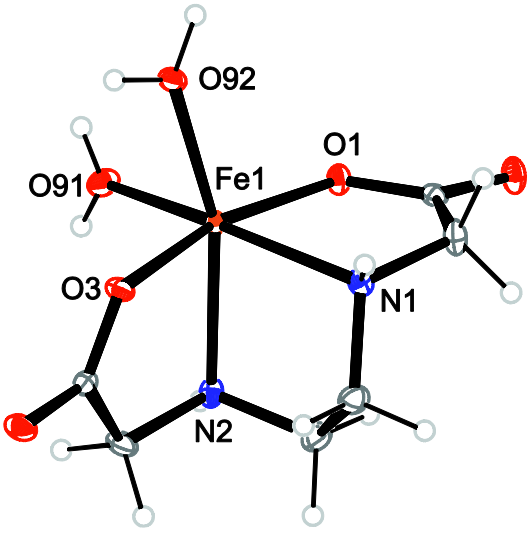

Figure 2.10: ORTEP plot of $[Fe^{II}(edda)(H_2O)_2]$ in crystals of **5b** (50% probability level). Space group $P2_1/n$. Interatomic distances (Å) and angles (°), the standard deviation of the last digit is given in parentheses: Fe1−N1 2.2813(14), Fe1−O3 2.0765(12), Fe1−O1 2.0891(12), Fe1−O91 2.0905(13), Fe1−O92 2.1399(13), Fe1−N2 2.2265(14), Fe1−N1 2.2813(14), O3−Fe1−O1 165.88(5), O3−Fe1−O91 102.42(5), O1−Fe1−O91 90.27(5), O3−Fe1−O92 81.48(5), O1−Fe1−O92 105.32(5), O91−Fe1−O92 88.38(5), O3−Fe1−N2 78.71(5), O1−Fe1−N2 95.10(5), O91−Fe1−N2 91.02(5), O92−Fe1−N2 159.57(5), O3−Fe1−N1 88.61(5), O1−Fe1−N1 77.83(5), O91−Fe1−N1 164.86(5), O92−Fe1−N1 103.67(5), N2−Fe1−N1 80.88(5).

A strong hydrogen-bond pattern prevails in the crystal structure of **5b**. The amine groups and both aqua ligands form hydrogen bonds to carboxylate groups of adjacent coordination entities and a three-dimensional network occurs (Table 2.9 and Figure 2.11). Three ring motifs are formed with the descriptors $R_3^2(10)$ (binary graph-set O92^{v}−H921^{v}···O4^{vii}···H922^{iv}−O92^{iv}−Fe1^{iv}−O3^{iv}−C4^{iv}−O4^{iv}··· H922^{v}), $R_2^2(8)$ (binary graph-set H72···O1^{i}−C1^{i}−O2^{i}···H912−O91−Fe1−N2) and $R_4^2(8)$ (binary graph-set H912···O2^{i}··· H911^{v}−O91^{v}−H912^{v}···O2^{ii}···H911−O91) according to graph-set analysis.[2,3]

Table 2.9: Hydrogen bonds in crystals of **5b** with H···A < r(A) + 2 Å and ∢(DHA) > 110°.

D−H···A	d(D−H)	d(H···A)	d(D···A)	∢(DHA)
N2−H72···O1^{i}	0.88(2)	2.16(2)	3.0215(18)	165.4(19)
O91−H911···O2^{ii}	0.78(2)	2.01(2)	2.7748(18)	164(2)
O91−H912···O2^{i}	0.85(3)	1.84(3)	2.6819(18)	173(2)
O92−H921···O4^{iii}	0.86(3)	1.84(3)	2.7015(17)	178(2)
O92−H922···O6^{iv}	0.80(3)	2.04(3)	2.8440(18)	175(2)

Symmetry code: ^{i} −*x*+3/2, *y*−1/2, −*z*+1/2; ^{ii} *x*−1/2, −*y*+3/2, *z*−1/2; ^{iii} *x*, *y*+1, *z*; ^{iv} −*x*+1/2, *y*+1/2, −*z*+1/2; ^{v} −*x*+1, −*y*+1, −*z*; ^{vi} −*x*+1, −*y*, −*z*; ^{vii} *x*+1/2, −*y*−1/2, *z*−1/2.

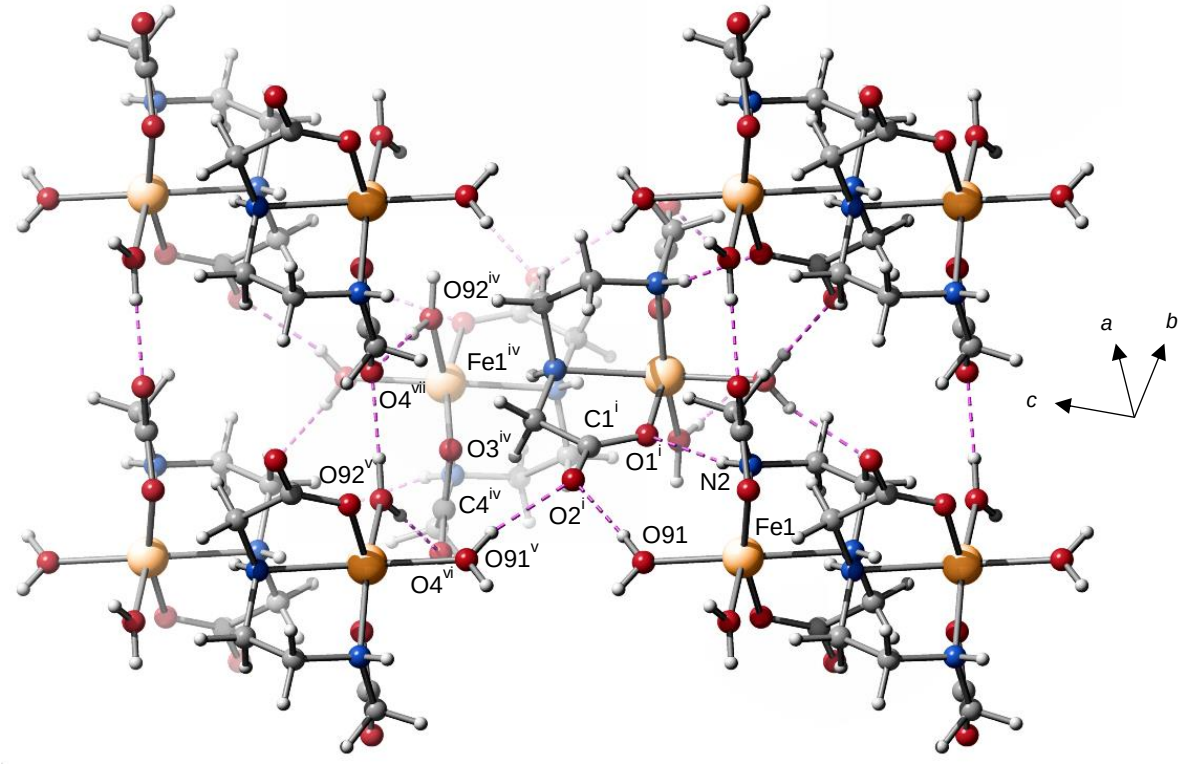

Figure 2.11: SCHAKAL plot of the hydrogen-bond pattern (dashed pink lines) in crystals of **5b**.

2.2.2 [Fe^{II}(bhedda)] (**6**)

Colorless needle-shaped crystals of (*OC*-6-13)-*N,N'*-bis(2-hydroxyethyl)ethylenediamine-*N,N'*-diacetatoiron(II) hydrate (**6** · H_2O) were isolated from an aqueous solution of the raw product **6** by the diffusion of acetone over two weeks (see chapter 2.1.4 for the synthetic route). **6** · H_2O crystallized in the monoclinic space group $P2_1$ with two formula units in the primitive cell. The asymmetric unit contains one iron atom that is coordinated by the bhedda co-ligand in a pentadentate binding mode via the two carboxylate-oxygen atoms, the two nitrogen donor atoms and via the oxygen atom of one hydroxyethyl group. The other hydroxyethyl function bends away from the iron center and forms a hydrogen bond to a carboxyl-oxygen atom of a neighboring complex entity. The remaining coordination site is occupied by a carboxyl-oxygen atom from an adjacent complex unit and a polymeric three-dimensional network results. The molecular structure in crystals of **6** · H_2O is shown in Figure 2.12. The structure is strengthened by a strong hydrogen-bond network. The coordinated hydroxyethyl function forms hydrogen bonds to the water of crystallization. This in turn forms further hydrogen bonds to carboxyl-oxygen atoms and to the dangling hydroxyethyl functions from neighboring complex entities (Table 2.10 and Figure 2.13). Three cyclic motifs are formed with the descriptors $R_5^5(20)$ (quaternary graph-set H911^{vi}···O6^{v}–H86^{v}···O4···H912^{iv}–O91^{iv}–H911^{iv}···O6–H86···O4^{i}–C8^{i}–O3^{i}–Fe1^{i}–O1^{i}–C2^{i}–O2^{i}–Fe1^{vi}–O5^{vi}–H85^{vi}···O91^{vi}), $R_6^5(28)$ (quaternary graph-set H911^{vi}···O6^{v}–H86^{v}···O4–C8–O3–Fe1–O2^{iv}–C2^{iv}–O1^{iv}–Fe1^{iv}–O5^{iv}–H85^{iv}···O91^{iv}–H912^{iv}···O6–H86···O4^{i}–C8^{i}–O3^{i}–Fe1^{i}–O1^{i}–C2^{i}–O2^{i}–Fe1^{vi}–O5^{vi}–H85^{vi}···O91^{vi}), and $R_2^2(12)$ (binary graph-set H912···O4^{iii}–C8^{iii}–O3^{iii}–Fe1^{iii}–O2–C2–O1–Fe1–O5–H85–O91) according to graph-set analysis.[2,3]

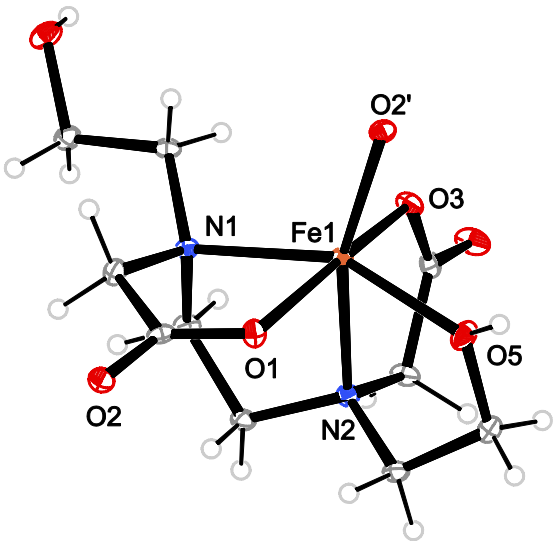

Figure 2.12: ORTEP plot of [Fe^{II}(bhedda)] in crystals of **6** · H_2O (50% probability level). A carboxylate residue from an adjacent complex is included. Space group $P2_1$. Interatomic distances (Å) and angles (°) with the standard deviation of the last digit in parentheses: Fe1–N1 2.284(3), Fe1–N2 2.234(4), Fe1–O1 2.097(3), Fe1–O2 2.081(3), Fe1–O3 2.096(3), Fe1–O5 2.124(3), N1–Fe1–O1 77.59(12), N1–Fe1–O2 113.99(13), N1–Fe1–O3 92.29(12), O2–Fe1–N2 162.58(13), O1–Fe1–O3 165.49(12), N1–Fe1–O5 153.35(15), N1–Fe1–N2 81.37(14), O2–Fe1–O3 92.05(13), O2–Fe1–O5 89.53(12), O2–Fe1–O1 101.48(11).

Table 2.10: Hydrogen bonds in crystals of **6** · H_2O with H···A < r(A) + 2 Å and ∢(DHA) > 110°.

D−H···A	d(D−H)	d(H···A)	d(D···A)	∢(DHA)
O6−H86···O4^{i}	0.84	1.89	2.728(4)	176.2
O5−H85···O91	0.824(14)	1.89(3)	2.665(4)	156(6)
O91−H911···O6^{ii}	0.805(14)	2.05(2)	2.816(4)	158(5)
O91−H912···O4^{iii}	0.818(14)	1.947(19)	2.751(4)	167(6)

Symmetry code: ^{i} −*x*+2, *y*−1/2, −*z*+2; ^{ii} −*x*+1, *y*+1/2, −*z*+1; ^{iii} −*x*+2, *y*+1/2, −*z*+1; ^{iv} –*x*+2, *y*−1/2, −*z*+1; ^{v} –*x*+2, *y*+1/2, −*z*+2; ^{vi} *x*+1, *y*, *z*+1.

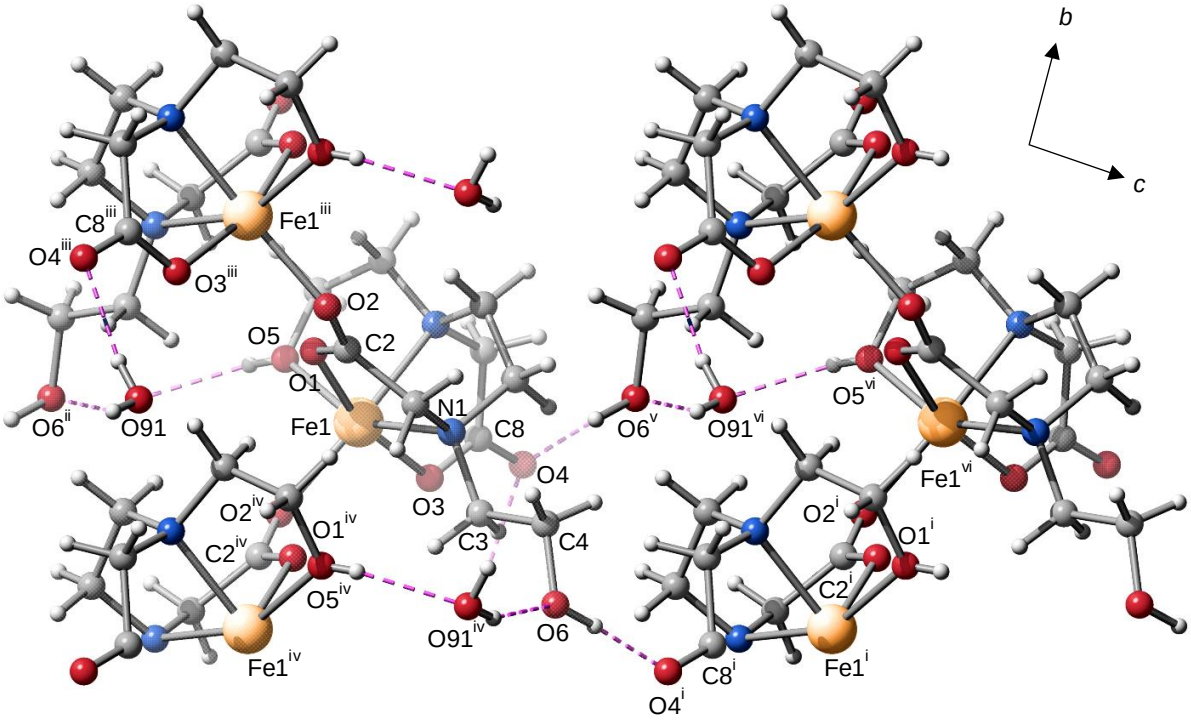

Figure 2.13: SCHAKAL plot of the hydrogen-bond network (dashed pink lines) in crystals of **6** · H_2O with view along [100].

2.2.3 [Fe^{II}(Hhedtra)] (**7**)

[Fe^{II}(Hhedtra)] (**7**) was synthesized from an aqueous solution of iron(II) sulfate heptahydrate and equimolar amounts of half-neutralized *N*-(2-hydroxyethyl)ethylenediamine-*N,N′,N′*-triacetic acid (H_3hedtra). Colorless rod-shaped crystals of (*OC*-6-31*)-N*-(2-hydroxyethyl)ethylenediamine-*N,N′,N′*-triacetatoiron(II) hydrate (**7** · H_2O) were obtained in a "slow-cooling" procedure. An aqueous solution of the raw product **7** was heated under reflux and the reaction flask was transferred immediately to a dewar vessel filled with boiling water. The apparatus was then allowed to cool to room temperature within 24 hours. **7** · H_2O crystallized in the orthorhombic space group *Fdd*2 with 16 formula units in the primitive cell. The molecular structure resembles that of compound **6**. The iron atom is coordinated by the chelating ligand in a pentadentate binding mode via the two nitrogen donor atoms, two carboxylate-oxygen atoms and the oxygen atom of the hydroxyethyl group, resulting in four five-membered chelate rings. The sixth coordination site is occupied by a carboxyl-oxygen atom of an adjacent complex unit. The third carboxylate group is protonated, dangles and forms a hydrogen bond to the water of crystallization. The molecular structure in crystals of **7** · H_2O is shown in Figure 2.14. As in the case of the complex polymer $[Fe(H_2O)_2(\mathbf{4})_2]_{n/n}$, slightly acidic conditions must be satisfied in order to support the dangling protonated carboxymethyl function (pH = 5 of the mother liquor).

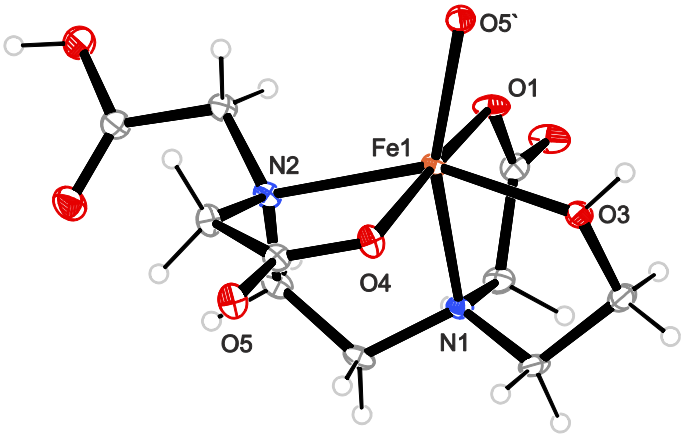

Figure 2.14: ORTEP plot of [Fe^{II}(Hhedtra)] in crystals of **7** · H_2O (50% probability level). A carboxylate residue from an adjacent complex is included. Space group *Fdd*2. Interatomic distances (Å) and angles (°) with the standard deviation of the last digit in parentheses: N2−Fe1 2.341(3), Fe1−O4 2.048(2), Fe1−O5 2.073(3), Fe1−O1 2.075(3), Fe1−O3 2.163(2), Fe1−N1 2.220(3), O5−Fe1 2.073(3), O4−Fe1−O5 104.55(10), O4−Fe1−O1 171.32(10), O5−Fe1−O1 83.96(10), O4−Fe1−O3 85.57(10), O5−Fe1−O3 90.05(10), O1−Fe1−O3 96.31(10), O4−Fe1−N1 93.06(10), O5−Fe1−N1 158.49(10), O1−Fe1−N1 79.03(10), O3−Fe1−N1 78.92(10), O4−Fe1−N2 77.14(10), O5−Fe1−N2 114.82(10), O1−Fe1−N2 97.86(10), O3−Fe1−N2 152.46(11), N1−Fe1−N2 80.76(10).

The crystal structure is stabilized via a strong hydrogen-bond network. The coordinated hydroxyethyl group and the water of crystallization form hydrogen bonds to a carboxylate group of a neighboring complex unit. Two ring motifs are formed with the descriptors $R_3^3(17)$ (tertiary graph-set O91^{v}···H87^{iv}–O7^{iv}–C10^{iv}–C9^{iv}–N2^{iv}–Fe1^{iv}–O5^{iii}–C5^{iii}–O4^{iii}–Fe1^{iii}–O3^{iii}–H83^{iii}···O2^{vi}–C1^{vi}–O1^{vi}···H912^{v}) and $R_3^2(8)$ (tertiary graph-set O91^{iii}–H912^{iii}···O1–Fe1–O3–H83···O2^{iii}···H911^{iii}) according to graph-set analysis.[2,3]

Table 2.11: Hydrogen bonds in crystals of **7** · H_2O with H···A < r(A) + 2 Å and ∢(DHA) > 110°.

D–H···A	d(D–H)	d(H···A)	d(D···A)	∢(DHA)
O91–H911···O2	0.91(8)	1.98(8)	2.841(4)	157(6)
O91–H912···O1^{ii}	0.73(7)	2.20(7)	2.927(4)	170(7)
O7–H87···O91^{i}	0.91(6)	1.75(6)	2.640(4)	166(6)
O3–H83···O2^{iii}	0.84	1.78	2.624(3)	177.5

Symmetry code: ^{i} −*x*+1, −*y*+1, *z*; ^{ii} *x*+1/4, −*y*+3/4, *z*−1/4; ^{iii}−*x*+3/4, *y*−1/4, *z*+1/4, ^{iv} *x*−1/4, −*y*+1/4, *z*+3/4; ^{v} −*x*+3/4, *y*−3/4, *z*+3/4; ^{vi} *x*, *y*−1/2, *z*+1/2.

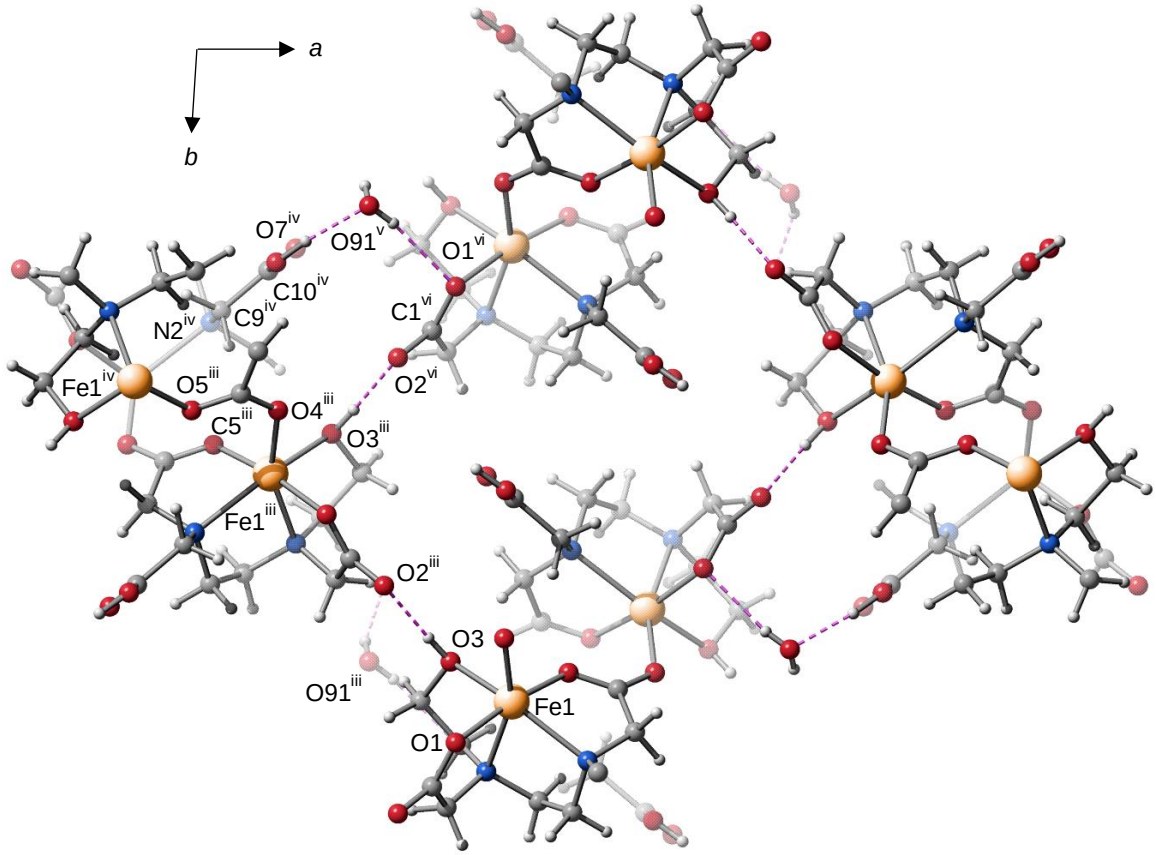

Figure 2.15: SCHAKAL drawing of the hydrogen-bond network (dashed pink lines) in crystals of **7** · H_2O with view along [001].

2.3 Quantum-chemical calculations

Quantum-chemical calculations, based on DFT, were performed in order to attain a clear insight into the electronic structure of the $\{FeNO\}^7$(S = 3/2) complexes and to evaluate possible differences between stable and less stable[4,115] complexes. Structural peculiarities are discussed with DFT calculations and quantified with relaxed surface scans. The calculations were performed using spin-unrestricted open-shell systems with a quartet spin state.

2.3.1 Structural optimization

Geometry optimizations were expected to reproduce the experimentally determined structural parameters of the Fe–N–O moiety as well as the N–O stretching vibrations as accurately as possible. All optimizations were accomplished with starting geometries derived from X-ray crystallography. The triple zeta basis set def2-TZVP[122] with polarized and diffuse functions led to a satisfying overall agreement of computational and experimental results for the less stable compounds.[4] Thus, the complexes were optimized on the def2-TZVP level of theory with the pure density functional BP86[123,124], the dispersion-corrected pure density functional B97-D[125] as well as with the hybrid density functional TPSSh[126]. Dispersion correction (D3) by Grimme[125] was utilized to consider *van-der-Waals* interactions and the COSMO model[127] was applied for solvent correction. As the normal COSMO model[127] was not sufficient to account for the strong hydrogen-bond network in the less stable compounds, geometry optimizations were also accomplished using the COSMO-RS model.[4] This solvation model is able to provide a more suitable description of hydrogen bonds without the need to know the explicit position of all molecules in space.[128,129] The carboxylate residue of the adjacent anion in **2** was first replaced by an acetato co-ligand in order to construct a non-polymeric single unit. But the optimization of this single unit calculates the Fe–N–O bond angle as too small. A suitable picture of the Fe–N–O entity is obtained when the sixth coordination site is occupied by an aqua ligand. This calculated $[Fe(H_2O)(NO)(nta)]^-$ complex anion is specified as **2i** in the following text.

A comparison of results on complexes **1b−4** with different computational methods is given in Tables 2.12–2.15. Regarding bond distances only, a satisfying overall agreement of computational and experimental results is obtained with the TPSSh functional or the B97-D functional. As expected, the Fe–O91 distance in **1b** is described more precisely using the COSMO-RS model for solvent correction. However, when the Fe–N–O bond angles and the N–O stretching vibrations are considered as well, an accurate description of the Fe–N–O moiety is obtained with the TPSSh/COSMO combination or with the B97-D/COSMO-RS combination. TPSSh/COSMO-RS calculates the Fe–N–O bond angles about 12° too big and the N–O stretching vibration energies approximately 50 cm^{-1} too high. On the whole, the TPSSh/COSMO combination provides reasonable values for the structural parameters as well as for the N–O stretching frequencies. The maximal deviation between the computed and the experimental N–O stretching vibration energy is 17 cm^{-1} (**2i**), which matches the normal limits found for DFT calculations.[130] Since a COSMO-RS calculation may take about three times more computing time than a normal COSMO calculation does, subsequent calculations were performed on the TPSSh/def2-TZVP level of theory with the COSMO model for solvent correction.

Table 2.12: DFT results on **1b** using the basis set def2-TZVP, the functionals BP86, B97-D or TPSSh, COSMO (c) or COSMO-RS (crs) and dispersion correction (D3). The Exp. column lists the average structural data of the two independent complex molecules in the asymmetric unit in crystals of **1b** · ½ H_2O.

1b	Exp.	BP86 c	BP86 crs	B97-D c	B97-D crs	TPSSh c	TPSSh crs
N1–O1/Å	1.16	1.18	1.18	1.17	1.17	1.17	1.16
Fe1–N1/Å	1.77	1.73	1.73	1.78	1.78	1.78	1.78
Fe1–N2/Å	2.23	2.19	2.19	2.24	2.23	2.23	2.23
Fe1–N3/Å	2.17	2.18	2.16	2.20	2.19	2.18	2.18
Fe1–O2/Å	2.01	1.98	2.04	2.02	2.08	2.01	2.06
Fe1–O3/Å	2.09	2.07	2.12	2.07	2.12	2.05	2.09
Fe1–O91/Å	2.06	2.23	2.16	2.23	2.17	2.19	2.13
Fe1–N1–O1/°	148.1	143.5	145.5	146.1	149.5	152.4	160.0
$\tilde{\nu}$(NO)/cm^{-1}	1761	1683	1702	1729	1752	1786	1815

Table 2.13: DFT results on **2i** using the basis set def2-TZVP, the functionals BP86, B97-D or TPSSh, COSMO (c) or COSMO-RS (crs) and dispersion correction (D3).

2(**i**)	Exp.	BP86 c	BP86 crs	B97-D c	B97-D crs	TPSSh c	TPSSh crs
N1–O1/Å	1.15	1.18	1.17	1.17	1.16	1.17	1.16
Fe1–N1/Å	1.75	1.72	1.73	1.77	1.77	1.77	1.77
Fe1–N2/Å	2.23	2.21	2.21	2.25	2.25	2.24	2.24
Fe1–O2/Å	2.07	2.05	2.08	2.06	2.09	2.04	2.07
Fe1–O3/Å	2.05	2.00	2.04	2.03	2.08	2.02	2.06
Fe1–O4/Å	2.09	2.05	2.08	2.06	2.09	2.04	2.06
Fe1–N1–O1/°	164.8	147.3	149.5	151.9	155.9	161.4	175.1
$\tilde{\nu}$(NO)/cm^{-1}	1791	1700	1738	1746	1787	1808	1852

Table 2.14: DFT results on **3** using the basis set def2-TZVP, the functionals BP86, B97-D or TPSSh, COSMO (c) or COSMO-RS (crs) and dispersion correction (D3). The N–O stretching vibration of the aqueous complex is given in the Exp. column because of the low crystal yield.

3	Exp.	BP86 c	BP86 crs	B97-D c	B97-D crs	TPSSh c	TPSSh crs
N1–O1/Å	1.13	1.18	1.18	1.17	1.17	1.17	1.16
Fe1–N1/Å	1.78	1.73	1.73	1.78	1.78	1.78	1.77
Fe1–N2/Å	2.21	2.20	2.19	2.25	2.24	2.23	2.23
Fe1–N3/Å	2.24	2.25	2.23	2.27	2.25	2.23	2.22
Fe1–O2/Å	2.03	1.98	2.01	2.01	2.05	2.01	2.05
Fe1–O3/Å	2.04	2.05	2.10	2.06	2.10	2.03	2.08
Fe1–O4/Å	2.08	2.19	2.16	2.19	2.16	2.14	2.13
Fe1–N1–O1/°	150.2	143.2	145.2	146.1	149.3	152.4	161.7
$\tilde{\nu}$(NO)/cm^{-1}	1782	1684	1706	1733	1758	1791	1828

Table 2.15: DFT results on **4** using the basis set def2-TZVP, the functionals BP86, B97-D or TPSSh, COSMO (c) or COSMO-RS (crs) and dispersion correction (D3).

4	Exp.	BP86 c	BP86 crs	B97-D c	B97-D crs	TPSSh c	TPSSh crs
N1–O1/Å	1.16	1.18	1.18	1.18	1.17	1.17	1.16
Fe1–N1/Å	1.76	1.73	1.73	1.78	1.78	1.78	1.77
Fe1–N2/Å	2.20	2.20	2.20	2.24	2.24	2.23	2.23
Fe1–N3/Å	2.24	2.34	2.29	2.36	2.31	2.30	2.27
Fe1–O2/Å	2.05	2.05	2.09	2.06	2.10	2.04	2.07
Fe1–O3/Å	2.07	2.06	2.09	2.06	2.10	2.04	2.08
Fe1–O4/Å	2.00	2.01	2.02	2.04	2.06	2.03	2.06
Fe1–N1–O1/°	148.8	143.3	146.2	146.5	151.2	153.5	169.1
$\tilde{\nu}$(NO)/cm^{-1}	1781	1695	1708	1715	1760	1774	1835

2.3.2 Electronic-structure description

The electronic structure of the nitrosyl compounds is analyzed in terms of the relevant canonical molecular orbitals. The molecular orbital diagram of the HOMO-LUMO region in **1b** is illustrated in Figure 2.16. It is representative for complexes **2i−4**. In the following orbital discussion, the z-axis is defined along the Fe−N vector of the Fe–N–O group (see also the MO diagram of free NO in chapter 1.2 on page 5).

The five energetically highest occupied orbitals in the α-spin manifold (69−73) exhibit a marginal Fe d character with weak antibonding contributions from the co-ligands. The two highest occupied orbitals in the β-spin manifold (69/70) are comprised of π interactions between the NO 1π* orbitals and the Fe d_{xz} and d_{yz} orbitals, respectively. In addition to a σ bond between the Fe d_{z^2} orbital and the 2σ orbital of the NO ligand, these two π-bonding interactions contribute most to the Fe–NO bonding. The bonding σ interaction is, however, greatly stabilized and difficult to identify due to strong contributions from the co-ligands in the lower energy levels of the complex. The α-HOMO (73) is comprised of the antibonding σ interaction between the Fe d_{z^2} and the NO 2σ orbital. To reduce this unfavorable interaction, the Fe–N–O bond angle deviates from 180° (152° in the calculated structure of **1b**). In doing so, a weak σ interaction between the Fe d_{yz} orbital and one NO 1π* orbital is generated, which becomes more essential the more acute the Fe–N–O angle becomes (see also chapter 2.3.6.1). This interaction is enhanced by mixing minimal Fe d_{z^2} contributions to the β-orbital with a Fe d_{yz} character (70).

It is customary in literature to consider the unoccupied molecular orbitals in order to describe the Fe–N–O bonding because the occupied molecular orbitals are often greatly stabilized due to spin polarization and high contributions from the co-ligands.[4,58,62,66,67,131] The unoccupied molecular orbitals reflect the bonding properties as described above. The five lowest unoccupied orbitals in the β-spin manifold (71−75) are comprised of a mostly Fe d character, whereas the two unoccupied orbitals in the α-spin manifold (74/75) show a predominantly NO 1π* character. Within the unoccupied molecular orbitals in the β-spin manifold, strong NO contributions are found in LUMO+1 and LUMO+2 (72/73) that are made up of antibonding π interactions between the NO 1π* orbitals and the Fe d_{xz} and d_{yz} orbitals, respectively. When the bonding situation is initially considered as $^{6}Fe^{3+}–^{3}NO^{-}$,[58–65,67] the nitrosyl ligand acts as a strong π donor in the β-spin manifold while almost no π backdonation from the singly occupied Fe d_{xz} and d_{yz} orbitals into the empty NO 1π* orbitals prevails within the α-spin manifold (weak π acceptor). The nearly evenly distributed percentages of Fe and NO in the two highest occupied ß-orbitals (69/70) indicate an almost covalent bonding character for the Fe–N–O moiety with antiferromagnetic spin coupling between the NO 1π* and the Fe d_{xz} and d_{yz} orbitals. The three unpaired electrons, responsible for the *S* = 3/2 spin state, are located almost completely on the iron atom.

A density-of-states (DOS) plot for the α-spin as well as for the β-spin manifold is shown in Figure 2.17. The diagrams visualize contributions from the NO fragment as well as from the residual [Fe^{II}L] fragment (L = co-ligands) to the total DOS in complex **1b**. The DOS plots were created using the AOMix software.[132,133] They reflect the electronic structure of **1b** as described above.

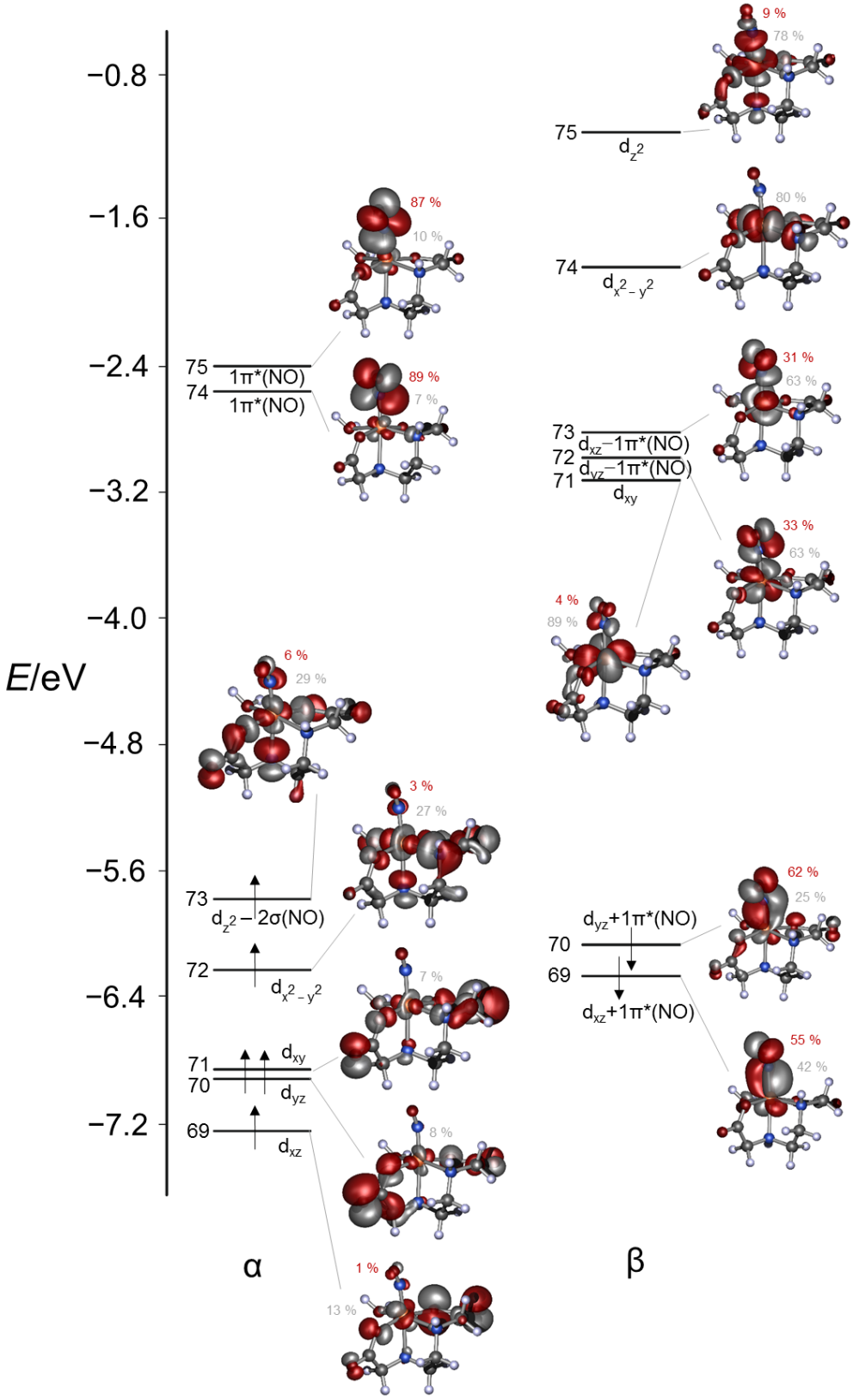

Figure 2.16: Energy-level diagram of the HOMO-LUMO region for the spin-unrestricted calculation of TPSSh/def2-TZVP-optimized **1b** together with the orbital contours and their Fe and NO contributions. The individual contributions were derived from Mulliken population analysis (contributions from Fe in gray, contributions from NO in red). Up-arrows symbolize α-spin electrons, down-arrows β-spin electrons. Isovalue of the orbitals: 0.04.

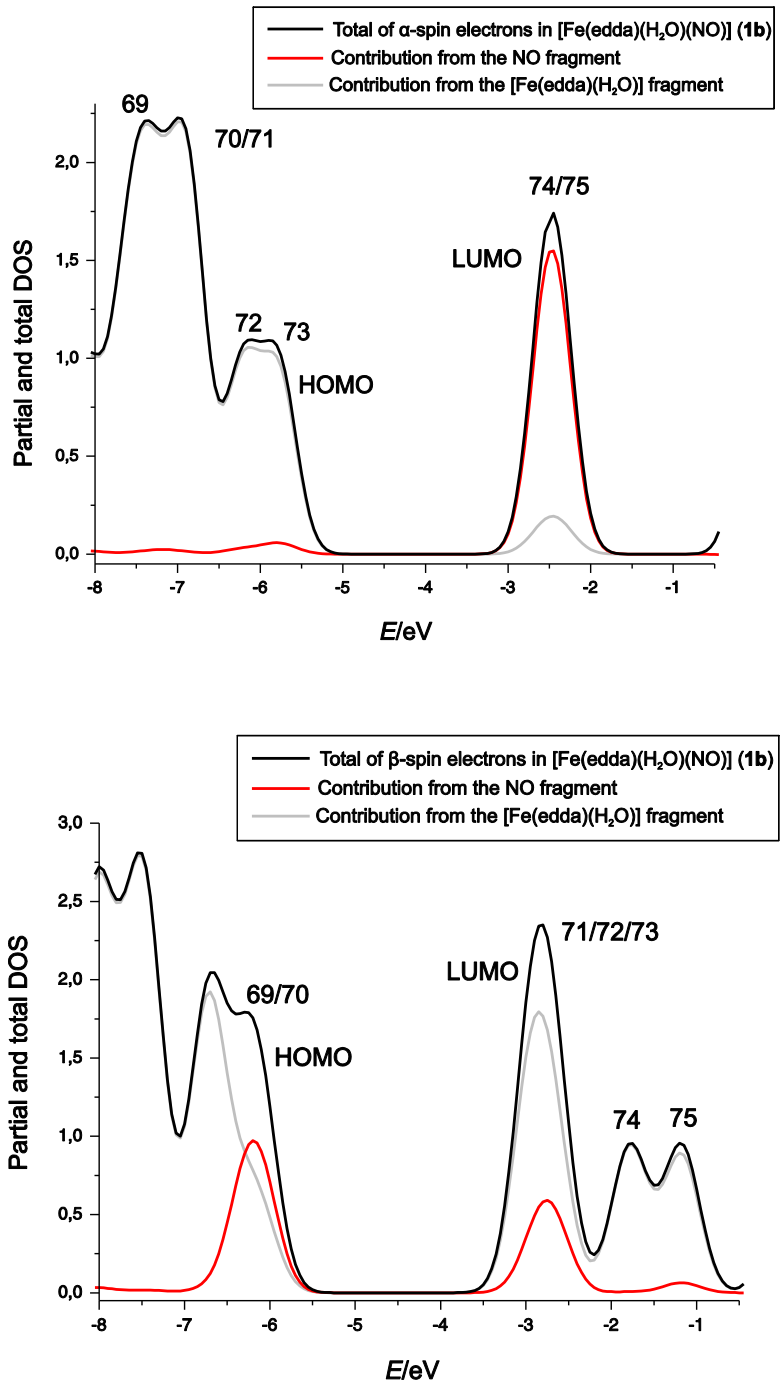

Figure 2.17: Continuous Gaussian-band shape plot of the density of states (DOS) in **1b**. The contributions of the NO fragment and the [Fe^{II}L] fragment (L = co-ligands) to the total DOS are presented for the α-spin manifold (top) and for the β-spin manifold (bottom). The DOS plots were created using the AOMix program.[132,133]

2.3.3 Population analyses

Mulliken population analysis (MPA)[134], natural population analysis (NPA)[135] and quantum theory of atoms in molecules (QTAIM)[136,137] were carried out to gain insight into the charge and spin distribution of the Fe–N–O moiety. To assign charges to atoms, the spatial region of those atoms must be well defined. MPA and NPA are based on the linear combination of atomic orbitals and thus the wave function of the molecule. Shared electrons are equally distributed between two atoms. NPA differs between orbitals involved in bonding and antibonding, non-bonding atomic orbitals and Rydberg type orbitals. In contrast to MPA, which considers all orbitals, NPA treats only the orbitals involved in bonding. QTAIM was found to provide an accurate interpretation of the chemical bonding in metal complexes.[136] The method defines the spatial partition of atoms with electron density surfaces. The calculation is therefore based on the electron density and a different partitioning of atoms is realized.

The calculations were performed using the def2-TZVP basis set and the hybrid density functional TPSSh (T) or the pure density functional BP86 (B). Table 2.17 summarizes the computed charges and spin densities on the iron center and on the nitrosyl ligand in complexes **1b−4**. All population analyses assign positive charges to the iron center and the nitrogen atom and negative charges to the oxygen atom. In general, MPA calculates lower charges than NPA, which in turn gives lower charges than QTAIM. The population analyses reveal spin densities with opposite signs on the iron center and on the nitrosyl group. The chelating ligands hardly affect the results. Slightly lower charges are calculated on the nitrosyl ligand of the monoanionic complex **4**. The computed charges on the nitrosyl ligand show only slight dependence on the functional but vary considerably within the population method. MPA assigns almost neutral charges to the nitrosyl group (0.01 to −0.07). More negative charges are calculated with NPA (−0.12 to −0.19) and QTAIM (−0.31 to −0.35). The charges on the iron atom follow the same trend. The lowest positive charges on the iron center are calculated with MPA (+0.33 to +0.51). NPA (+1.19 to +1.40) and QTAIM (+1.42 to +1.61) assign more positive charges to the central metal. The computed spin densities depend strongly on the functional. The TPSSh functional assigns β-spin densities of −1.03 to −1.14 to the nitrosyl ligand and α-spins between +3.61 and +3.77 to the iron center. The BP86 functional calculates less spin-polarized solutions with smaller spin densities on the iron atom (+2.83 to +3.41) and on the nitrosyl ligand (−0.41 to −0.81). Figure 2.18 illustrates a spin-density plot of $[Fe(Hedta)(NO)]^-$ (**4**). It is representative for compounds **1b−3**. The donor atoms of the co-ligand show the same positive spin density as the iron center due to spin delocalization.

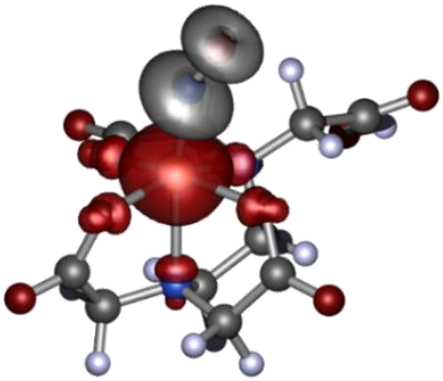

Figure 2.18: Plot of the spin density in **4**. Calculated with TPSSh, def2-TZVP, COSMO and dispersion correction (D3).

In order to examine possible differences in the charge distribution of the stable and less stable compounds, the QTAIM charges of some less stable quartet-{FeNO}^{7} complexes were calculated as well. The charges on the nitrosyl group and on the iron center are summarized in Table 2.16. Similar results are obtained for $[Fe(H_2O)_2(NO)(oda)]$ (**I**), $[Fe(dipic)(H_2O)_2(NO)]$ (**II**) and $[Fe(H_2O)_2(ida)(NO)]$ (**III**). The lowest negative charge on the nitrosyl group is calculated in the unstable complex cation $[Fe(H_2O)_5(NO)]^{2+}$.

Table 2.16: QTAIM charges *q* of different {FeNO}^{7}(*S* = 3/2) complexes arranged according to the stability constants K_{NO} derived by the van Eldik's group.[87] All values are elementary charges. The calculations were performed with TPSSh/def2-TZVP, dispersion correction (D3) and COSMO(water).

	q(Fe)	*q*(NO)
$[Fe(H_2O)_5(NO)]^{2+}$	1.63	−0.11
I[a]	1.62	−0.25
II[a]	1.61	−0.25
III[a]	1.59	−0.27

(**I**) $[Fe(H_2O)_2(NO)(oda)]$, (**II**) $[Fe(dipic)(H_2O)_2(NO)]$, (**III**) $[Fe(H_2O)_2(ida)(NO)]$.

[a] The starting geometries for the calculations were taken from the X-ray results of Reference [4].

Table 2.17: MPA, NPA and QTAIM analysis on **1b**, **2i**, **3** and **4**. All values are elementary charges. The calculations were carried out with the basis set def2-TZVP and the functional TPSSh (T) or BP86 (B), dispersion correction (D3) and COSMO(water).

			Charge				Spin			
			Fe	N	O	NO	Fe	N	O	NO
1b	MPA	T	0.50	0.16	−0.16	0	3.73	−0.60	−0.48	−1.08
		B	0.40	0.13	−0.14	0.01	3.33	−0.39	−0.32	−0.71
	NPA	T	1.38	0.04	−0.19	−0.15	3.64	−0.61	−0.43	−1.04
		B	1.19	0.08	−0.21	−0.13	2.87	−0.17	−0.24	−0.41
	QTAIM	T	1.57	0.09	−0.40	−0.31	3.61	−0.57	−0.46	−1.03
		B	1.43	0.07	−0.39	−0.32	3.02	−0.24	−0.23	−0.47
2i	MPA	T	0.51	0.18	−0.18	0	3.77	−0.64	−0.50	−1.14
		B	0.42	0.15	−0.15	0	3.41	−0.46	−0.36	−0.82
	NPA	T	1.40	0.04	−0.19	−0.15	3.67	−0.66	−0.44	−1.10
		B	1.22	0.08	−0.21	−0.13	2.91	−0.21	−0.27	−0.48
	QTAIM	T	1.61	0.09	−0.41	−0.32	3.64	−0.61	−0.47	−1.08
		B	1.47	0.07	−0.39	−0.32	3.07	−0.28	−0.25	−0.53
3	MPA	T	0.44	0.16	−0.17	−0.01	3.72	−0.59	−0.49	−1.08
		B	0.33	0.13	−0.15	−0.02	3.33	−0.40	−0.33	−0.73
	NPA	T	1.38	0.04	−0.19	−0.15	3.62	−0.60	−0.43	−1.03
		B	1.20	0.08	−0.20	−0.12	2.83	−0.16	−0.25	−0.41
	QTAIM	T	1.56	0.09	−0.40	−0.31	3.61	−0.58	−0.47	−1.05
		B	1.42	0.08	−0.39	−0.31	3.01	−0.24	−0.23	−0.47
4	MPA	T	0.48	0.12	−0.19	−0.07	3.75	−0.64	−0.50	−1.14
		B	0.38	0.09	−0.16	−0.07	3.36	−0.45	−0.35	−0.80
	NPA	T	1.39	0.02	−0.21	−0.19	3.65	−0.65	−0.45	−1.10
		B	1.21	0.07	−0.22	−0.15	2.84	−0.20	−0.27	−0.47
	QTAIM	T	1.58	0.07	−0.42	−0.35	3.63	−0.61	−0.48	−1.09
		B	1.43	0.05	−0.40	−0.35	3.03	−0.28	−0.25	−0.53

2.3.4 AOMix-FO charge decomposition analysis (CDA)

AOMix-fragment orbital charge decomposition analysis (CDA)[132,133] was performed in order to evaluate the amount of electron donation and backdonation between NO and [Fe^{II}L] (L = co-ligands). Table 2.18 summarizes the CDA results for compounds **1b−4** with the two fragments $^{2}NO^{0}$ and $^{5}[Fe^{II}L]$. A positive value indicates charge transfer from the [Fe^{II}L] fragment to the NO fragment and *vice versa*. The analyses show nearly no electron transfer in the neutral complexes **1b** and **3**. A minimal charge transfer occurs from the [Fe^{II}L] fragment to the NO group in the β-spin manifold of the monoanionic compounds **2i** and **4**.

Table 2.18: CDA analyses using AOMix-FO. All values are elementary charges. Calculated with TPSSh/def2-TZVP, dispersion correction (D3) and COSMO(water).

	α–CT (Fe → NO)	β–CT (Fe → NO)
1b	−0.03	0.03
2i	−0.06	0.11
3	−0.03	0.04
4	−0.04	0.13

CDA was further accomplished with the nitrosonium cation ($^{0}NO^{+}$) as well as the nitroxyl anion ($^{3}NO^{-}$) as fragments. The results for compound **1b** are listed in Table 2.19. They are representative for complexes **2i−4**.

Table 2.19: CDA analyses using AOMix-FO. All values are elementary charges. Calculated with TPSSh/def2-TZVP, dispersion correction (D3) and COSMO(water).

	α–CT (Fe → NO)	β–CT (Fe → NO)
$^{4}[Fe^{I}L]-^{1}NO^{+}$	−0.03	1.03
$^{6}[Fe^{III}L]-^{3}NO^{-}$	−0.03	−0.97

Whereas almost no charge transfer arises in the α-spin manifold, a total of one β-electron is transferred from the iron center to the NO group in the case of the $^{1}NO^{+}$ fragment and from the NO group to the iron center in the case of the $^{3}NO^{-}$ fragment.

2.3.5 Broken-symmetry calculations

Spin-coupling parameters of the nitrosyl-iron compounds were determined with broken-symmetry (bs) calculations.[138,139] The Heisenberg exchange coupling constant *J* was calculated in order to quantify the strength of the antiferromagnetic spin coupling and the overlap integrals $S_{\alpha\beta}$ in order to estimate the covalent bonding character. The BS-calculation starts with a ferromagnetic coupled spin state (hs) and generates a broken-symmetry (bs) state by swapping the spins at the center with the smaller number of unpaired electrons. The coupling constant *J* determines the energetical arrangement of the spin states (Formula 2.1) and is calculated from the energy difference between the ferromagnetic coupled (E_{hs}) and the broken-symmetry state (E_{bs}) with Yamaguchi's expression[140] (Formula 2.2).

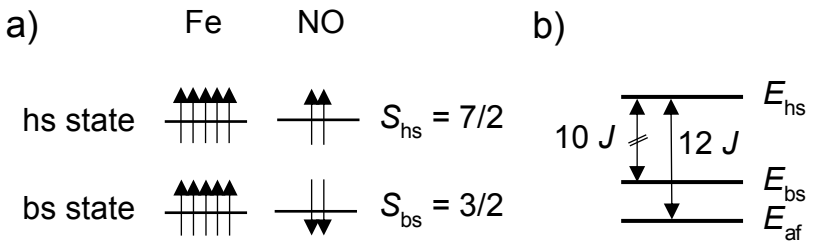

Figure 2.19: (a) Formal "site spin" orientations in the ferromagnetic-coupled (hs) and broken-symmetry (bs) states of the nitrosyl-iron compounds, up-arrows symbolize α-spin electrons, down-arrows β-spin electrons. (b) The Heisenberg exchange coupling constant *J* is calculated from the energy difference between the ferromagnetic-coupled (E_{hs}) and the broken-symmetry (E_{bs}) state and is ideally very close to the real antiferromagnetic (E_{af}) spin state.

$$E(S) = -JS(S+1) \tag{2.1}$$

$$J = -\frac{E_{\mathrm{hs}} - E_{\mathrm{bs}}}{\langle S^2\rangle_{\mathrm{hs}} - \langle S^2\rangle_{\mathrm{bs}}} \tag{2.2}$$

Table 2.20 summarizes the Heisenberg exchange coupling constants *J* as well as the overlap integrals $S_{\alpha\beta}$ of the non-orthogonal singlet coupled orbital pairs HOMO−3 and HOMO−4 (the two β-HOMOs that represent the π-bonding interaction between NO and Fe, see chapter 2.3.2) of the broken-symmetry solution for compounds **1b−4**. The energies of the broken-symmetry calculations differ only little from the real antiferromagnetic spin state solutions. Moreover, the determined broken-symmetry spin states $\langle S^2\rangle_{bs}$ of about 4.56 agree suitably with the real antiferromagnetic spin states $\langle S^2\rangle_{af}$ of 3.75.

Table 2.20: Results of the broken-symmetry calculations: Heisenberg exchange coupling constants *J*, overlap integrals $S_{\alpha\beta}$ of the non-orthogonal singlet coupled orbital pairs HOMO−3 and HOMO−4 as well broken-symmetry spin states $\langle S^2 \rangle_{bs}$ for compounds **1b−4**. The DFT calculations were performed with TPSSh/def2-TZVP, dispersion correction (D3) and COSMO(water).

	1b	**2i**	**3**	**4**
J/cm^{-1}	−1948	−1891	−1943	−1813
$S_{\alpha\beta}$ (HOMO−3)	0.75	0.74	0.75	0.75
$S_{\alpha\beta}$ (HOMO−4)	0.81	0.79	0.81	0.77
$\langle S^2 \rangle_{bs}$	4.54	4.54	4.58	4.60

The computed Heisenberg-exchange coupling constants *J* indicate a strong antiferromagnetic coupling between the iron center and the nitrosyl ligand and the magnitudes of the overlap integrals $S_{\alpha\beta}$ of HOMO−3 and HOMO−4 are consistent with an almost covalent bond in the Fe–N–O moiety.

2.3.6 Structural peculiarities

The molecular structures of the {FeNO}^{7}(S = 3/2) complexes described in this thesis reveal two distinct structural features. The nitrosyl ligand is tilted towards a carboxylate function of the aminecarboxylato co-ligand. Furthermore, the thermal ellipsoid of their nitrosyl-oxygen atom is uncommonly small for {FeNO}^{7}(S = 3/2) complexes.[4,46] This is particularly obvious in complex **3**. These peculiarities will be outlined and analyzed with DFT calculations in the following part.

2.3.6.1 The thermal ellipsoid of the nitrosyl-oxygen atom

Among quartet-{FeNO}^{7} complexes, an exact experimental determination of the Fe–N–O bond angle is often hampered because of the high thermal mobility and the concomitant disordered ellipsoid of their nitrosyl-oxygen atom.[4,46] A relaxed surface scan of the Fe–N–O bond angle in **1b−4** was performed in order to understand the origin of the small broadening of their nitrosyl-oxygen atoms' vibrational ellipsoid. The Fe–N–O bond angles were fixed to constrained values between 120° and 180° in steps of 10° and all other coordinates were optimized to their most favorable values. Because of the normal shape of the thermal ellipsoid, a bending curve with a distinct minimum close to the experimentally determined value was expected. Bending of the Fe–N–O unit should result in significant energy differences between the DFT-optimized structures. The dependence of the energy on the Fe–N–O bond angle is shown in Figure 2.20. A weak bending potential is calculated in which the Fe–N–O angle can be varied between 140° and 180° with an energy change of only 2.5 kJ mol^{-1}. However, the energetic minima agree with the experimentally determined bond angles. The small broadening is obviously not due to electronic effects but it may be the result of crystal-packing effects or intermolecular interactions. In order to evaluate whether the NO ligand is untypically fixed by short intermolecular contacts, the direct

environment of the nitrosyl ligand was analyzed with the program package MERCURY, whereby distances of ±0.1 of the sum of *van-der-Waals* radii of atoms were considered. But neither an intermolecular interaction nor a specific crystal-packing pattern that could have accounted for the small thermal ellipsoid was found (see also the packing diagrams of the crystal structures in the APPENDIX).

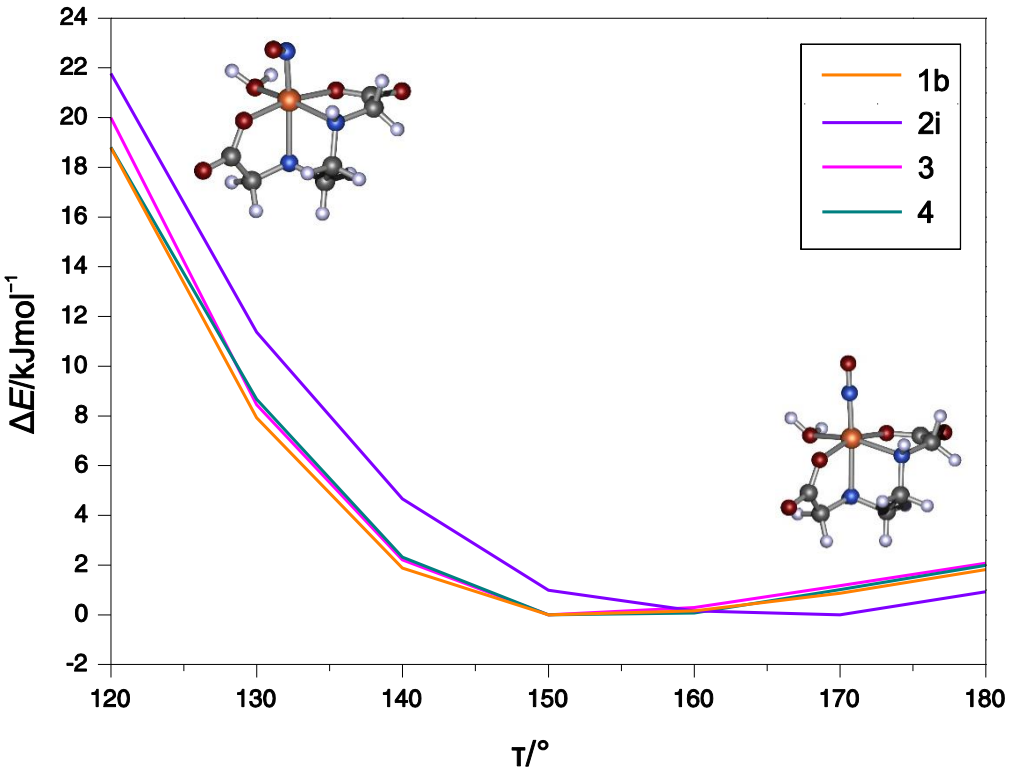

Figure 2.20: Fe–N–O bending potential of **1b**−**4**. The DFT calculations were performed with TPSSh/def2-TZVP, dispersion correction (D3) and COSMO(water). The DFT-optimized structures of **1b** are shown for graphical visualization.

A Walsh diagram analysis (Figure 2.21) demonstrates that the flat Fe–N–O bending potential results from the opposing effects of both Fe–NO π bonds and the Fe–NO σ antibond. This is in line with the results of the less stable complexes.[115] When the Fe–N–O moiety is bent, the character of the α-HOMO changes from a σ-antibonding interaction between the Fe d_{z^2} orbital and the NO 2σ lone pair to a weak σ-bonding interaction between the Fe d_{z^2} orbital and one NO π* orbital. This results in a lowering of the α-HOMO orbital energy of about 0.1 eV. Furthermore, in a bent Fe–N–O moiety, the Fe d_{xz}–NO 1π* interaction is moderately destabilized due to the weakened π-bonding interaction (≈ 0.6 eV, referring to a linear Fe–N−O unit). The Fe d_{yz}–NO 1π* interaction now has σ-bonding character, is faintly destabilized (≈ 0.1 eV, referring to a linear Fe–N–O unit) and becomes the β-HOMO−1. This σ-bonding interaction is enhanced by mixing minimal Fe d_{z^2} contributions to the β-orbital with a predominantly Fe d_{yz} character. In a linear Fe–N–O moiety, both Fe–NO π interactions are greatly stabilized and lowered in energy because of the optimal orbital overlap between the NO 1π* and the Fe d_{xz} and Fe d_{yz}

orbitals, respectively. The balance of these effects causes the minor energy differences that are associated with bending of the Fe–N–O unit.

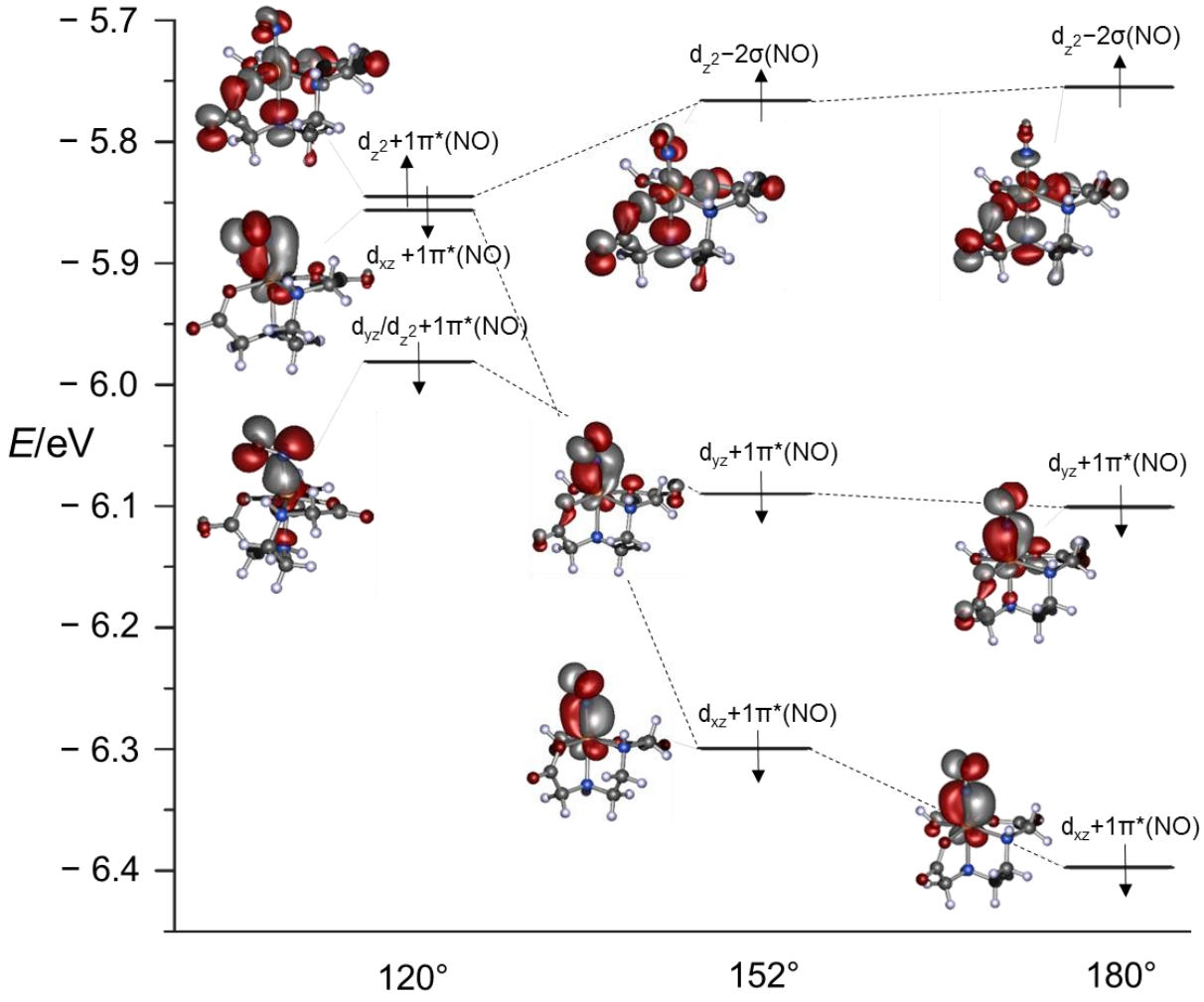

Figure 2.21: Walsh diagram of **1b**. The diagram is representative for compounds **2i–4**. Up-arrows indicate α-spin electrons, down-arrows β-spin electrons. The DFT calculations were performed with TPSSh/def2-TZVP, dispersion correction (D3) and COSMO(water), isovalue of the orbitals: 0.04.

2.3.6.2 The tilt of the NO ligand

The molecular structures of **1b−4** show a particularity that can also be found among the less stable representatives.[4] The nitrosyl group is bent towards the oxygen atom of a coordinating carboxylate group that is perpendicular to the basal plane of the coordination octahedron (the plane normal to the NO ligand). When two such oxygen donor atoms exist *cis* to each other, the NO ligand is tilted into the space between them (**2** and **4**). The observation is supported by DFT calculations. Geometry optimizations of structures with the nitrosyl group pointing to another donor atom in the complex' equatorial plane, result in energetic minimum structures with the nitrosyl ligand tilting towards the respective oxygen donor atom (all coordinates were optimized to their most favorable values). The optimized minimum structures of **1b−4** are illustrated in Figure 2.22.

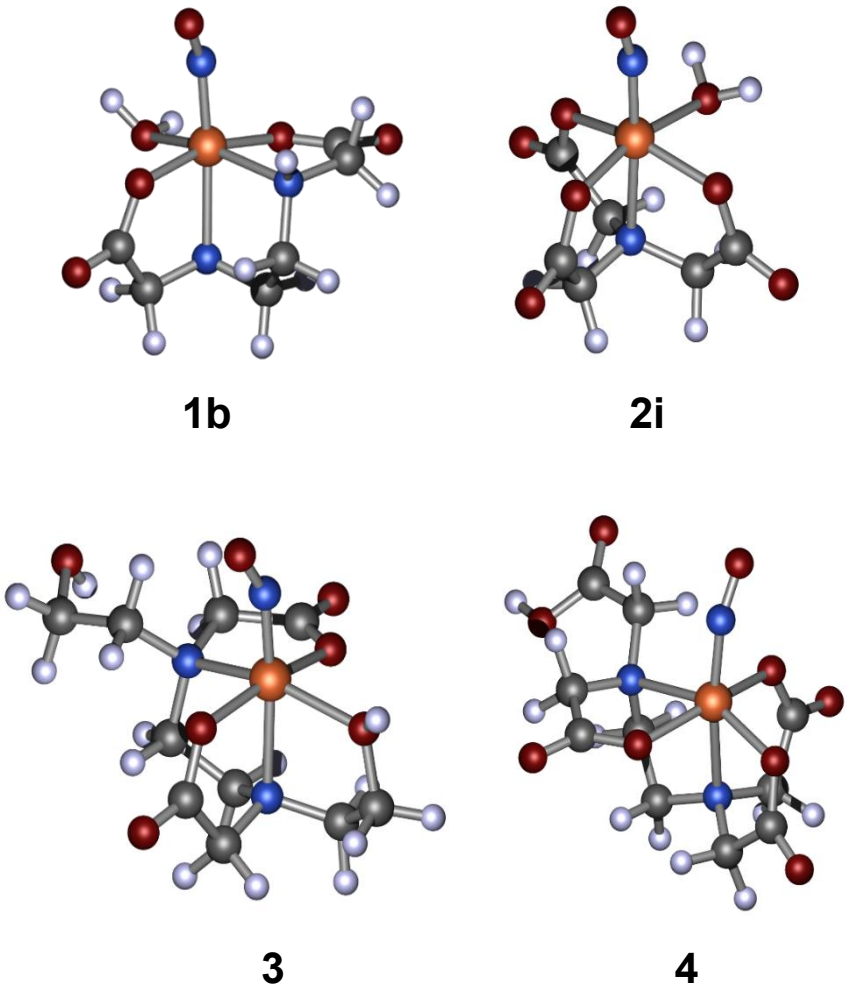

Figure 2.22: DFT-optimized minimum structures of **1b−4**. The structures illustrate the tilt of the NO group to the oxygen donor atom of the carboxylate function that is perpendicular to the basal plane of the coordination octahedron. The calculations were accomplished using TPSSh/def2-TZVP, dispersion correction (D3) and COSMO(water).

The effect was analyzed with canonical bonding molecular orbitals. To simplify the investigation, the tentative octahedrally coordinated complex anion $[FeF_3(NH_3)_2(NO)]^-$ with only σ and π donors as co-ligands was considered. A DFT-based geometry optimization (BP86/def2-TZVP) results in a nitrosyl group that is bent towards a coordinated fluorido co-ligand. Among the canonical MOs, the β−HOMO clarifies the observed effect (Figure 2.23, left). The orbital shows one of the two π-bonding interactions between the NO 1π* and the Fe d orbitals. Simultaneously, there is an antibonding interaction between the nitrogen atom and the oxygen atom of the NO group as well as between the iron center and the fluorido co-ligand. This results in a nodal plane between those atoms. By bending the nitrosyl-oxygen atom to the fluoride donor atom, a slightly bonding interaction is generated. This can be transferred to complexes with aminecarboxylato co-ligands. The smaller bond angle in the tentative model compound, however, leads to a better bonding overlap between the terminal atoms of the F–Fe–N–O moiety. The interaction can be seen, although to a lesser extent, in the β-HOMO of the nitrosyl-iron compounds with aminecarboxylates (Figure 2.23, right).

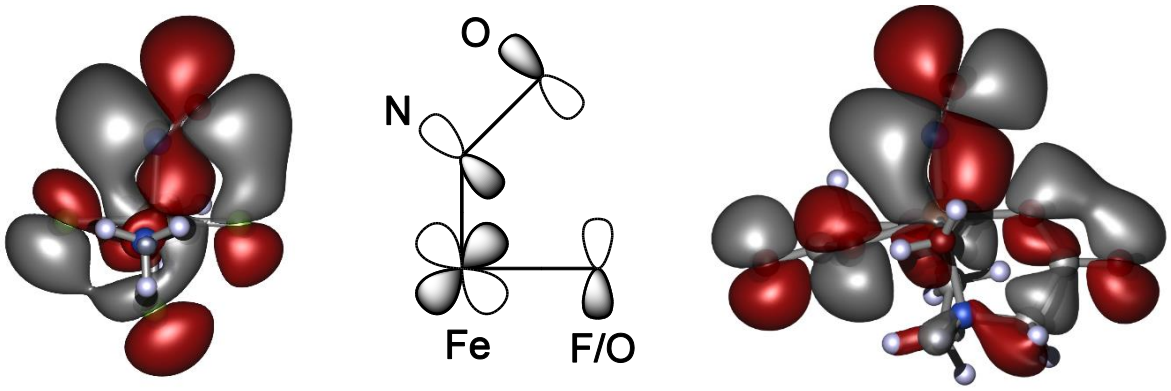

Figure 2.23: Left: β-HOMO of the tentative $[FeF_3(NH_3)_2(NO)]^-$ model complex (BP86/def2-TZVP, isovalue 0.008); middle: schematic illustration of the bonding overlap between the nitrosyl-oxygen atom and the fluorido ligand or the oxygen atom of the carboxylate group of the aminecarboxylato co-ligand; right: β-HOMO of **1b** (TPSSh/def2-TZVP, isovalue 0.008).

In order to quantify the effect, a relaxed surface scan of the X−Fe–N–O torsion angle (whereby X stands for one of the four donor atoms in the complex's equatorial plane) was performed in the non-polymeric species **1b** and **3**. The Fe–N–O–X torsion angles were fixed to 0° and all other coordinates were optimized to their most favorable values. Analogous results were obtained for **1b** and **3**. Figure 2.24 shows the calculated energy differences as well as the change of the Fe–N–O bond angles for the four conformations of complex **1b**. The atomic labels correspond to the nomenclature of Figure 2.1 and are related to the equatorial donor atom to which the NO ligand is bent. The calculations verify the experimentally determined conformation as minimum structure (NO bends towards O2, ∢ Fe–N–O_{exp} = 152°). The conformation with the nitrosyl group tilting towards the in-plane-carboxylato ligand O3 is thereby, marginally less stable than the conformation with the nitrosyl ligand bending to the nitrogen donor atom N3. Simultaneously, the Fe–N–O bond angle straightens up. The NO ligand is bent towards

the aqua ligand (or the hydroxyethyl group in **3**) in the least stable conformation and linearization of the Fe–N–O moiety results.

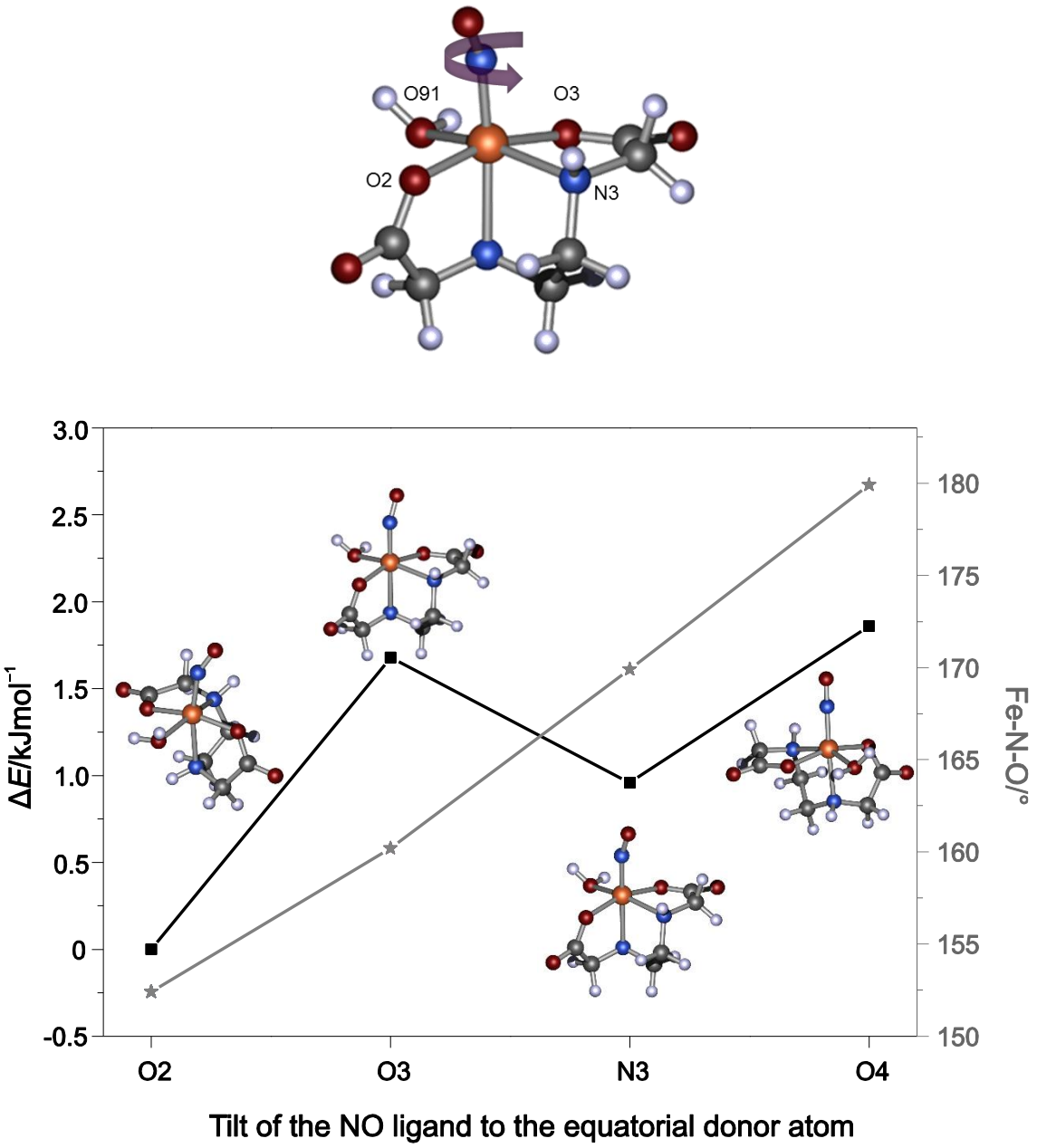

Figure 2.24: Schematic illustration (top) and results (bottom) of the relaxed surface scan on the rotation of the NO ligand about the Fe–N axis in **1b**. The energy difference ΔE and the variation of the Fe–N–O bond angle are depicted. The atomic labels correspond to Figure 2.1 and are related to the equatorial donor atom to which the NO ligand is bent. The same result is obtained for the relaxed torsion scan of the non-polymeric complex **3**. The DFT calculations were performed with TPSSh/def2-TZVP, dispersion correction (D3) and COSMO(water). The four corresponding DFT-optimized structures of **1b** are shown for graphical visualization.

The marginal bonding overlap between the carboxylate-oxygen atom and the nitrosyl-oxygen atom can be seen in the β-HOMO of the DFT-optimized complex structures. Figure 2.25 shows the relevant molecular orbitals of the four conformations of complex **1b**. The contours of these orbitals confirm the results of the relaxed surface scan (see Figure 2.24). The best orbital overlap can be seen in the β-HOMO of the minimum structure with an Fe–N–O bond angle of 152° and the NO ligand tilting towards the carboxylate-oxygen atom O2. A faintly weaker overlap exists when the nitrosyl ligand is bent towards the carboxylate-oxygen atom in the equatorial plane of the octahedron O3, with the consequence, that the Fe–N–O bond angle straightens up to 157°. No orbital overlap is found between the nitrosyl-oxygen atom and the nitrogen donor atom N3 or between the nitrosyl-oxygen atom and the aqua ligand O91, whereupon further straightening up to linearization of the Fe–N–O moiety results.
It is however worth mentioning that the energy difference of only 1.9 kJ mol^{-1} between the minimum conformation (NO bends towards O2, ∢ Fe–N–O 152°) and the maximum conformation (NO bends towards O91, ∢ Fe–N–O 180°) demonstrates the great electronic flexibility of the Fe–N–O system.

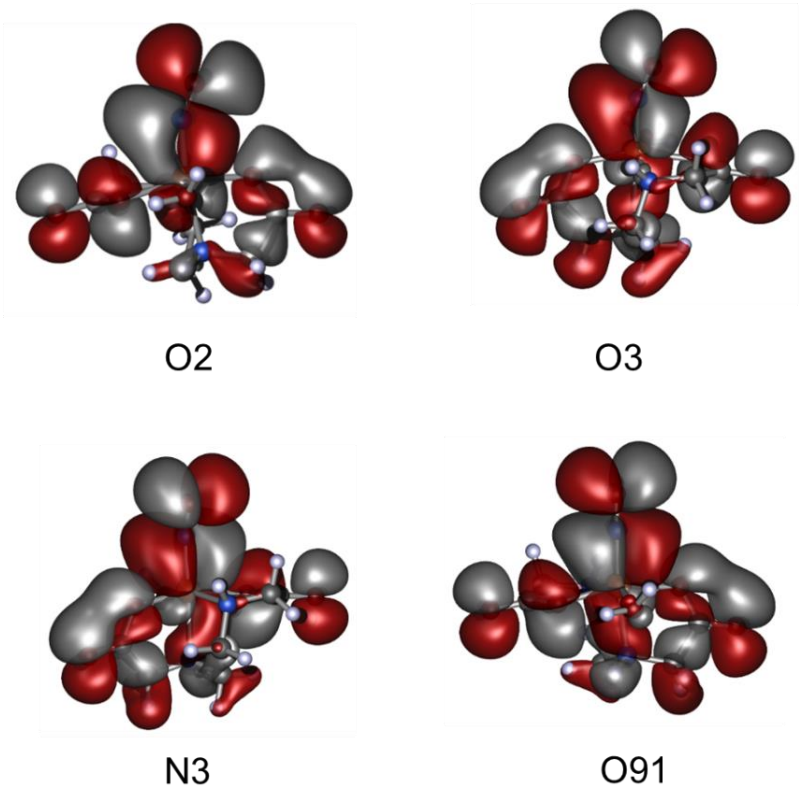

Figure 2.25: β-HOMOs of the four conformations in the relaxed surface scan of **1b**. The labels are related to the nomenclature of Figure 2.1 and correspond to the specific equatorial donor atom to which the NO ligand is bent. The DFT calculations were performed with TPSSh/def2-TZVP, dispersion correction (D3) and COSMO(water), isovalue 0.008.

2.3.7 TD-DFT calculations

In contrast to the normal DFT method, which is generally limited on the electronic ground state of a molecule, the time-dependent DFT (TD-DFT) formalism is able to account for electronically excited states.[141] Excitation energies of the nitrosyl compounds **1b−4** were calculated in a TD-DFT approach in order to assign electronic transitions and their orbital contributions to the UV/Vis spectroscopic data. Three characteristic absorption bands at around 330 nm, 430 nm and 600 nm are found in the UV/Vis-spectra of the nitrosyl complexes. The TPSSh/def2-TZVP-based computed excitation energies agree with the experimental data (Figure 2.26). Table 2.21 summarizes the UV/Vis spectroscopic data and the calculated TD-DFT transitions together with the corresponding orbital contributions for the α- and for the β-spin manifold (see also the energy-level diagram of the HOMO-LUMO region of **1b** on page 39). Distinct orbital contributions can be assigned to the calculated wavelengths. Several strong excitations are calculated in the UV region between 300 nm and 380 nm. They are due to a β-transition from the aminecarboxylato co-ligand into the β-LUMO with a Fe d_{xy} character and into the Fe−NO π antibond, respectively. An α-transition is observed in **1b** and **3**, stemming from an Fe $d_{x^2-y^2}$ to NO charge transfer. Strong excitations are computed as well in the blue region of the electromagnetic spectrum between 420 nm and 490 nm. An electronic-charge transfer transition from Fe-centered MOs with a $d_{x^2-y^2}$or a d_{z^2} character into the NO 1π* orbitals occurs within the α-spin manifold. The transitions in the β-spin manifold correspond to excitations from the Fe–NO π bond either into the Fe–NO π antibond or into the Fe-centered MOs with a Fe $d_{x^2-y^2}$ and a d_{z^2} character, respectively. Weak excitations are calculated in the red region of the electromagnetic spectrum between 600 nm and 690 nm. These are responsible for the dark green color of the aqueous compounds. The color is due to a β-transition from the Fe−NO π bond either into the Fe−NO π antibond or into the iron-centered β-LUMO with a predominantly d_{xy} character.

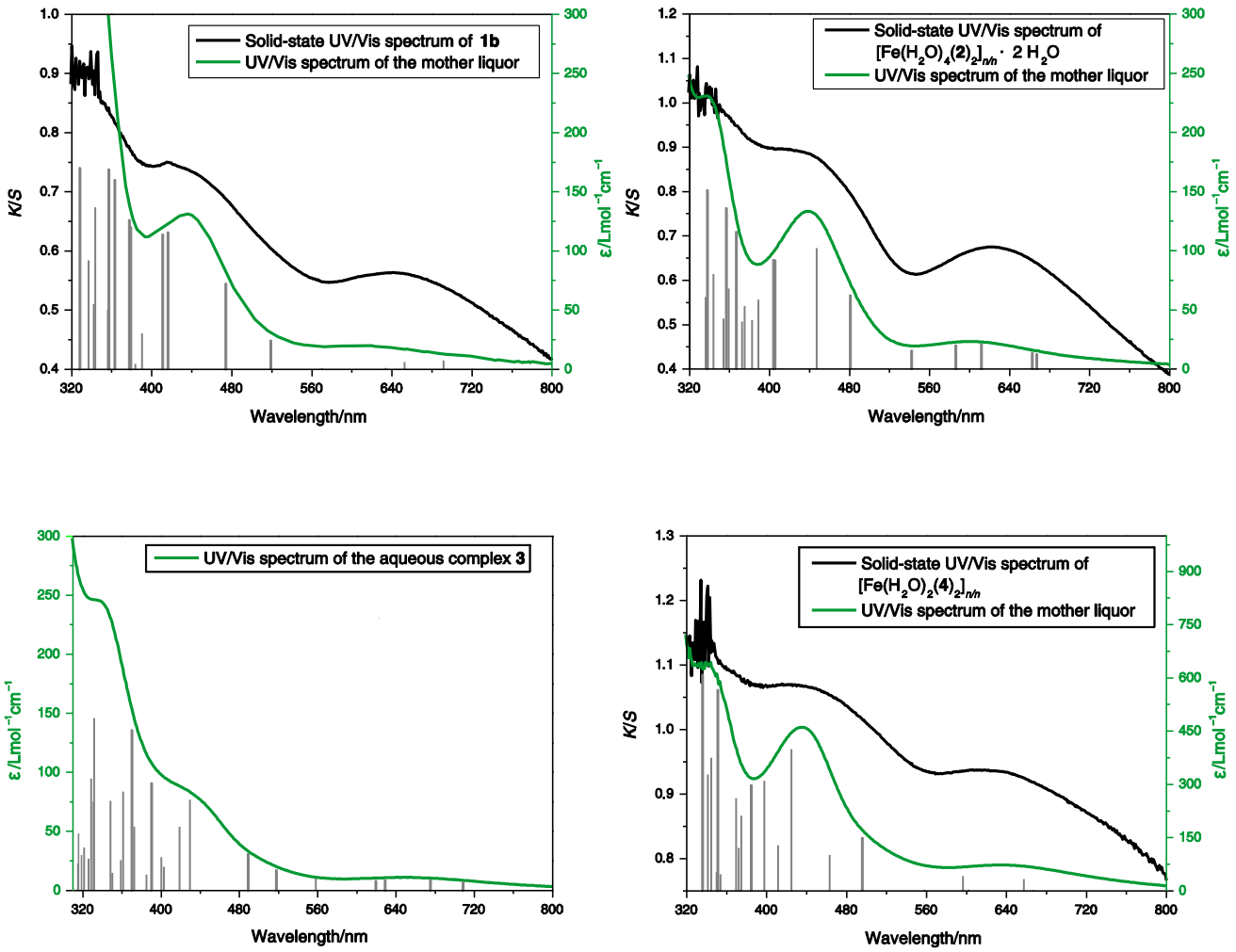

Figure 2.26: TD-DFT calculated excitation energies (vertical gray lines) and UV/Vis spectra of complexes **1b**–**4**. The solid-state UV/Vis spectrum of **3** is missing because of the low crystal yield.

Table 2.21: Calculated TD-DFT excitations (TPSSh/def2-TZVP) together with the corresponding orbital contributions in the α- and in the β-spin manifold as well as the experimentally determined UV/Vis spectroscopic data of complexes **1b**−**4** (sol.: aqueous reaction solution, cry.: crystalline compound).

	UV/Vis sol. / crys.	TD-DFT	α−transition	β−transition
1b	342 / −	328, 343, 362, 377.	Fe $d_{x^2-y^2}$ → NO 1π*	edda → Fe d_{xy} / Fe−NO π* Fe−NO π → Fe $d_{x^2-y^2}$ / Fe d_{z^2}
	435 / 414, 430.	411, 415, 473.	Fe $d_{x^2-y^2}$ / Fe d_{z^2} → NO 1π*	Fe−NO π → Fe−NO π* / Fe $d_{x^2-y^2}$ / Fe d_{z^2}
	617 / 644	653, 691.	−	Fe−NO π → Fe−NO π* / Fe d_{xy}
2(i)	339 / −	338, 367, 375.	−	nta → Fe d_{xy} / Fe−NO π* Fe−NO π → Fe d_{z^2}
	439 / 433	389, 447, 481.	Fe $d_{x^2-y^2}$ / Fe d_{z^2} → NO 1π*	Fe−NO π → Fe−NO π* / Fe $d_{x^2-y^2}$
	602 / 622	586, 611, 662.	−	Fe−NO π → Fe−NO π* / Fe d_{xy}
3	337 / −	308, 331, 370.	Fe $d_{x^2-y^2}$ → NO 1π*	bhedda → Fe d_{xy} / Fe−NO π* Fe−NO π → Fe $d_{x^2-y^2}$ / Fe d_{z^2}
	422 / −	390, 430.	Fe $d_{x^2-y^2}$ / Fe d_{z^2} → NO 1π*	Fe−NO π → Fe−NO π* / Fe $d_{x^2-y^2}$
	650 / −	619, 675.	−	Fe−NO π → Fe−NO π* / Fe d_{xy}
4	342 / −	335, 350, 354.	−	edta → Fe d_{xy} / Fe−NO π* Fe−NO π → Fe d_{z^2}
	435 / 432	425, 495, 557.	Fe $d_{x^2-y^2}$ / Fe d_{z^2} → NO 1π*	Fe−NO π → Fe−NO π*
	634 / 623	596, 657.	−	Fe−NO π → Fe−NO π* / Fe d_{xy}

2.3.8 Structural optimizations and comparison of the coordination isomers of [Fe(edda)(H_2O)(NO)] (**1**) and [Fe(edda)(H_2O)$_2$] (**5**)

The tetradentate chelate ligand edda gives rise to different coordination isomers (see also the overview of numbered compounds). On the one hand, four isomers are plausible for the nitrosyl species **1**: the nitrosyl ligand can coordinate either in *trans* position to one of the nitrogen donor atoms of the co-ligand (**1b** and **1c**) or in *trans* position to a carboxylate-oxygen atom (**1d**). In the fourth possible coordination isomer (**1a**), the co-ligand coordinates *meridionally* to the iron center and the nitrosyl ligand coordinates in *trans* position to the aqua ligand. On the other hand, three coordination isomers are probable for the precursor compound **5**: both aqua ligands can coordinate *trans* to each other (**5a**). The aqua ligands can also coordinate *cis* to each other, whereby a coordination *trans* to both nitrogen donor atoms of the edda co-ligand (**5b**) or *trans* to one nitrogen donor atom and one carboxylate-oxygen atom of the co-ligand (**5c**) is plausible.

Structure optimizations were performed on the different coordination isomers of [Fe(edda)(H_2O)(NO)] (**1**) and [Fe(edda)(H_2O)$_2$] (**5**). It was tested whether the crystallized species **1b** and **5b** represent the minimum structure in solution as well. The DFT results are listed in Table 2.22 and Table 2.23.

Table 2.22: DFT-calculated energy differences of the coordination isomers of [Fe(edda)(H_2O)(NO)] (**1**). The DFT calculations were performed with TPSSh/def2-TZVP, dispersion correction (D3) and COSMO(water).

	1a	**1b**	**1c**	**1d**
ΔE/kJmol^{-1}	16.1	0	7.1	4.1

Table 2.23: DFT-calculated energy differences of the coordination isomers of [Fe(edda)(H_2O)$_2$] (**5**). The DFT calculations were performed with TPSSh/def2-TZVP, dispersion correction (D3) and COSMO(water).

	5a	**5b**	**5c**
ΔE/kJmol^{-1}	34.9	0	8.6

The calculations reveal the energetic minimum for **1b** and **5b**, respectively. However, the energies of the coordination isomers **1c**, **1d** and **5c** are found close to the minimum structures, which indicates that they coexist in solution. The energetic maxima and, therefore, the most unfavorable structures are obtained for the *meridionally* (referring to the edda coordination) coordinated isomers **5a** and **1a**. This is most likely due to the steric hindrance of the edda co-ligand.

2.3.9 Structural optimization of $[Fe(hedtra)(NO)]^-$

A geometry optimization was performed on the $[Fe(hedtra)(NO)]^-$ complex anion with the highest stability constant K_{NO} according to van Eldik's survey.[87,89] The hedtra co-ligand is a derivative of edta, whereby one of the carboxymethyl functions is replaced by a hydroxyethyl residue. The starting geometry was, thus, constructed from the minimum structure of complex **4** by replacing the dangled protonated carboxymethyl function by a hydroxyethyl residue. The energetic minimum structure of the $[Fe(hedtra)(NO)]^-$ species is shown in Figure 2.27. The calculation results in an Fe–N–O bond angle of 153.1° and a N–O stretching vibration of 1786 cm^{-1}. The DFT-optimized structure confirms the structural feature of quartet-$\{FeNO\}^7$ compounds with aminecarboxylates as described in chapter 2.3.6.2: the NO group is bent towards the oxygen atom of a carboxylate group that is perpendicular to the basal plane of the coordination octahedron.

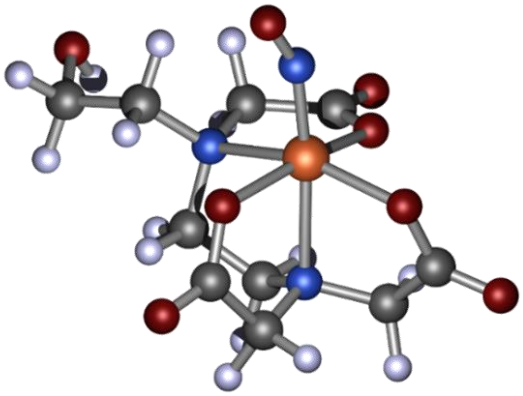

Figure 2.27: Energetic minimum structure of the $[Fe(hedtra)(NO)]^-$ complex anion. The DFT calculation was accomplished with TPSSh/def2-TZVP, dispersion correction (D3) and COSMO(water).

2.4 The Influence of Local Transport Processes on Chemical Reactions in Bubble Flows – SPP1740

An important research area in the field of engineering science is the investigation of multiphase systems in so-called "bubble columns". The interplay between hydrodynamic conditions, mass transport as well as reaction kinetics is being intensely studied to confirm industrial oxygenation products with high yield and high selectivity. The DFG priority program SPP1740 assembles chemists and engineers to investigate the reaction of gas bubbles in a liquid phase, when they are consumed in a chemical reaction. To enable the investigation of a specific chemical reaction system on a larger scale, several conditions must be met: an *in-situ* traceability of the reaction progress, an adjustability of the intrinsic reaction kinetics and the availability of a suitable solvent. $\{FeNO\}^7$(S = 3/2) complexes with aminecarboxylato co-ligands fulfill these requirements and are, moreover, synthesized from inexpensive chemicals. During the synthesis of the complex compounds, a distinct color change from the colorless Fe^{II} precursor

solution to the characteristic dark green quartet-{FeNO}^{7} species is observable. The colored Fe–NO reaction product can then be visualized *in-situ* around the NO bubble. Furthermore, the complexes are detectable by various analytical methods and the reaction rate can be influenced by the choice of different chelating ligands.

The Fe−NO reaction system was tested in a gas-liquid flow apparatus at the Institute for Microprocess Engineering of the Karlsruhe Institute of Technology in a collaboration with Dr. Günter Rinke and Dipl. Ing. Daniela Schurr.[117,118] This flow system consists of alternating gaseous bubbles and liquid slugs. It can characterize real-time bubble dynamics and measures localized concentrations around the bubbles with confocal Raman spectroscopy. The experimental set up of this so-called Taylor flow apparatus is shown in Figure 2.28.

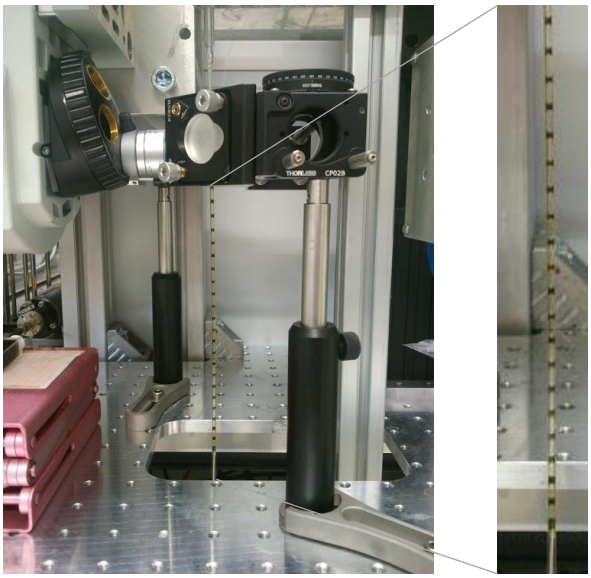

Figure 2.28: Experimental set up of the Taylor flow apparatus.[117,118] Alternating gaseous NO bubbles and liquid slugs of the aqueous dark green Fe−NO reaction product are illustrated.

In order to verify whether the Fe−NO reaction system provides a characteristic analyzable Raman active absorption band for concentration measurements, Raman spectra were performed on several aqueous nitrosyl-iron compounds with an argon-ion laser excitation wavelength of 488 nm. The results of the Raman measurements are shown in Figure 2.29. The spectra reveal the characteristic N–O stretching vibration band. However, the intensity of this signal is too low for concentration measurements at a localized spot. All quartet-{FeNO}^{7} complexes show an intense vibration band at 500 cm^{-1}. The intensity of this vibration signal varies depending on the aminecarboxylato co-ligand. Reference Raman measurements of the Fe^{II} aminecarboxylate precursor compounds as well as of free NO in water demonstrate that the vibration band stems from NO-binding. DFT calculations attribute the absorption band to the Fe–N(O) stretching vibration. Table 2.24 summarizes the Raman data of the NO-stretching vibration signals as well as of the intense Fe–N(O) vibration bands together with the computed DFT-based values.

Table 2.24: Raman data of the NO-stretching vibration bands as well as of the intense Fe−N(O) vibration bands together with the calculated DFT-based values in cm^{-1} (TPSSh/def2-TZVP, dispersion correction (D3), COSMO(water)).

	$\tilde{\nu}(Fe-N_O)_{exp.}$	$\tilde{\nu}(Fe-N_O)_{calcd}$	$\tilde{\nu}(N-O)_{exp.}$	$\tilde{\nu}(N-O)_{calcd}$
[Fe(edda)(H_2O)(NO)]	486	457	1768	1786
$[Fe(edta)(NO)]^{2-}$	494	461	1786	1774
$[Fe(H_2O)_5(NO)]^{2+}$	456	496	1821	1886
$[Fe(hedtra)(NO)]^{-}$	499	463	1786	1772

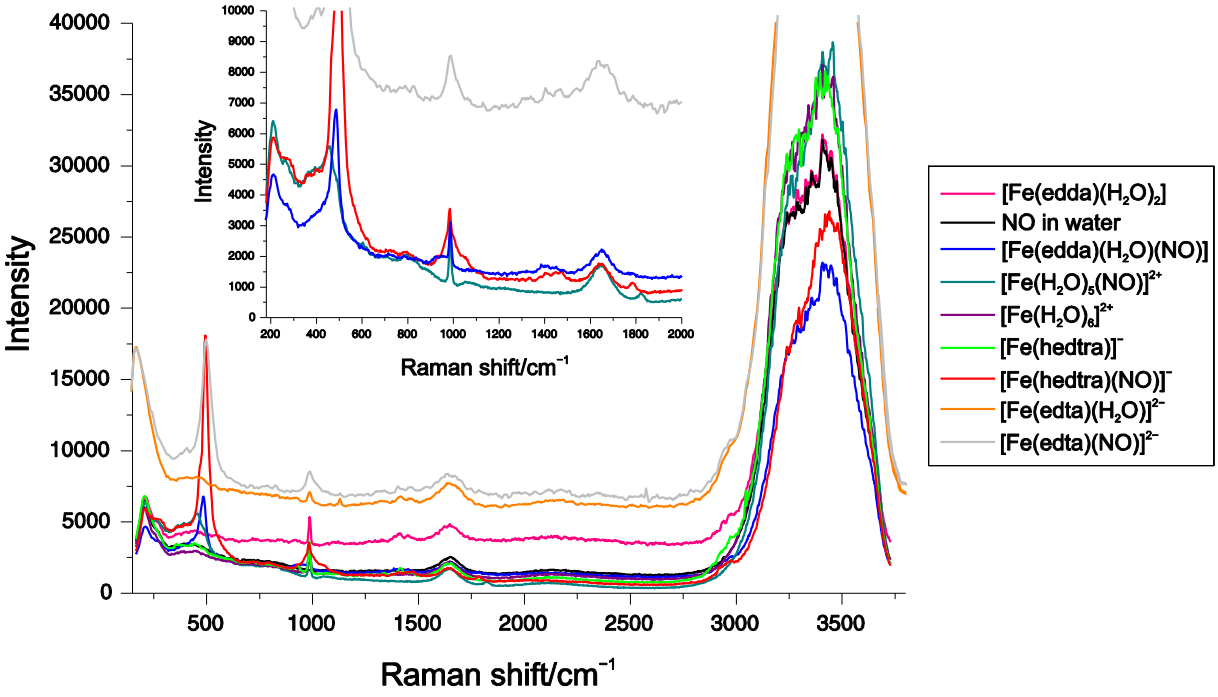

Figure 2.29: Raman spectra of some aqueous quartet-{FeNO}^{7} complexes with aminecarboxylato co-ligands, of free NO in water and of the colorless Fe^{II} aminecarboxylate precursor compounds. The inset shows the characteristic N–O stretching vibration band of the nitrosyl species at around 1800 cm^{-1}. The spectra were recorded with 488 nm laser excitation.

The confocal Raman-spectroscopy subsystem operates with a pulsed Nd:YAG laser (wavelength of 532 nm). But the characteristic Fe–N(O) vibration band can be observed only with 488 nm laser excitation. This indicates resonance-Raman activity. The laser wavelength of 488 nm is close in energy to the electronic-charge transfer transition of the {FeNO}^{7}(S = 3/2) species at around 430 nm (see their UV/Vis spectroscopic data in chapter 2.1.6). The frequency coincidence leads to a high-intensity Fe–N(O) absorption band that, however, is not detectable with 532 nm laser excitation because of the reduced Raman scattering.

The Fe–NO reaction system was further investigated in a cooperation with M.Sc. Katharina Haase and Prof. Dr. Christian Kähler[119] at the Institute of Fluidmechanics and Aerodynamics of the *Bundeswehr* University Munich. The *in-situ* traceability of the reaction progress was utilized in order to visualize the darkened mass transport from a free rising NO bubble in an Fe^{II} aminecarboxylate precursor solution with shadow images and a tomographic camera set up. The aminecarboxylato co-ligand hedtra was used because of its good solubility in aqueous solution and the high stability of the Fe/hedtra/NO species.[87,89] The NO bubbles were injected with a capillary into 10 L of a 62 mmol L^{-1} (referring to the iron content) aqueous solution of iron(II) sulfate heptahydrate, sodium hydroxide and H_3hedtra. The tomographic camera set-up and the time-resolved shadow images, which show the motion of the NO bubble, are illustrated in Figure 2.30. The NO bubble is rising in a straight path after detecting from the capillary. A cone-like form is observable until the path changes and the bubble goes into a zig-zagging motion (t = 0–0.026 s). The Fe–NO reaction product is formed in the shape of two trails behind the bubble (t = 0.026–0.053 s). These trails grow in length until the bubble changes its direction and the reaction product diffuses. After the change in curvature, the two trails begin to reform until the next path change occurs (t = 0.07–0.1 s).

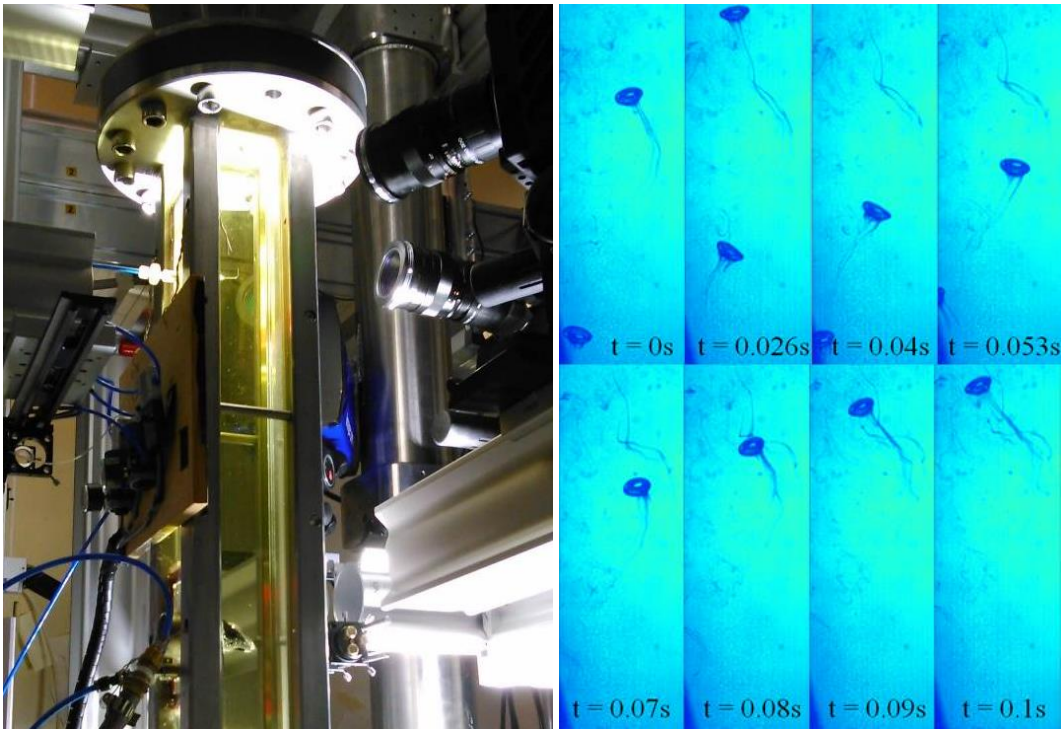

Figure 2.30: Left: schematic tomographic 3D camera setup with triggered background light, right: time-resolved shadow images of the darkened mass transport from the free rising NO bubble in the Fe^{II} aminecarboxylate precursor liquid.[119]

3 Discussion

3.1 Characterization and crystallization of stable {FeNO}^{7}(*S* = 3/2) compounds with aminecarboxylates

In the context of this thesis, four crystalline octahedral quartet-{FeNO}^{7} complex compounds with polydentate aminecarboxylato co-ligands were characterized by X-ray diffraction. The aqueous reaction solutions of the complexes are stable against NO loss upon stripping with inert gas or upon the application of vacuum. They share a bent Fe–N–O moiety with bond angles between 148° and 165° and a nitrosyl ligand that is coordinated *trans* to a nitrogen donor atom of the aminecarboxylato co-ligand. The Fe–N(O) bond lengths range from 1.76 Å to 1.78 Å and the N–O bond distances are found between 1.13 Å and 1.16 Å. The $\tilde{\nu}$(NO) stretching vibration bands are observed between 1761 cm^{-1} and 1791 cm^{-1}. As the experimentally determined Fe–N(O) and N–O bond lengths as well as the $\tilde{\nu}$(NO) stretching vibration signals match perfectly with the data of quartet-{FeNO}^{7}complexes known from literature, the average Fe–N–O bond angles of about 150° in **1b** · ½ H_2O, **3** and $[Fe(H_2O)_2(\mathbf{4})_2]_{n/n}$ mark the lower limit of typical values for quartet-{FeNO}^{7} centers.[4,46,60,64,81,98–115] The maximum Fe–N–O bond angle of 165° is found in the nitrosyl-containing building block **2** of the complex polymer $[Fe(H_2O)_4(\mathbf{2})_2]_{n/n}$ · 2 H_2O. The IR- and UV/Vis data of the crystalline nitrosyl compounds agree suitably with the spectroscopic data of their mother liquors. Moreover, the IR and UV/Vis solution data match those reported by the van Eldik group.[87]

The crystallization of the {FeNO}^{7}(*S* = 3/2) complexes lasted from two weeks for compound **3** to one year for the complex polymer $[Fe(H_2O)_4(\mathbf{2})_2]_{n/n}$ · 2 H_2O. The coordination polymers $[Fe(H_2O)_2(\mathbf{4})_2]_{n/n}$ and $[Fe(H_2O)_4(\mathbf{2})_2]_{n/n}$ · 2 H_2O contain bridging dicationic $[Fe(H_2O)_{4/2}]^{2+}$ moieties instead of the attempted sodium or potassium counterions. A closer look at the hydrogen-bond network in the crystal structure of these compounds shed light on the unusual structure motif of the complex polymers. The structures are comprised of a strong three-dimensional hydrogen-bond pattern, whereby hydrogen bonds are formed between the aqua ligands of the bridging dicationic $[Fe(H_2O)_{4/2}]^{2+}$ moieties and the carboxyl-oxygen atoms of neighboring nitrosyl-containing monoanions **2** and **4**. In the nitrosyl-containing monoanion **4**, one of the chelating ligand's carboxymethyl function is protonated and bends away from the iron center. The hydrogen atom bound to the dangling carboxymethyl group forms a hydrogen bond to a carboxyl-oxygen atom of an adjacent Fe/Hedta/NO entity. This explains why the crystallization succeeded only under acidic conditions. A strong hydrogen-bond network also prevails in the crystal structure of **1b** · ½ H_2O as well as in the crystal structures of the less stable quartet-{FeNO}^{7} complex compounds with derivatives of the tridentate iminodiactetate as co-ligands. The less stable complexes bear additional aqua ligands to complete the octahedral coordination sphere of the central metal. These aqua ligands form hydrogen bonds to carboxyl-oxygen atoms of neighboring complex molecules.[4,115] To sum up, the crystallization of the {FeNO}^{7}(*S* = 3/2) complexes with aminecarboxylato co-ligands from aqueous solution is hardly correlated to the ability to form a strong hydrogen-bond network in the crystal structure of the compounds.

3.2 The stability of the Fe–NO linkage

While the nitrosyl-iron complexes in this thesis contain aminecarboxylato co-ligands of denticity four and higher, the complexes of the less stable subclass are comprised of aminecarboxylato co-ligands of limited denticity and aqua ligands that complete the octahedral environment of the iron atom.[4,115] In contrast to the less stable representatives, the aqueous reaction solutions of the nitrosyl-iron complexes in this thesis are stable against NO loss when treated with an inert gas stream or when subjected to low pressure. The complex stability is obviously not influenced by just the spectator ligand, the Fe–NO linkage is also connected to the specific aminecarboxylato co-ligand. These stability differences will be discussed in the following chapter.

3.2.1 X-ray results, DFT-based structural optimizations and broken-symmetry calculations

The molecular structures in crystals of $\{FeNO\}^7$ (S = 3/2) complexes with aminecarboxylates do not allow accurate conclusions concerning the observed stability differences. Table 3.1 compares experimental and computed data of the stable complexes (**1b**–**4**) with selected less stable representatives.[4,115] The experimental and the DFT results reveal similar structural parameters for the Fe–N–O moiety. The broken-symmetry calculations[138,139] give comparable magnitudes of the overlap integrals $S_{\alpha\beta}$ as well as Heisenberg-coupling constants J.[140] All of these results indicate the same bonding situation as for the less stable compounds: an almost covalent bonding character of the Fe–NO linkage with strong antiferromagnetic coupling between the iron center and the NO ligand.

Table 3.1: Experimental (upper rows) and DFT (lower rows) structural data of the Fe–N–O moiety in **1b–4** and in the less stable complexes [Fe(dipic)$(H_2O)_2$(NO)] (**II**), [Fe$(H_2O)_2$(ida)(NO)] (**III**), and [Fe$(H_2O)_2$(NO)(phida)] (**IV**). The magnitudes of the overlap integrals $S_{\alpha\beta}$ and the Heisenberg coupling constants J[140] were derived from broken-symmetry calculations.[138]

	II[a]	**III**[a]	**IV**[a]	**1b**[b]	**2(i)**[b]	**3**[b]	**4**[b]
Fe1–N1/Å	1.76	1.78	1.78	1.77	1.75	1.78	1.76
	1.77	1.78	1.78	1.78	1.77	1.78	1.78
N1–O1/Å	1.14	1.11	1.17	1.16	1.15	1.13	1.16
	1.15	1.16	1.16	1.17	1.17	1.17	1.17
Fe1–N1–O1/°	167	155	148	148	165	150	149
	167	151	153	152	161	152	153
$\tilde{\nu}$(NO)/cm^{-1}	1806	1772	1764	1761	1791	1782	1781
	1832	1781	1792	1786	1808	1791	1774
$S_{\alpha\beta}$ (HOMO–3)	0.76	0.76	0.76	0.75	0.74	0.75	0.75
$S_{\alpha\beta}$ (HOMO–4)	0.76	0.76	0.76	0.81	0.79	0.81	0.77
J/cm^{-1}	–2205	–2268	–2316	–1948	–1891	–1943	–1813

[a] The DFT data resulted from calculations on the B97-D/def2-TZVP level of theory, dispersion correction (D3) and COSMO-RS(water). Experimental and computed data were taken from Reference [4]. [b] The DFT calculations were performed with TPSSh/def2-TZVP, dispersion correction (D3) and COSMO(water).

3.2.2 Reaction equilibrium in aqueous solution

The stability differences are observed in the aqueous reaction solutions of the nitrosyl-iron compounds. Apart from the intrinsic complex stability of the nitrosyl-iron compounds, the aqueous reaction equilibrium has to be taken into consideration. The relevant reaction equilibria for the edta co-ligand are summarized in Scheme 3.1.

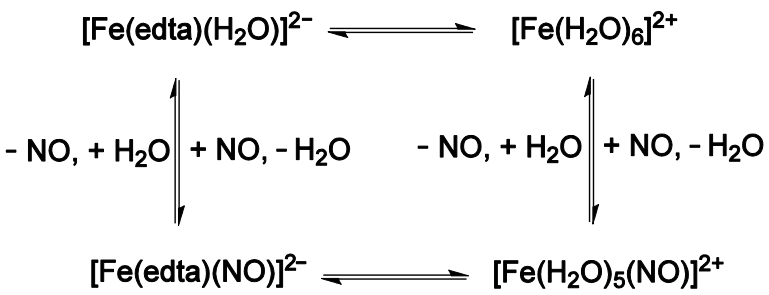

Scheme 3.1: Relevant equilibria in the aqueous reaction solution of the Fe/edta/NO species.

In the case of stable reaction solutions with edta as the co-ligand (lg β = 6.3 at pH 5 for the nitrosyl species[87,90], lg β = 14.94 at 0.1 molL^{-1} ionic strength for the aqua species[142]), the reaction equilibrium is located predominantly on the left-hand side of Scheme 3.1 and only minor quantities of both aqua species prevail in the aqueous reaction medium. When the hexadentate edta co-ligand is substituted by the tridentate ida co-ligand (lg β = 4.1 at pH 5 for the nitrosyl species[87,90], lg β = 5.45 at 1 molL^{-1} ionic strength for the aqua species[143]), the less stable aminecarboxylate complex with and without a bonded nitrosyl ligand causes higher amounts of the residual aqua species. After the treatment with NO, the green nitrosyl-iron solutions contain either a higher residual concentration (instable) or a lower residual concentration (stable) of the unstable $[Fe(H_2O)_5(NO)]^{2+}$ complex cation which is destroyed upon stripping with an inert-gas stream or upon subjection to low pressure. On continuous readjustment of the solution equilibria, the aquated nitrosyl species decomposes and the original colorless solution of the Fe^{II} aminocarboxylate complex results, as observed for the aqueous solutions of the less stable compounds when exposed to an inert gas stream.[4]

3.2.3 Structural considerations – Comparison of {FeNO}^{7}(S = 3/2) complexes with the nitrosyl-free Fe^{II} and Fe^{III} compounds

It was stated in chapter 3.2.1 that, at first sight, the molecular structures barely reflect the observed stability differences. In order to make a statement about the oxidation state of the iron atom in the stable and less stable compounds, structural parameters of the corresponding Fe^{II} and Fe^{III} aminecarboxylate species are compared. For the non-polymeric nitrosyl species **1b** and **3**, the Fe^{II} aminecarboxylate precursor compounds **5b** and **7** were crystallized. Structural data of the Fe^{III} complexes were derived from DFT calculations. Data of selected less stable nitrosyl-iron compounds and the analogous nitrosyl-free compounds were taken from the literature.[4,144–148] Table 3.2 summarizes the average Fe–$O_{Carboxylate}$ and Fe–OH_2/$OH_{Hydroxyethyl}$ bond distances in quartet-{FeNO}^{7} compounds arranged according to their stability constants K_{NO} (pursuant to van Eldik's survey[87,90]) together with the data of the Fe^{II} and Fe^{III} complexes.

The DFT result of the experimental inaccessible least stable $[Fe(H_2O)_5(NO)]^{2+}$ complex cation lies close to the data of the corresponding $[Fe^{II}(H_2O)_6]^{2+}$ complex, indicating an Fe^{II} state in that complex. In contrast, the structural parameters of the stable Fe–NO compounds [Fe(edda)(H_2O)(NO)] (**1b**) and [Fe(bhedda)(NO)] (**3**) are found between the Fe^{II} and Fe^{III} complexes. Hence, significant admixture of the Fe^{III} state can be discussed for these compounds. The Fe–NO stability is obviously correlated to the larger weight of the trivalent state of the iron center. Even though the unstable [Fe(dipic)(H_2O)$_2$(NO)] (**II**) complex shows a considerably Fe^{II} character, a distinct Fe^{III} character prevails in the [Fe(H_2O)$_2$(NO)(oda)] (**I**) compound which, however, belongs to the less stable subclass.

In order to quantify the weight of the Fe^{III} character in the {FeNO}^{7}(S = 3/2) complexes, Fe^{II} and Fe^{III} entities of the same overall structure are considered. For this purpose, the heptacoordinated $[Fe^{II}(edta)(H_2O)]^{2-}$ and $[Fe^{III}(edta)(H_2O)]^{-}$ compounds are compared. The mean Fe–$O_{Carboxylate}$ bond length in $[Fe^{III}(edta)(H_2O)]^{-}$ is 2.12 Å[149] and 2.24 Å in $[Fe^{II}(edta)(H_2O)]^{2-}$ [150]. They differ by 0.12 Å,

which is – due to some degree of covalency in the Fe–O bonds – a little bit smaller than the difference of the high-spin ionic radii for hexacoordinated Fe^{II} and Fe^{III} centers of 0.14 Å.[151] The difference between the mean $Fe–O_{Carboxylate}$ bond lengths in the nitrosyl compound **3** and its Fe^{II} precursor species **6** is 0.06 Å (for the bhedda co-ligand) and 0.07 Å for the oda co-ligand. Consequently, the ferric $Fe^{III}(NO^{–})$ mesomer contributes with a weight of roughly one half to the electronic states of the stable [Fe(bhedda)(NO)] (**3**) and the unstable $[Fe(H_2O)_2(NO)(oda)]$ (**I**) species.

To conclude, the following criteria have to be met for a stable quartet-$\{FeNO\}^7$ complex: an adequate stability constant K_{NO} to ensure only minor quantities of the unstable aqua species in the aqueous reaction medium and, moreover, a considerable weight of the ferric $Fe^{III}(NO^{–})$ part.

Table 3.2: Comparison of experimental structural data (upper rows) and DFT results (lower rows) of several {FeNO}^{7}(S = 3/2) complexes, arranged according to their stability constants K_{NO}, with the corresponding nitrosyl-free Fe^{II} and Fe^{III} compounds. The stability constant K_{NO} of the [Fe(bhedda)(NO)] (**3**) complex is not known so far but it is assumed that the complex belongs to the stable subclass of the van Eldik series. The listed values represent the mean Fe–$O_{Carboxylate}$ and Fe–OH_2/$OH_{Hydroxyethyl}$ bond lengths in the complex compounds. Distances are given in Å.

Stability constant K_{NO} of the aqueous nitrosyl-iron complex

	$\bar{d}$ Fe–$O_{Carboxylate}$	$\bar{d}$ Fe–OH_2/$OH_{Hydroxyethyl}$
$[Fe^{II}(H_2O)_6]^{2+}$[144]	-	2.12[a]
		2.12[b]
$[Fe(H_2O)_5(NO)]^{2+}$	-	-
		2.12[b]
$[Fe^{III}(H_2O)_6]^{3+}$[145]	-	1.99[c]
		2.01[b]
$[\{Fe^{II}(H_2O)_2(oda)\}_n]$[146]	2.14	2.15
	2.11[d]	2.16[d]
$[Fe(H_2O)_2(NO)(oda)$ (**I**)][4]	2.07	2.08
	2.05[d]	2.15[d]
$[Fe^{III}Cl(H_2O)_2(oda)]$[147]	2.00	2.03
	2.00[d]	2.10[d]
$[Fe^{II}(dipic)(H_2O)_3]$[4]	2.16	2.12
	2.14[d]	2.18[d]
[Fe(dipic)$(H_2O)_2$(NO)] (**II**)[4]	2.12	2.11
	2.11[d]	2.15[d]
$[Fe^{III}(dipic)(H_2O)_3]^+$[148]	2.01	2.00
	2.01[d]	2.05[d]
$[Fe^{II}(edda)(H_2O)_2]$ (**5b**)	2.08	2.11
	2.02[e]	2.23[e]
[Fe(edda)(H_2O)(NO)] (**1b**)	2.05	2.06
	2.03[e]	2.19[e]
$[Fe^{III}(edda)(H_2O)_2]^+$	-	-
	1.94[e]	2.08[e]
$[Fe^{II}$(bhedda)] (**6**)	2.09	2.12
	2.02[e]	2.22[e]
[Fe(bhedda)(NO)] (**3**)	2.03	2.08
	2.02[e]	2.14[e]
$[Fe^{III}$(bhedda)]$^+$	-	-
	1.93[e]	2.10[e]

[a] The average Fe–OH_2 distance was taken from the crystal structure of iron(II) sulfate heptahydrate.[144] [b] The DFT results were obtained with BP86/def2-TZVP, dispersion correction (D3) and COSMO(water). [c] The average Fe–OH_2 bond length refers to the crystal structure of caesium iron alum.[145] [d] Results of the DFT calculations with TPSSh/def2-TZVP, dispersion correction (D3) and COSMO-RS(water), data were taken from Reference [4]. [e] The DFT calculations were performed with TPSSh/def2-TZVP, dispersion correction (D3) and COSMO(water).

3.2.4 Population analyses and CDA results

AOMix-FO charge decomposition analyses (CDA)[132,133], Mulliken population analysis (MPA)[134], natural population analysis (NPA)[135] and quantum theory of atoms (QTAIM)[136,137] were performed in order to draw conclusions about the charge and spin distribution in the Fe–N–O moiety.

The computed charges as well as spin densities on the iron center and on the NO ligand are consistent with an electronic structure between $Fe^{II}(NO)$ and $Fe^{III}(NO^{-})$. The population analyses do not reflect the various Fe–N–O bond angles in the compounds. Analogous charges and spin densities are calculated on the nitrosyl ligand and on the iron center in **2i**, whose structure-optimized Fe–N–O bond angle of 161° differs from the average angle of about 152° in **1b**, **3** and **4**. It turned out in chapter 3.2.3 that the stability of the NO-linkage is correlated to the weight of the $Fe^{III}(NO^{-})$ part in the compounds. Table 3.3 summarizes the average charges on the iron atom and on the nitrosyl ligand in complexes **1b**–**4** together with the computed charges of selected less stable compounds.[4] All population analyses assign more negative charges to the nitrosyl ligand and less positive charges to the iron atom in the stable complexes. This probably originates from an enhanced electron-density transfer from the higher dentate aminecarboxylato co-ligand to the iron atom in the stable complexes. The less effective nuclear charge on the iron center causes decreasing π-donation from the nitrosyl ligand into the iron d_{xz} and d_{yz} orbitals, which leads to a higher calculated negative charge on the nitrosyl group.

The QTAIM method was expected to provide an alternative description of the electronic situation in the complex compounds.[136] However, the QTAIM calculations are not in accordance with the structural considerations of the last chapter. Analogous charges are calculated on the iron atom and on the nitrosyl group in the $[Fe(H_2O)_2(NO)(oda)]$ (**I**) complex, an Fe^{III} character was discussed in the last chapter, and in the $[Fe(dipic)(H_2O)_2(NO)]$ (**II**) compound for which an Fe^{II} character was determined.

In effect, QTAIM can estimate trends for the charge distribution in the Fe–N–O moiety as MPA and NPA but is not able to predict absolute elementary charges.

Table 3.3: Average MPA, NPA and QTAIM charges on Fe and NO in stable (**1b**–**4**) as well as in selected less stable (**I**–**III**) $\{FeNO\}^7$ (S = 3/2) complexes. All values are elementary charges. The DFT calculations were performed with TPSSh/def2-TZVP, dispersion correction (D3) and COSMO(water). The MPA and NPA data of the less stable complexes were taken from Reference [4].

		I–**III**	**1b**–**4**
MPA	Fe	0.59	0.48
	NO	0.08	–0.02
NPA	Fe	1.41	1.39
	NO	–0.07	–0.16
QTAIM	Fe	1.61	1.58
	NO	–0.26	–0.32

I: $[Fe(H_2O)_2(NO)(oda)]$, **II**: $[Fe(dipic)(H_2O)_2(NO)]$, **III**: $[Fe(H_2O)_2(ida)(NO)]$.

Moreover, the AOMix-FO charge decomposition analyses (CDA) calculate almost no charge transfer between the fragments $^{2}NO^{0}$ and $^{5}Fe^{II}L$ (L = co-ligands), indicating an Fe^{II} oxidation state in the compounds. A total of one β-electron is transferred from the iron fragment to the NO fragment for the fragment combination $^{4}[Fe^{I}L]–^{1}NO^{+}$ and *vice versa* for the fragment combination $^{6}[Fe^{III}L]–^{3}NO^{-}$.
All of these results are in agreement with a bonding situation between $^{5}Fe^{2+}–^{2}NO^{0}$ and $^{6}Fe^{3+}–^{3}NO^{-}$ with an approximately zero net charge on the nitrosyl ligand because of charge compensation due to the largely covalent Fe–NO π bonds in the β-spin manifold.

3.3 Structural individualities of $\{FeNO\}^{7}$(*S* = 3/2) complexes with aminecarboxylato co-ligands

3.3.1 The steric demand of the nitrosyl ligand

All crystalline quartet-$\{FeNO\}^{7}$ complexes with aminecarboxylates share an iron central atom that is coordinated by the co-ligand via five-membered chelate rings.[4] Crystallization attempts with chelating ligands which are expected to form six-membered chelate rings (e.g. iminodiproprionate) resulted in reaction solutions that were prone to oxidation to Fe^{III}.[152] In the literature, there is only one crystalline octahedral $\{FeNO\}^{7}$(*S* = 3/2) compound with a coordinated carboxylate group that forms a six-membered chelate to the iron center.[102] The destabilizing influence of six-membered chelate rings on the $\{FeNO\}^{7}$(*S* = 3/2) complexes in aqueous solutions was also stated by the van Eldik group.[87]
With the molecular structures of the nitrosyl-iron compounds in this thesis, a structural characteristic of $\{FeNO\}^{7}$(*S* = 3/2) complexes with aminecarboxylates becomes clear once again.[4] All equatorial donor atoms are tilted away from the nitrosyl ligand and an average O–N–Fe–X angle of about 98.4° results for **1b**–**4** (with X = the four donor atoms in the equatorial plane normal to the NO group). Six-membered chelate rings would push the equatorial atoms towards the NO hemisphere and an unstable Fe–N–O moiety results (Figure 3.1). A DFT calculation supported this observation. Capturing the four equatorial donor atoms in the basal plane of the coordination octahedron in $[Fe(H_2O)_2(ida)(NO)]$ resulted in an energy loss of about 15 kJ mol^{-1} compared to the downwards-angled structure.[4]

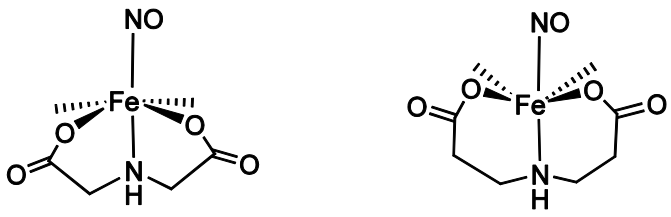

Figure 3.1: Molecular structure of $\{FeNO\}^{7}$(*S* = 3/2) complexes with five-membered chelate rings (left) and potential molecular structure with six-membered chelate rings (right). The concept is illustrated with iminodiacetate and iminodipropionate as co-ligands. In the case of six-membered chelate rings, a structure would be expected with the equatorial donor atoms tilting towards the nitrosyl group.

The steric demand of the nitrosyl ligand becomes further apparent when the monoanionic building block $[Fe(Hedta)(NO)]^-$ (**4**) of the complex polymer $[Fe(H_2O)_2(\mathbf{4})_2]_{n/n}$ is compared with its sevenfold-coordinated precursor compound $[Fe^{II}(edta)(H_2O)]^{2-}$.[150,153,154] The molecular structures are illustrated in Figure 3.2. The coordination number changes from seven to six on NO-binding and one of the chelating ligand's functional groups dangles in the nitrosyl complex. A coordinated aqua ligand is obviously sterically less demanding than a nitrosyl ligand, which is evident from the typical Fe–NO bond distance of 1.78 Å and the Fe–OH_2 bond length of 2.27 Å[150] in the heptacoordinated precursor compound.

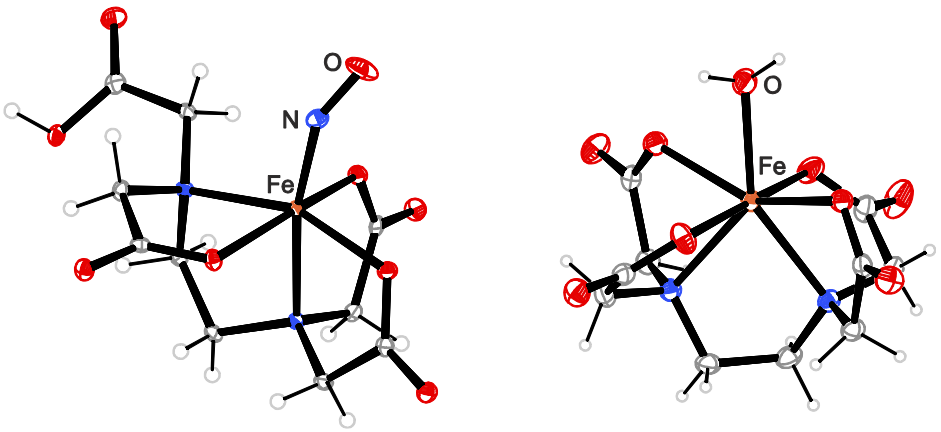

Figure 3.2: Monoanionic building block $[Fe(Hedta)(NO)]^-$ (**4**) of the complex polymer $[Fe(H_2O)_2(\mathbf{4})_2]_{n/n}$ and molecular structure of the sevenfold-coordinated precursor compound $[Fe^{II}(edta)(H_2O)]^{2-}$.[150]

All of these observations are most likely due to the steric demand of the orbital lobes of the Fe–NO π interaction. This clarifies the most stable Fe–NO linkage for the hedtra co-ligand in van Eldik's stability survey as well.[87,90] In **4**, the NO ligand competed with one of the carboxylate groups of the potentially hexadentate edta co-ligand and a complex anion with a dangled protonated carboxyl group results. This carboxyl group is, however, part of the chelate in the sevenfold-coordinated precursor compound. With its hydroxyethyl group, the hedtra co-ligand provides a hemilabile function that can bend away from the iron center to enable a free coordination site for the sterically demanding nitrosyl ligand. The geometry optimization of the Fe/hedtra/NO species results in an energetic minimum with a dangled hydroxyethyl function and three coordinated carboxylate groups (see chapter 2.3.9). The calculated Fe–N–O bond angle of 153° is consistent with the bond angles between 152° and 161° that are found in the DFT-optimized structures of **1b**–**4**. Moreover, the DFT-based N–O stretching vibration of 1786 cm^{-1} agrees suitably with the vibration signal of the aqueous species at 1777 cm^{-1}.[87]

3.3.2 Structural correlations of {FeNO}^{7}(*S* = 3/2) complexes with amine-carboxylato co-ligands

With the stable {FeNO}^{7}(*S* = 3/2) complexes of this thesis and the less stable representatives known in literature,[4] structure analyses of 13 crystalline quartet-{FeNO}^{7} compounds with aminecarboxylato co-ligands are accessible so far. Consequently, structural correlations between these complexes are considered.

3.3.2.1 Experimentally determined data of the Fe–N–O moiety

The molecular structures of all crystalline quartet-{FeNO}^{7} complexes with aminecarboxylato co-ligands share an octahedrally coordinated iron center. As already mentioned in chapter 3.2.1, the structural parameters of the Fe–N–O moiety closely resemble each other. The Fe–N(O) bond distances of **1b**–**4** are found between 1.76 Å and 1.78 Å, the N–O bond distances lie between 1.13 Å and 1.16 Å. These data match with the corresponding bond lengths of the less stable compounds with iminodiacetate derivatives as co-ligands. They are observed between 1.76 Å and 1.80 Å for the Fe–N(O) bond distances as well as between 1.09 Å and 1.17 Å for the N–O bond lengths. Within the stable compounds, the maximum Fe–N–O bond angle is found in the complex anion **2**, the only complex with merely one nitrogen donor atom coordinating to the iron center. Its Fe–N–O bond angle of 161° deviates from the Fe–N–O bond angles of about 150° that are found in the crystal structures of **1b** · ½ H_2O, **3** and $[Fe(H_2O)_2(\mathbf{4})_2]_{n/n}$. The less stable compounds show Fe–N–O bond angles between 148° and 171°, whereby the [Fe(H_2O)$_2$(NO)(phida)] (**IV**) complex has the smallest bond angle.[4] As a result, a correlation between the different aminecarboxylato co-ligands and the structural parameters of the Fe–N–O moiety is not assignable. Nevertheless, there is a relation between the Fe–N–O bond angle and the N–O stretching vibration band. The complex anion **2** with the maximum Fe–N–O angle shows the highest N–O vibration band (1791 cm^{-1}), whereas compound **1b** with the minimum Fe−N−O bond angle of 148° exhibits the lowest N−O stretching vibration band (1761 cm^{-1}). A similar low N–O stretching frequency (1764 cm^{-1}) is found in the less stable complex [Fe(H_2O)$_2$(NO)(phida)] (**IV**). This phenomenon has also been discussed in literature for sixfold-coordinated {FeNO}^{7}(*S* = 3/2) complexes.[4,46,64] A smaller Fe–N–O bond angle is connected with a lower N–O stretching vibration band. However, the correlation is not particulary pronounced in this thesis. The N–O stretching vibrations of **2**, **3** and **4**, whose Fe–N–O bond angles lie between 148° and 150°, deviate by circa 20 cm^{-1} from each other.

3.3.2.2 The correlation between the Fe–N–O bond angle and the N–O stretching vibration band in the context of DFT calculations

The experimentally determined Fe–N–O bond angle is a result of various electronic effects and is thus difficult to predict (see also chapter 2.3.6.1). DFT calculations (BP86/def2-TZVP) on the tentative model compound $[FeF_n(H_2O)_{5-n}(NO)]^{2-n}$ show that the Fe–N–O bond angle is associated with the number of anionic ligands bound to the iron atom. Structural optimizations result in decreasing Fe–N–O bond angles on increasing fluoride substitution. A similar observation is made when the carboxylate residue of the adjacent complex entity in **2** is replaced by an anionic acetato ligand. Structural optimization (TPSSh/def2-TZVP) results in an Fe–N–O bond angle of 148° that is not in satisfying agreement with the experimentally determined value of 165°. When the carboxylate residue is substituted by the weak aqua donor ligand, the DFT calculation results in an Fe–N–O bond angle of 161° so that an accurate description of the Fe–N–O moiety is achieved. This trend can be explained with ligand-donor effects that influence the effective nuclear charge of the iron center. An anionic ligand leads to a decreased effective nuclear charge on the iron center and, consequently, less π-donation from the singly occupied NO 1π*orbitals into the empty symmetrically matching Fe d_{xz} and Fe d_{yz} orbitals occurs within the β-spin manifold. As the π-donation stems from NO antibonding (1π*) orbitals, a strengthening of the Fe–N(O) bond and an increase in $\tilde{\nu}$(NO) is expected in complexes with a higher Fe–N–O bond angle. Li *et al*.[64] published the octahedrally coordinated quartet-{FeNO}^{7} complex cation $[Fe(X)(NO)(THF)(OTf)]^+$ (X = tris(1-ethyl-4-isopropylimidazolyl)-phosphine) with only neutral donor ligands, an Fe–N–O bond angle of 172° and the highest N–O stretching vibration band (1831 cm^{-1}) observed for sixfold-coordinated quartet-{FeNO}^{7} compounds so far (note the N–O stretching vibration band of free NO at 1875 cm^{-1} [33]). DFT calculations revealed the high N–O stretching vibration band and the Fe–N–O bond angle close to linearity to the strong π-donation from the NO 1π* orbitals into the Fe d_{xz} and d_{yz} orbitals.[64]

Because of the good agreement between experimental and DFT data of the Fe–N–O moiety, the computational results are considered to evaluate electronic-structural reasons for the vibration–bond angle correlation in **1b** (minimum Fe–N–O bond angle and N–O stretching frequency) and **2**(**i**) (maximum Fe–N–O bond angle and N–O stretching frequency). The amount of β-electron transfer from the 1π* orbitals of NO into the Fe d_{xz} and Fe d_{yz} orbitals can be estimated from the NO and Fe contributions in the corresponding occupied orbitals β-HOMO and β-HOMO−1. As these molecular orbitals show considerable contributions from the co-ligands, the exact amounts of Fe and NO are difficult to quantify. The strength of π-donation can also be predicted from the relative amounts of Fe and NO in the corresponding antibonding orbitals β-LUMO+1 and β-LUMO+2. The contours of these orbitals together with their relative amounts of Fe and NO as well as selected parameters of the Fe–N–O moiety and the N–O stretching frequencies are shown in Figure 3.3. As evident from the comparable Fe and NO contributions in the occupied and the unoccupied orbitals, strong π-donation is expected in both complexes. Moreover, the Fe–N(O) bond distances are similar. As a result, the higher Fe–N–O bond angle and N–O stretching frequency of **2i** is not due to stronger π-donation. The hyphothesis is also contradicted, when the $[Fe(phida)(H_2O)(NO)]$ (**IV**) compound with the least obtuse Fe–N–O bond angle of 148° within the less stable representatives is taken into consideration. The iron

atom is coordinated by two weak aqua donor ligands as well as by the tridentate phida co-ligand and the nitrosyl group coordinates *cis* to the nitrogen donor atom of the chelating ligand. A more “electron-poor” iron center is expected, whereby the NO ligand should donate significant β-electron density into the Fe d-orbitals and a straightened Fe–N–O bond angle would be expected.

To sum up, the experimentally determined structure of $\{FeNO\}^7$(S = 3/2) complexes with aminecarboxylates is very difficult to forecast. A relation between bond lengths, bond angles and IR absorptions of the individual Fe–N–O moieties is almost not assignable. However, it should be noted that a less obtuse Fe–N–O bond angle in $\{FeNO\}^7$(S = 3/2) complexes with aminecarboxylates could be correlated to a *cis*-positioned nitrogen donor atom as evident from the small bond angles of about 150° in **1b**, **2**, **4** and [Fe(H_2O)(NO)(phida)] (**IV**).

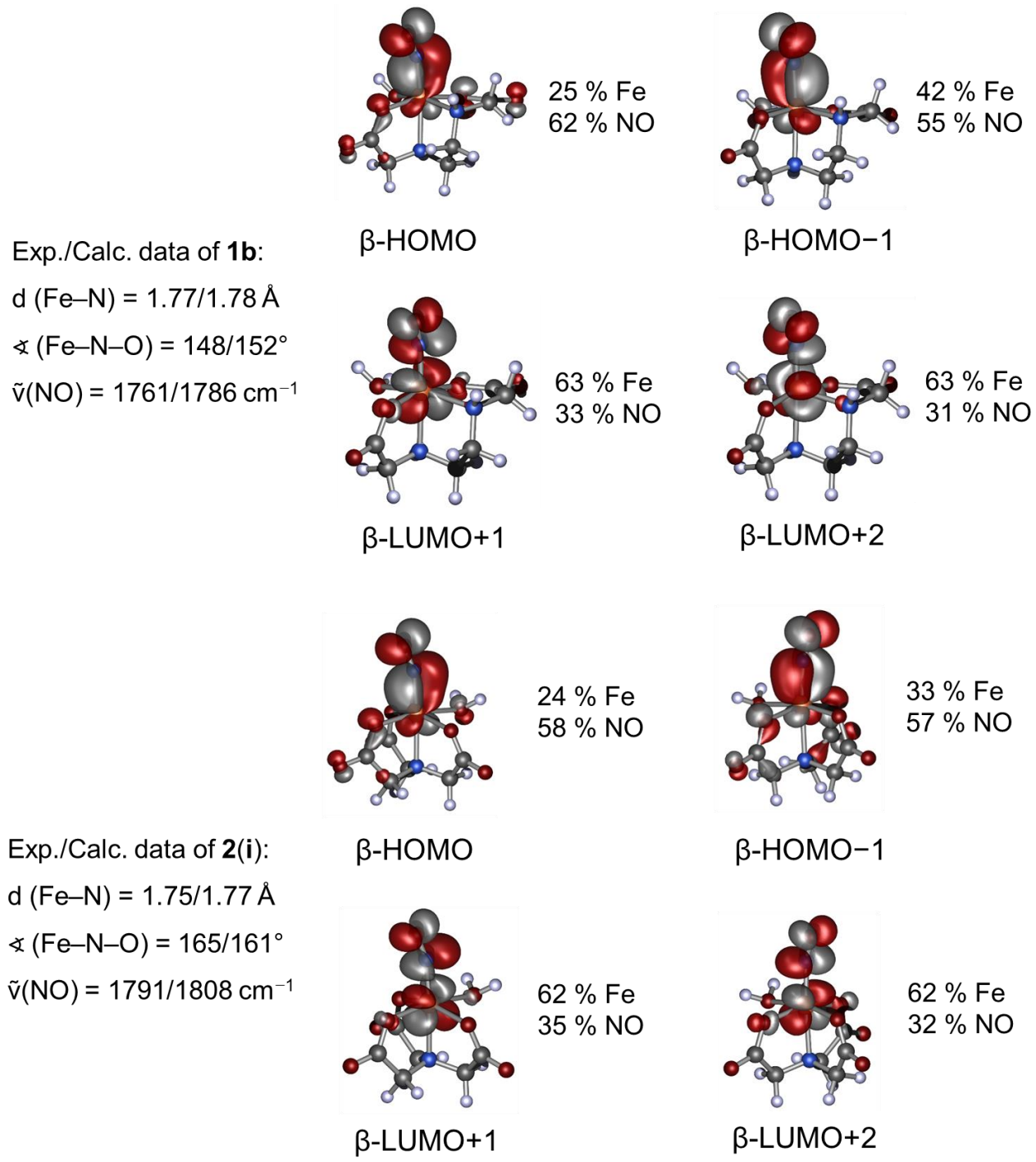

Figure 3.3: Selected data of the Fe–N–O moiety and contours of β-HOMO, β-HOMO−1, β-LUMO+1 and β-LUMO+2 together with the relative amounts of Fe and NO in **1b** (top) and **2**(**i**) (bottom). The DFT calculations were accomplished using TPSSh/def2-TZVP, dispersion correction (D3) and COSMO(water), isovalue of the orbitals: 0.04. The individual Fe and NO contributions were derived with MPA.

3.4 {FeNO}^{7}(S = 3/2) complexes with aminecarboxylates in the DFG priority program SPP1740

The {FeNO}^{7}(S = 3/2) compounds with aminecarboxylato co-ligands are model compounds in the SPP1740 priority program, which deals with the "influence of local transport processes in chemical reactions in bubble flows". Raman measurements in collaboration with Dr. Günter Rinke and Dipl. Ing. Daniela Schurr[117,118] at the Karlsruhe Institute of Technology revealed an intense resonance-Raman active Fe–N(O) vibration band at around 500 cm^{-1}. Resonance enhancement of the $\tilde{\nu}$(Fe–NO) stretching mode in quartet-{FeNO}^{7} compounds is also known in literature.[62,79,155–157] The resonance-Raman signal of the Fe–NO-stretching vibration band of complex **4** at 494 cm^{-1}**,** obtained with 488 nm laser excitation, agrees perfectly with the $\tilde{\nu}$(Fe–NO) mode at 496 cm^{-1} that is known for the Fe/edta/NO species in the literature.[62,79] The mass transport of a free rising NO bubble in an Fe^{II} hedtra precursor solution was visualized with a tomographic camera set up in collaboration with M.Sc. Katharina Haase and Prof. Dr. Christian Kähler[119] at the Institute of Fluidmechanics and Aerodynamics of the *Bundeswehr* University Munich. The Fe/hedtra/NO reaction system was used because of the good water solubility of the hedtra co-ligand and the high stability of the resulting nitrosyl complex. Nonetheless, according to van Eldik's studies, a high stability of the nitrosyl species is correlated to a high oxygen sensitivity of the Fe^{II} aminecarboxylate precursor complex.[87] As evident from chapter 3.2, the stability of the aqueous nitrosyl complexes can be varied by different aminecarboxylato co-ligands. Establishing a correlation between the complex stability and the structure of the nitrosyl-iron compounds has long been hampered because of the lack of structural information on these species. The X-ray results of this thesis contribute to a better understanding of the characteristics of solution chemistry. The structure information of this thesis gives rise to new aminecarboylato co-ligands that can support favored NO-binding. An optimal aminecarboxylato co-ligand causes a stable nitrosyl complex and a minimal oxygen sensitivity of the precursor species. With the awareness that the coordination number of multidentate ligands, edta for example, changes from seven to six on NO-binding, potentially heptadentate, bis-hemilabile chelators can be tailored for future research and engineering collaborations.

4 Summary

The focus of this thesis is on the crystallization and the description of the molecular structures as well as the quantum-chemical analysis of octahedrally coordinated {FeNO}^{7}(*S* = 3/2) complexes. Based on several publications by the van Eldik group[86–90], the authors reported thermodynamic, kinetic and spectroscopic studies on aqueous {FeNO}^{7}(*S* = 3/2) complexes with aminecarboxylato co-ligands, M. Wolf of the Klüfers group succeeded in crystallizing several compounds of that kind. They were the first quartet-{FeNO}^{7} complexes to be crystallized from an aqueous solution.[4,115] In accordance with van Eldik's studies, the complexes rank among a less-stable subclass of quartet-{FeNO}^{7} compounds with aminecarboxylates. Their aqueous reaction solutions lose nitric oxide when stripped with inert gas or when subjected to low pressure within a short period of time. So far, structural information on the stable subclass of {FeNO}^{7}(*S* = 3/2) compounds with aminecarboxylates has not been available. An important representative beyond this subclass is the hitherto not crystallographically characterized Fe/edta/NO complex, whose application in flue-gas cleaning processes has recently been reported in several studies.[48–57]

Four new crystalline {FeNO}^{7}(*S* = 3/2) complexes with the multidentate co-ligands edda, nta, bhedda and edta were synthesized and analyzed by X-ray diffraction: the hemihydrate complex [Fe(edda)(H_2O)(NO)] · ½ H_2O (**1b** · ½ H_2O), the solvent-free complex [Fe(bhedda)(NO)] (**3**) and the two coordination polymers $[Fe(H_2O)_4(\mathbf{2})_2]_{n/n}$ · 2 H_2O and $[Fe(H_2O)_2(\mathbf{4})_2]_{n/n}$ with $[Fe(NO)(nta)]^-$ (**2**) and $[Fe(Hedta)(NO)]^-$ (**4**) monoanions as the nitrosyl-containing building blocks. All of these complexes belong to the stable subclass of van Eldik's studies. Their aqueous reaction solutions are stable against NO loss upon stripping with inert gas or upon the application of vacuum. The crystallization processes lasted from two weeks for the solvent-free complex [Fe(bhedda)(NO)] (**3**) to one year for the coordination polymer with $[Fe(NO)(nta)]^-$ (**2**) monoanions. Both coordination polymers contain bridging dicationic $[Fe(H_2O)_{4/2}]^{2+}$ moieties instead of the attempted counterions. These unusual structure motifs were attributed to the ability of the bridging $[Fe(H_2O)_{4/2}]^{2+}$ units to form a strong three-dimensional hydrogen-bond pattern in the crystal structure of the coordination polymers.

Comparison of the molecular structures of all currently available crystalline quartet-{FeNO}^{7} compounds with aminecarboxylates revealed one common structural feature, namely the octahedral coordination of the iron center. This became particularly evident in the molecular structure of the monoanionic building unit $[Fe(Hedta)(NO)]^-$ (**4**) (Figure 4.1). Even though the edta co-ligand is a strong hexadentate chelating agent, an octahedrally coordinated nitrosyl-iron complex with a dangled protonated carboxymethyl function was formed. Keeping in mind the sevenfold-coordinated precursor compound $[Fe^{II}(edta)(H_2O)]^{2-}$,[150,153,154] the NO-binding required the coordination number of the iron atom to decrease. In all crystalline quartet-{FeNO}^{7} complexes with aminecarboxylates, the equatorial donor atoms are tilted away from the nitrosyl group, resulting in an average O–N–Fe–X torsion angle of about 100° (with X = the four donor atoms in the equatorial plane normal to the NO ligand). This sterically demanding behavior of the NO ligand clarified the most stable Fe–NO linkage for the hedtra co-ligand in van Eldik's studies.[86–89] With its hydroxyethyl group, the potential hexadentate hedtra ligand

possesses a hemilabile function that can bend away from the iron center to provide a free coordination site for the sterically demanding NO ligand.

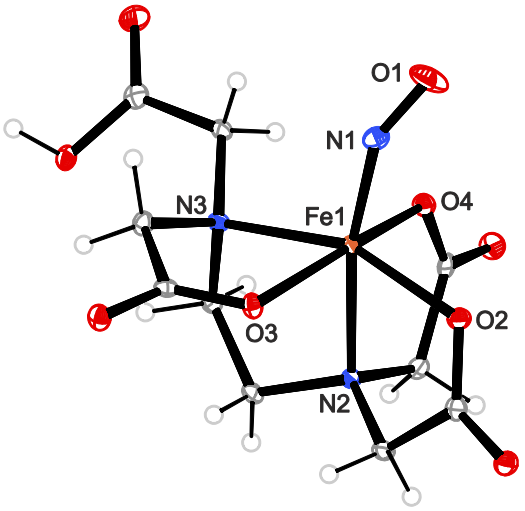

Figure 4.1: Monoanionic building block $[Fe(Hedta)(NO)]^-$ (**4**) of the complex polymer $[Fe(H_2O)_2(\mathbf{4})_2]_{n/n}$.

The $\{FeNO\}^7$ (S = 3/2) complexes were further analyzed with quantum-chemical calculations, based on DFT, in order to get insight into their electronic configuration, to evaluate possible differences between the stable and the less stable complexes and to analyze structural peculiarities. The DFT results, in association with the X-ray results, were expected to contribute to an understanding of the observed stability differences. It was, however, demonstrated that both the experimental and the DFT-optimized structural data of the stable and the less-stable complexes are the same with regard to bond distances and bond angles. An analysis of the electronic structure in terms of the relevant canonical molecular orbitals, broken symmetry calculations, AO-Mix CDA analyses and population analyses indicated the same bonding situation as for the less stable $\{FeNO\}^7$ (S = 3/2) compounds with aminecarboxylato co-ligands: the electronic configuration is best described as an intermediate between $Fe^{II}(NO)$ and $Fe^{III}(NO^-)$ with strong antiferromagnetic coupling between the iron center and the NO ligand and largely covalent Fe–NO π bonds within the β-spin manifold. A closer look at the structural parameters of the corresponding nitrosyl-free Fe^{II} and Fe^{III} complexes revealed that a higher stability of the Fe–NO linkage is associated with a significant admixture of the ferric $Fe^{III}(NO^-)$ mesomer. The instability towards NO loss upon stripping with inert gas was related to the higher amount of the unstable $[Fe(H_2O)_5(NO)]^{2+}$ ion in the aqueous solution equilibria. It was concluded that these two criteria, an adequate stability constant K_{NO} to ensure only minor quantities of the unstable $[Fe(H_2O)_5(NO)]^{2+}$ species in the reaction medium as well as a considerable weight of the ferric $Fe^{III}(NO^-)$ part, have to be satisfied for a stable nitrosyl complex.

With the molecular-structure analyses of this thesis, a special feature of $\{FeNO\}^7$ (S = 3/2) complexes with aminecarboxylato co-ligands became apparent (see Figure 4.2). The NO ligand is tilted towards the oxygen atom of a carboxylate group that is perpendicular to the basal plane of the coordination octahedron (the plane normal to the NO ligand). This structural feature is due to a marginal bonding

interaction between the carboxylate-oxygen atom and the nitrosyl-oxygen atom of the NO group. The bonding overlap responsible for the NO tilt can be seen in the β-HOMO of the DFT-optimized complexes.

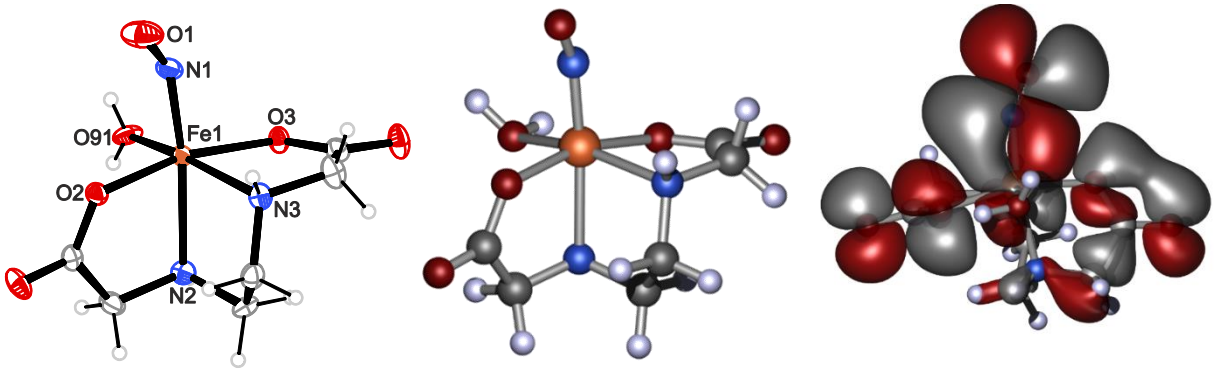

Figure 4.2: The tilt of the NO group to the oxygen donor atom of the carboxylate function that is perpendicular to the basal plane of the coordination octahedron. Left: ORTEP plot of the molecular structure of [Fe(edda)(H_2O)(NO)] (**1b**) in crystals of **1b** · ½ H_2O, middle: the TPSSh/def2-TZVP-optimized structure of **1b,** right: β-HOMO of **1b** (TPSSh/def2-TZVP, isovalue 0.008).

The X-ray analyses of the {FeNO}^{7}(*S* = 3/2) complexes described in this thesis revealed another structural particularity: the thermal ellipsoids of their nitrosyl−oxygen atoms are uncommonly small for {FeNO}^{7}(*S* = 3/2) complexes.[4,46] An examination of the direct environment of the NO ligand in the crystal structures of the complexes showed neither an intermolecular interaction nor a specific crystal-packing pattern as being responsible for this small vibrational ellipsoid. Moreover, the energetic scan of the Fe–N–O bond angle resulted in a weak Fe–N–O bending potential, which proved that the normal shape of the nitrosyl-oxygen atoms' ellipsoid is not due to electronic effects either. Unfortunately, it was not possible to provide a satisfying explanation for this structural peculiarity.

As part of a DFG priority program, the Fe–NO reaction system was investigated in two collaborations with engineering research groups.[117–119] Raman measurements at the Karlsruhe Institute of Technology revealed an intense resonance-Raman active Fe–N(O) vibration band at around 500 cm^{-1} for the quartet-{FeNO}^{7} complexes. Furthermore, the mass transport of a free rising NO bubble in an iron(II) precursor solution was visualized with a tomographic camera set up at the Institute of Fluid Dynamics and Aerodynamics of the *Universität der Bundeswehr München.*

To conclude, the results of this thesis contribute to an enhanced understanding of the solution chemistry of {FeNO}^{7}(*S* = 3/2) compounds with aminecarboxylates. The stability rules for the aqueous complexes, as described by the van Eldik group about fifteen years ago, have become comprehensible by means of single-crystal X-ray analysis and computational chemistry. The structure information of this thesis gives rise to new aminecarboylato co-ligands that can support favored NO-binding. With the finding that the coordination number of the edta co-ligand changes from seven to six on NO-binding, potentially heptadentate, bis-hemilabile chelators can be tailored for future research and engineering collaborations.

5 Experimental Part

5.1 Common working techniques

Due to the possible oxidation of the $\{FeNO\}^7$(S = 3/2) compounds and the iron(II) aminecarboxylate complexes, all experiments were carried out under strict exclusion of oxygen from air using standard Schlenk techniques with argon or nitrogen as the inert gas. Before usage, all reaction flasks were evacuated and filled with argon three times in order to remove oxygen. Solvents were deaerated with argon before usage. For this purpose, the solvents were transferred under an argon stream in pre-evacuated Schlenk flasks and degassed by a continuous argon flow (15 min per 100 mL volume). The deaerated solvents were then stored under an argon atmosphere. The syringes and cannulas that were used to transfer reagents and solvents, were purged three times with argon before usage.

To enable the crystallization of the $\{FeNO\}^7$(S = 3/2) complexes, the principle of isothermal diffusion was utilized. In this context, a two-chamber Schlenk flask was constructed by integrating a test tube into a conventional Schlenk tube. The reaction partners were dissolved inside the test tube while a suitable solvent with less polarity was added outside to diffuse into the reaction solution.

The experimental set-up of the NO apparatus is shown in Figure 5.1. Nitric oxide was purged with a 4 M sodium hydroxide solution before passing it through the reaction flask to exclude higher oxidized NO_x species and polymers. Excess NO gas was converted to N_2 with a 2 M amidosulfuric acid solution. The apparatus was flushed with argon (10 min) before and after the reaction with gaseous NO in order to eliminate oxygen and NO_x residues.

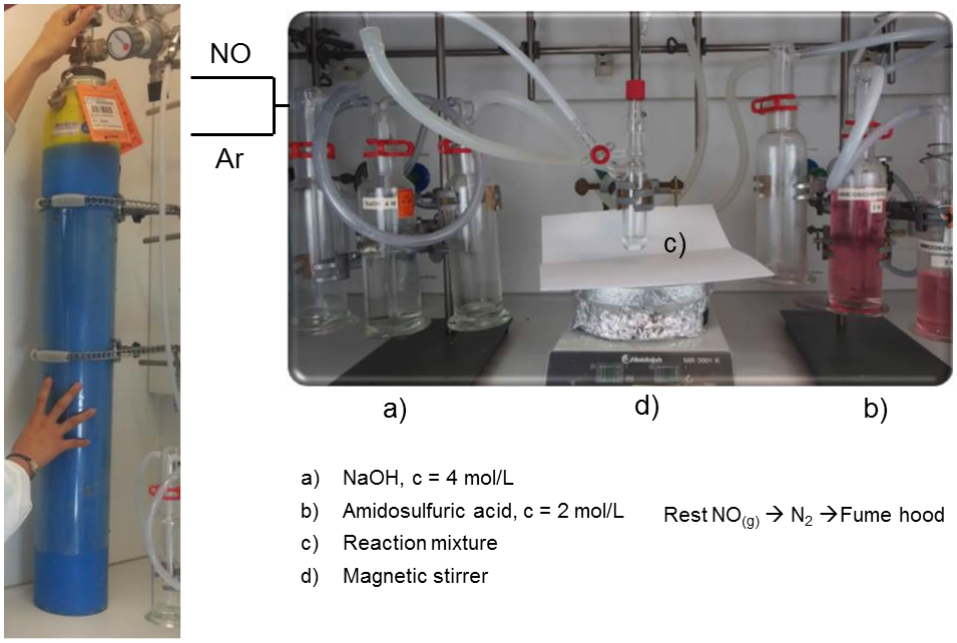

Figure 5.1: Experimental set-up of the NO apparatus. The pH indicator methyl orange was added to the 2 M amidosulfuric acid solution.

5.2 Analytical methods

5.2.1 NMR spectroscopy

The $^{13}C\{^{1}H\}$-NMR spectrum of the K_2bhedda reaction solution was recorded with a resonance frequency of 100 MHz on a Jeol Eclipse 400 spectrometer. The measurement was carried out at room temperature (ca. 24°C) in a 5 mm tube. The chemical shift δ is given in ppm. The spectrum was recorded broadband proton decoupled and interpreted using the software MESTRENOVA.[158]

5.2.2 Mass spectrometry

The FAB spectra were measured on a Jeol MStation 700. The samples were ionized in a nitrobenzylalcohol or glycerine matrix, using 8 kV fast argon atoms.

5.2.3 Elemental analysis

The CHN analyses were recorded on an Elementar vario micro cube instrument.

5.2.4 IR spectroscopy

IR spectra were recorded on a Jasco FT/IR-460 Plus spectrometer. Because of the strong absorption band of water in the region of the characteristic NO stretching vibration, IR spectra of the dissolved complexes were recorded in D_2O. Solid samples were measured with an ATR diamond plate, solutions were recorded with a CaF_2 measuring cell or an ATR diamond plate. Solid samples were recorded from 400 cm^{-1} to 4000 cm^{-1}, solutions from 1300 cm^{-1} to 2000 cm^{-1}. The intensity of the vibration bands is given in parenthesis behind the wavenumber. The spectra were interpreted with the software SPECTRA MANAGER 2.[159] They were plotted with the program package ORIGIN PRO for visual presentation.[160] All signals are given in wavenumbers (cm^{-1}).

5.2.5 Raman spectroscopy

Raman spectra were recorded at the Institute for Microprocess Engineering of the Karlsruhe Institute of Technology on a self-constructed spectrometer.[117,118] The measurements were performed in silica glass cuvettes with a thickness of 1 cm using the 488 nm excitation wavelength from a continuous emitting argon-ion laser. The spectra were recorded from 0 cm^{-1} to 4000 cm^{-1} and plotted with the program package ORIGIN PRO for visual presentation.[160]

5.2.6 UV/Vis spectroscopy

UV/VIS spectra in solution were measured on a Cary 50 Conc UV-Visible-Spectrophotometer in silica glass cuvettes with a thickness of 1 cm. Solid samples were measured on a Cary 500 Scan UV-Vis-IR-

Spectrophotometer with a Labsphere DRA-CA-5500 photometer sphere. The diffuse reflectance spectra of the UV/Vis spectrometer were converted into absorption data by using the Kubelka-Munk function:[121]

$$f(R) = \frac{(1-R)^2}{2R} = \frac{K}{S} \tag{5.1}$$

R is the relative reflectivity of an infinitely thick layer, *K* is the absorption coefficient and *S* is the scattering coefficient. The spectra were recorded from 300 nm to 800 nm and plotted with the program package ORIGIN PRO for visual presentation.[160]

5.2.7 X-ray diffraction

Crystals suitable for single-crystal X-ray diffraction analysis were selected by using a Leica MZ6 polarization microscope. The measurements were performed at 173 K on single crystal diffractometers of the types Bruker D8 Quest and Bruker D8 Venture using MoK_α irradiation (λ = 0.71073 Å). The structures were solved by direct methods using SHELXS2014[161] and refined by full-matrix, least-squares calculations on F^2 (SHELXL2014[162]). Non-hydrogen atoms were initially located and later refined anisotropically, hydrogen atoms were refined isotropically. C–H bonds and the corresponding angles were idealized. SHELXLE (version 7.25)[163] was used as graphical user interface. Intermolecular contacts were analyzed with the program package MERCURY.[164,165] Visualization was performed with ORTEP[166] and SCHAKAL[167]. Further informations on the structures are listed in tabular form in the APPENDIX. The values given there are described as follows:

$$R_{\mathrm{int}} = \frac{\sum |F_{\mathrm{o}}^2 - \langle F_{\mathrm{o}}^2 \rangle|}{\sum F_{\mathrm{o}}^2} \tag{5.2}$$

$$R(F) = \frac{\sum \big||F_o| - |F_{\mathrm{c}}|\big|}{\sum |F_{\mathrm{o}}|} \tag{5.3}$$

$$wR(F^2) = \sqrt{\frac{\sum w(F_{\mathrm{o}}^2 - F_{\mathrm{c}}^2)^2}{\sum w(F_{\mathrm{o}}^2)^2}} \tag{5.4}$$

$$S = \sqrt{\sum \frac{w(F_{\mathrm{o}}^2 - F_{\mathrm{c}}^2)^2}{N_{\mathrm{hkl}} - N_{\mathrm{Parameter}}}} \tag{5.5}$$

The weighting factors *ω* and *P* are defined as:

$$\omega = \frac{1}{\sigma^2(f_o^2) + (xP)^2 + yP} \text{ with } P = \frac{\max(F_o^2, 0) + 2F_c^2}{3} \tag{5.6}$$

In analogy to SHELXL-97, the values of the parameters *x* and *y* were adopted to minimize the variance of $w(F_c^2/F_0^2)^2$ for several (intensity-ordered) groups of reflexes.
The coefficient U_{eq} is defined as follows:

$$U_{eq} = \frac{1}{3}\sum_{i=1}^{3}\sum_{j=1}^{3} U_{ij} a_i a_j a_i^* a_j^* \tag{5.7}$$

5.3 Reagents and solvents

Table 5.1: Chemicals used, their purity and their manufacturers.

Chemical	Manufacturer (Purity)
1,10-phenanthroline	Merck (≥99.0%)
1,4-dioxane	Sigma-Aldrich (≥99.5%)
2,2′-bipyridyl	Alfa Aesar (98%)
acetone	Sigma-Aldrich (≥99.5%)
acetonitrile	VWR Chemicals (≥99.5%)
acetylacetone	Sigma-Aldrich (≥99%)
amidosulfuric acid	ApplChem (>99%)
benzyltrimethylammonium hydroxide solution [a]	Sigma-Aldrich
bis(triphenylphosphine)iminium chloride	ABCR (97%)
bromoacetic acid	Fluka (97%)
cesium hydroxide monohydrate	Acros (99.95%)
choline hydroxide solution [b]	TCI
deuterium oxide	Euriso-Top (99.9%)
D-histidine	Alfa Aesar Fluka (99%)
diethylenetriaminepentaacetic acid	Sigma Aldrich (≥98%)
diethylether	Bernd Kraft (≥99.5%)
DL-aspartate	Fluka (≥99%)
DL-serine	Fluka (≥99%)
D-threonine	Merk (≥99%)
iron(II) triflate	[c]

ethanol, abs.	Sigma-Aldrich (>99.5%)
ethylenediamine-*N,N,N′,N′*- tetraacetatic acid	Fluka (>99%)
ethylenediamine-*N,N′*-diacetic acid	Sigma-Aldrich (98%)
ethylenediamine-*N*,*N′*-disuccinic acid trisodium salt solution [d]	Sigma-Aldrich
glycine	Sigma-Aldrich (>99%)
iron(II) sulfate heptahydrate	Merk (99.9%)
L-aspartate	Fluka (≥99.5%)
L-cysteine	Acros Organics (>99%)
L-histidine	Fluka (≥99.0%)
lithium hydroxide monohydrate	Fluka (≥98.0%)
L-leucine	Fluka (≥99.5%)
L-phenylalanine	Acros Organics (>98.5%)
L-serine	Acros Organics (99%)
L-threonine	Acros Organics (≥98%)
L-tyrosine	Sigma-Aldrich Fluka (≥98%)
magnesium sulfate	Grüssing (99%)
methanol	Fluka (99.8%)
N-(2-hydroxyethyl)ethylenediamine-*N,N′,N′*-triacetic acid	Aldrich (98%)
N,*N*,*N′*,*N′*-tetramethylethylenediamine	Sigma-Aldrich (99.5%)
N,N′-bis(2-hydroxyethyl)-*N,N′*-ethylenediamine	Sigma-Aldrich (97%)
N,N-dimethylformamide	Fluka (≥99.5%)
n-hexane	Grüssing (95%)
nitric oxide	Air Liquide
nitrilotriacetic acid	Fluka (>99%)
n-pentane	VWR Chemicals (99.9%)
potassium hydroxide	Sigma-Aldrich (99.99%)
rubidium hydroxide hydrate	Aldrich
sodium hydroxide	Fluka (≥99.5%)
tetrasodium *N*,*N*-bis(carboxymethyl)-L-glutamate solution [e]	TCI
triethylamine	RiedeldeHaen (99%)
water	in-house system

[a] 50 wt.% in H_2O. [b] 49 wt.% in H_2O. [c] Synthesized according to Reference [168]. [d] 35 wt.% in H_2O. [e] 40 wt.% in H_2O.

5.4 Synthesis of iron(II) aminecarboxylates

5.4.1 $[Fe^{II}(edda)(H_2O)_2]$ (**5b**)

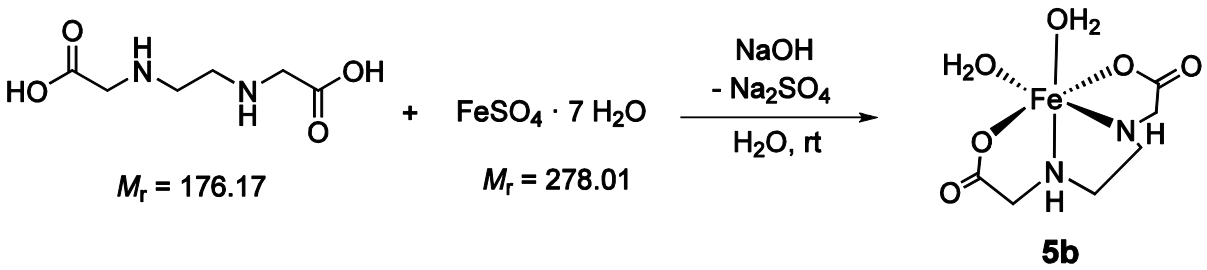

M_r = 176.17 M_r = 278.01

5b

Starting material: Ethylenediamine-*N*,*N*′-diacetic acid (H_2edda), iron(II) sulfate heptahydrate, sodium hydroxide, water, acetone.

Procedure: Sodium hydroxide (0.013 g, 0.32 mmol) was added to a suspension of H_2edda (0.028 g, 0.16 mmol) in distilled water (0.75 mL). After stirring the colorless solution for 30 min at room temperature, $FeSO_4 \cdot 7H_2O$ (0.044 g, 0.16 mmol) was added to it in portions. The slightly green solution was stored at room temperature under an argon atmosphere, and over one week, acetone (0.75 mL) was diffused into the reaction solution. $[Fe^{II}(edda)(H_2O)_2]$ (**5b**) was isolated in the form of colorless needle-shaped crystals.

Yield: 0.031 g (0.12 mmol, 72%).

Empirical formula: $C_6H_{14}FeN_2O_6$ (266.04 g mol^{-1}, **5b**).

IR (crystal, ATR): $\tilde{\nu}$/cm^{-1}: 3330(s), 3258(s), 2966(s), 2942(m), 2361(vw), 1978(vw), 1681(s, $\nu_{C=O}$), 1575(vs, $\nu_{as\ COO}$), 1558(vs), 1489(m), 1436(m), 1389(s, $\nu_{s\ COO}$), 1333(w), 1316(w), 1303(vs), 1283(w), 1255(w), 1141(m), 1098(m), 1050(m), 1006(s), 983(w), 943(s), 914(m), 899(m), 854(w), 831(w), 701(s), 687(s), 661(m).

Elemental analysis: (calcd. for $C_6H_{14}FeN_2O_6 \cdot 0.25\ H_2O$**,** 270.54 g mol^{-1}), found (calcd.): %: C 26.81 (26.64), H 5.60 (5.40), N 10.32 (10.35).

X-ray structure analysis: uv436.

5.4.2 $[Fe^{II}(bhedda)] \cdot H_2O$ (**6** · H_2O)

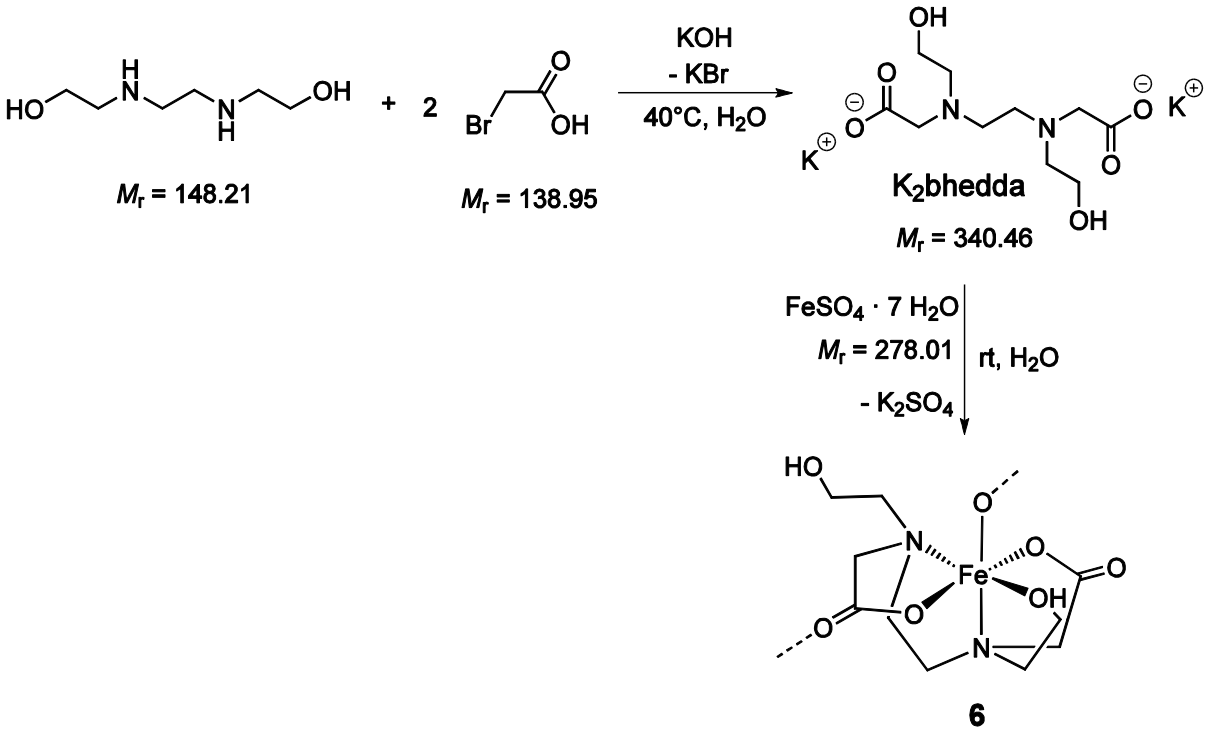

According to T. G. Wensel, C. F. Meares, *Biochemistry* **1983**, *22*, 6247–6254.

Starting materials: *N,N′*-bis(2-hydroxyethyl)-*N,N′*-ethylenediamine, bromoacetic acid, potassium hydroxide, iron(II) sulfate heptahydrate, water, acetone.

Procedure: *N*,*N′*-bis(2-hydroxyethyl)ethylenediamine-*N*,*N′*-diacetate dipotassium salt (K_2bhedda) was synthesized by following a published procedure by Wensel and Meares[120] under an nitrogen atmosphere. *N,N′*-bis(2-hydroxyethyl)-*N,N′*-ethylenediamine (2.67 g, 18.0 mmol) was dissolved in distilled water (8 mL). The solution was cooled with an ice bath, and bromoacetic acid (5.02 g, 36.0 mmol) was added in portions while stirring. During the addition of bromoacetic acid, the pH value of the mixture was kept at 11 with aqueous potassium hydroxide solution (7 M). The resulting mixture was stirred at 40°C for 60 h, whereby the pH value was still maintained at 10–11. The colorless reaction solution was treated with $FeSO_4 \cdot 7H_2O$ (5.00 g, 18.0 mmol) to form the $[Fe^{II}(bhedda)]$ complex (**6**). The colorless solid that precipitated was filtered from the slightly green reaction solution and dried in vacuum to give a colorless solid containing the $[Fe^{II}(bhedda)]$ complex. The colorless raw product (0.318 g, ≈1.00 mmol) was dissolved in water (3 mL) and over two weeks, acetone (3 mL) was diffused into the reaction solution. $[Fe^{II}(bhedda)] \cdot H_2O$ crystallized as colorless needle-shaped crystals, suitable for X-ray crystallography.

Yield: Raw product: 1.26 g (≈ 3.96 mmol, ≈ 22%), crystals: 0.174 g (0.518 mmol, ≈ 52%).

Empirical formula: $C_{10}H_{20}FeN_2O_7$ (336.13 g mol^{-1}; **6** · H_2O).

$^{13}C\{^{1}H\}$-NMR (raw solution before the treatment with $FeSO_4 \cdot 7H_2O$, 100 MHz, H_2O): *δ*/ppm: 179.7, 178.9, 176.4 (-<u>C</u>OO), 169.6, 169.2, 162.2, 61.6, 58.1 (OOC-<u>C</u>H_2-N), 57.4 (N-<u>C</u>H_2-CH_2-OH), 56.6 (N-CH_2-<u>C</u>H_2-OH), 55.9, 51.6 (N-<u>C</u>H_2-<u>C</u>H_2-N), 48.6, 46.5, 41.7.

MS (raw product, FAB^+, *M* = [Fe^{II}(bhedda)] ($C_{10}H_{18}FeN_2O_6$), 318.05 g mol^{-1}): *m/z* = 319.2 $[M+H]^+$.

MS (raw product, FAB^-, *M* = [Fe^{II}(bhedda)] ($C_{10}H_{18}FeN_2O_6$), 318.05 g mol^{-1}): *m/z* = 317.2 $[M-H]^-$.

IR (crystal, ATR): $\tilde{\nu}$/cm^{-1}: 2860(m), 2348(w), 2192(vw), 2158(vw), 1698(s, $\nu_{C=O}$), 1582(s, $\nu_{as\ COO}$), 1462(vw), 1427(w), 1402(s, $\nu_{s\ COO}$), 1373(m), 1310(w), 1237(w), 1237(m), 1098(vs, ν_{C-OH}), 983(m), 970(m), 938(w), 905(w), 878(w), 825(w), 762(w), 738(m), 732(w), 668(w).

Elemental analysis (crystal, calcd. for $C_{10}H_{20}FeN_2O_7 \cdot 0.1\ H_2O$, 337.85 g mol^{-1}), found (calcd.):%: C 35.53 (35.54), H 6.06 (6.03), N 8.30 (8.29).

X-ray structure analysis: uv207.

5.4.3 $[Fe^{II}(Hhedtra)] \cdot H_2O$ (**7** · H_2O)

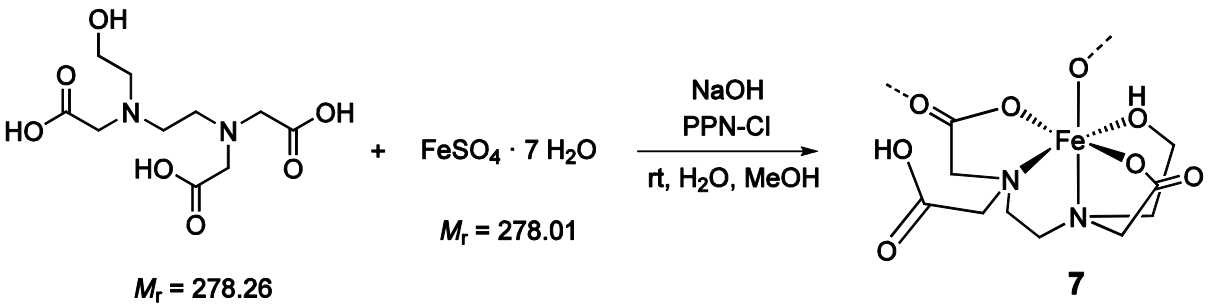

M_r = 278.26

Starting materials: *N*-(2-hydroxyethyl)ethylenediamine-*N,N′,N′*-triacetic acid (H_3hedtra), sodium hydroxide, iron(II) sulfate heptahydrate, water, bis(triphenylphosphine)iminium chloride, methanol.

Procedure: Sodium hydroxide (0.600 g, 15.0 mmol) was added to a suspension of H_3hedtra (2.80 g, 10.0 mmol) in distilled water (15 mL). Bis(triphenylphosphine)iminium chloride (0.290 g, 0.500 mmol) and methanol (5 mL) were added under stirring conditions in order to improve the crystallization tendency of the reaction product. $FeSO_4 \cdot 7H_2O$ (2.80 g, 10.0 mmol) was added in portions, whereupon a slightly green solution resulted. The precipitated colorless solid was filtered from the reaction solution, washed with methanol (ca. 10 mL) and dried *in vacuo.* To enable crystallization, the colorless solid (0.315 g) was heated under reflux in water (15 mL). The reaction flask was immediately transferred to a dewar vessel that was filled with boiling water, and cooled to room temperature within 24 hours. $[Fe(Hhedtra)] \cdot H_2O$ (**7** · H_2O) crystallized as colorless rods.

Yield: Raw product: 0.462 g, crystals: 0.138 g (0.394 mmol).

Empirical formula: $C_{10}H_{18}FeN_2O_8$ (350.11 g mol^{-1}, **7** · H_2O).

MS (raw product, FAB$^-$, $[Fe^{II}(hedtra)]^-$, 331.08 g mol^{-1}): *m/z* = 331.3 $[C_{10}H_{15}FeN_2O_7]^-$.

MS (raw product, FAB$^+$, PPN$^+$, 538.58 g mol^{-1}): *m/z* = 538.6 $[C_{36}H_{30}NP_2]^+$.

IR (crystal, ATR): $\tilde{\nu}$/cm^{-1}: 3412(vw), 2921(vw), 2854(vw), 1725(w), 1580(s, $\nu_{as\ COO}$), 1432(w), 1400(m, $\nu_{s\ COO}$), 1297(m), 1223(m), 1170(m), 1103(m), 1082(m), 993(w), 933(w), 880(w), 827(w), 802(w), 760(w), 724(w), 699(w).

Elemental analysis (crystal, calcd. for $C_{10}H_{18}FeN_2O_8 \cdot 0.35\ H_2O$**,** 356.41 g mol^{-1}), found (calcd.):%: C 33.84 (33.53), H 5.67 (5.32), N 7.63 (7.82).

X-ray structure analysis: sv252.

5.5 Synthesis of {FeNO}^{7}(*S* = 3/2) complexes with aminecarboxylates

5.5.1 [Fe(edda)(H_2O)(NO)] · ½ H_2O (**1b** · ½ H_2O)

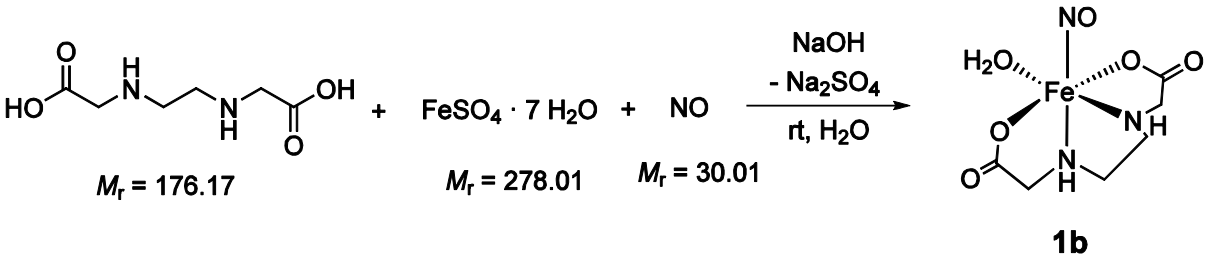

1b

Starting material: Ethylenediamine-*N*,*N*′-diacetic acid (H_2edda), iron(II) sulfate heptahydrate, sodium hydroxide, nitric oxide, water, acetone.

Procedure: Sodium hydroxide (0.100 g, 2.50 mmol) was added to a suspension of H_2edda (0.220 g, 1.25 mmol) in distilled water (4 mL). The mixture was stirred for 30 min at room temperature. $FeSO_4 \cdot 7H_2O$ (0.278 g, 1.00 mmol) was added in portions, and a slightly green solution resulted. The solution was treated with gaseous nitric oxide for ten minutes, whereupon a color change to green-black was observed after two minutes. The green-black solution was stored at room temperature under an NO atmosphere, and over three weeks, acetone (4 mL) was diffused into the reaction solution. [Fe(edda)(H_2O)(NO)] · ½ H_2O was isolated in the form of black crystals.

Yield: 0.121 g (0.421 mmol, 42%).

Empirical formula: $C_6H_{13}FeN_3O_{6.50}$ (287.04 g mol^{-1}, **1b** · ½ H_2O).

IR (crystal, ATR): $\tilde{\nu}$/cm^{-1}: 2360(vs), 2341(vs), 1761(m, ν_{NO}), 1589(s, $\nu_{as\,COO}$), 1457(w), 1417(w), 1376(m, $\nu_{s\,COO}$), 1339(m), 1306(w), 1282(vw), 1248(vw), 1213(vw), 1141(w), 1117(vw), 1075(vw), 1016(w), 958(m), 913(w).

IR (reaction solution, D_2O, measuring cell with CaF_2 panels): $\tilde{\nu}$/cm^{-1}: 1769(s, ν_{NO}), 1599(vs, $\nu_{as\,COO}$), 1462(vs), 1389(vs, $\nu_{s\,COO}$), 1320(s), 1291(w).

UV/Vis (crystal): λ/nm: 414 (CT), 430 (CT), 644 (d-d).

UV/Vis (reaction solution, H_2O, 1 mmol L^{-1}): λ/nm: 342 (CT), 435 (CT).

UV/Vis (reaction solution, H_2O, 10 mmol L^{-1}): λ/nm: 617 (d-d).

Raman (reaction solution, H_2O, 62 mmol L^{-1}, laser excitation 488 nm): $\tilde{\nu}$/cm^{-1}: 486 ($\nu_{Fe–NO}$), 1768 (ν_{NO}).

X-ray structure analysis: sq016.

5.5.2 $[\{Fe(H_2O)_4\}\{Fe(NO)(nta)\}_2]_{n/n} \cdot 2\ H_2O = [Fe(H_2O)_4(\mathbf{2})_2]_{n/n} \cdot 2\ H_2O$

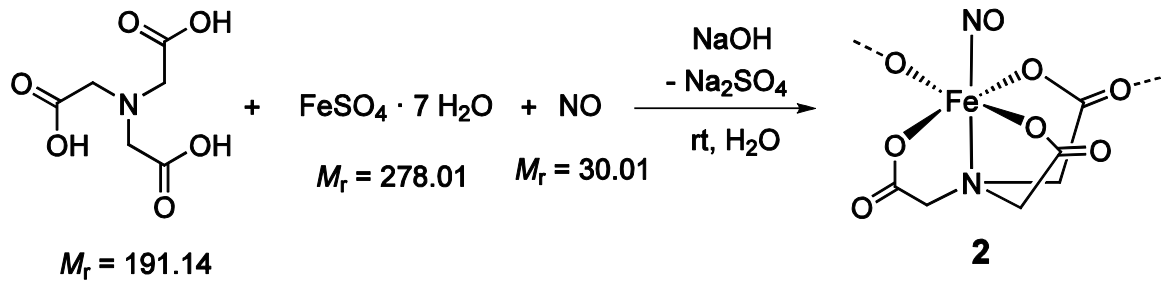

Starting material: Nitrilotriacetatic acid (H_3nta), iron(II) sulfate heptahydrate, nitric oxide, sodium hydroxide, water, acetone, ethanol.

Procedure: Sodium hydroxide (86.0 mg, 2.15 mmol) was added to a suspension of H_3nta (0.194 g, 1.00 mmol) in distilled water (3 mL). After stirring the colorless solution for 30 min at room temperature, $FeSO_4 \cdot 7H_2O$ (0.278 g, 1.00 mmol) was added to it in portions. Nitric oxide was bubbled through the slightly green solution for ten minutes, and a green-black solution resulted. The mixture was stored at room temperature under an NO atmosphere, and over six months, acetone (6 mL) was diffused into the reaction solution. The NO atmosphere was changed to an argon atmosphere, and ethanol (6 mL) was added to diffuse over a further six months into the reaction solution. After a period of one year, $[\{Fe(H_2O)_4\}\{Fe(NO)(nta)\}_2]_{n/n} \cdot 2\ H_2O = [Fe(H_2O)_4(\mathbf{2})_2]_{n/n} \cdot 2\ H_2O$ was isolated in the form of large black crystals suitable for X-ray crystallography.

Yield: 0.173 g, (0.486 mmol, 49%).

Empirical formula: $\{C_6H_{12}Fe_{1.50}N_2O_{10}\}_{n/n}$ (355.95 g mol^{-1}, 0.5 $[\{Fe(H_2O)_4\}\{Fe(NO)(nta)\}_2]_{n/n} \cdot H_2O$ = 0.5 $Fe(H_2O)_4(\mathbf{2})_2]_{n/n} \cdot H_2O$).

IR (crystal, ATR): $\tilde{\nu}$/cm^{-1}: 3222(s), 1791(s, ν_{NO}), 1574(vs, $\nu_{as\ COO}$), 1505(vs), 1459(m), 1317(s, $\nu_{s\ COO}$), 1271(s), 1223(m), 1124(m), 912(w), 736(s).

IR (reaction solution, D_2O, measuring cell with CaF_2 panels): $\tilde{\nu}$/cm^{-1}: 1793(w, ν_{NO}), 1714(s, vs, $\nu_{C=O}$), 1623(vs, $\nu_{as\ COO}$), 1435(s), 1400(vs, $\nu_{s\ COO}$), 1319(m), 1280(m), 1255(m), 1240(w).

UV/Vis (crystal): λ/nm: 433 (CT), 622 (d-d).

UV/Vis (reaction solution, H_2O, 3 mmol L^{-1}): λ/nm: 339 (CT), 439 (CT), 602 (d-d).

X-ray structure analysis: uv073.

5.5.3 [Fe(bhedda)(NO)] (**3**)

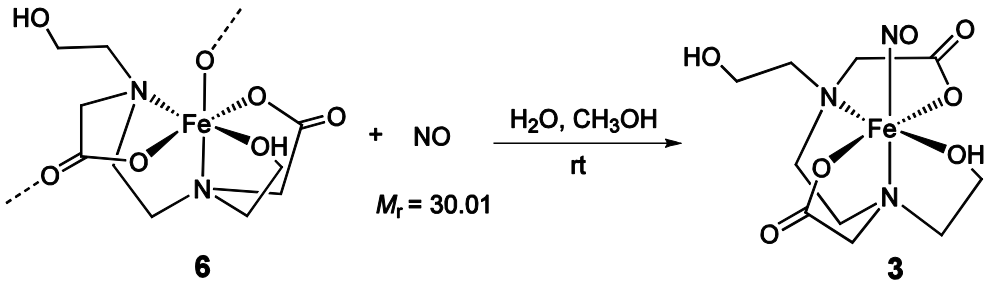

Starting material: (*OC*-6-13)-*N,N'*-bis(2-hydroxyethyl)ethylenediamine-*N,N'*-diacetatoiron(II) (**6**), nitric oxide, water, methanol, acetone.

Procedure: The precipitated colorless solid from chapter 5.4.2 that contains the [Fe^{II}(bhedda)] complex (**6**) was utilized without further purification. The solid (0.300 g, 0.940 mmol) was dissolved in water (3 mL). Gaseous nitric oxide was bubbled through the light-green solution for ten minutes, and, after two minutes, a color change to green-black was observed, indicating the formation of the {FeNO}^{7}(*S* = 3/2) chromophore. All attempts to crystallize [Fe(bhedda)(NO)] from an aqueous solution failed. Instead, the crystallization of the complex succeeded from a methanolic solution. [Fe^{II}(bhedda)] (50.0 mg, 0.157 mmol) was dissolved in methanol (1 mL), and the solution was treated with gaseous nitric oxide. The resulting brown-black reaction solution was stored at room temperature under an NO atmosphere, and acetone (2 mL) was diffused over two weeks into the reaction solution. [Fe(bhedda)(NO)] was isolated as one single black crystal.

Yield: One crystal.

Empirical formula: $C_{10}H_{18}FeN_3O_7$ (348.12, **3**).

IR (crystal): yield too low.

IR (reaction solution, D_2O, measuring cell with CaF_2 panels): $\tilde{\nu}$/cm^{-1}: 1782(m, ν_{NO}), 1620(s, $\nu_{as\ COO}$), 1380(m, $\nu_{s\ COO}$).

UV/Vis (crystal): yield too low.

UV/Vis (reaction solution, H_2O, 3 mmol L^{-1}): λ/nm: 337 (CT), 422 (CT), 650 (d-d).

X-ray structure analysis: tv157.

5.5.4 $[\{Fe(H_2O)_2\}\{Fe(NO)(Hedta)\}_2]_{n/n}$ = $[Fe(H_2O)_2(\mathbf{4})_2]_{n/n}$

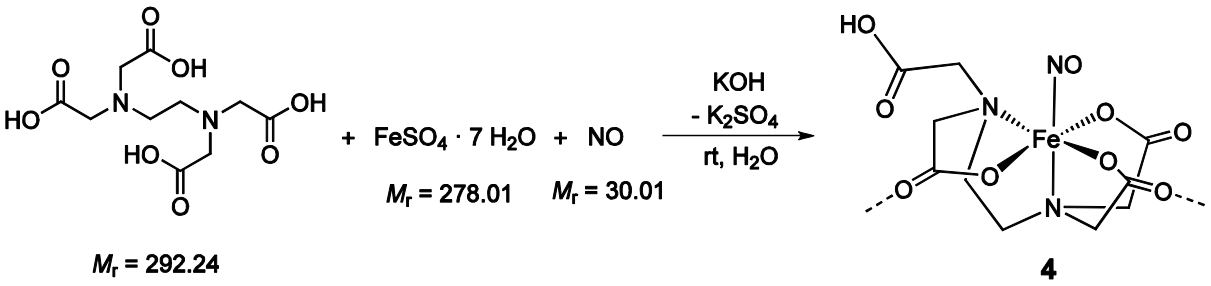

Starting material: Ethylenediamine-*N*,*N*,*N*′,*N*′-tetraacetic acid (H_4edta), iron(II) sulfate heptahydrate, nitric oxide, potassium hydroxide, water, acetone.

Procedure: To H_4edta (0.292 g, 1.00 mmol) in distilled water (3 mL) was added 85% potassium hydroxide (0.187 g, 3.33 mmol), and the colorless solution was stirred for 30 min at room temperature. $FeSO_4 \cdot 7H_2O$ (0.278 g, 1.00 mmol) was added in portions, resulting in a slightly green solution. Gaseous nitric oxide was bubbled through the reaction solution for ten minutes, whereupon after two minutes, the characteristic color change to green-black was observed. The solution was stored at room temperature under an NO atmosphere, and acetone (3 mL) was diffused into the reaction solution over six months. $[\{Fe(H_2O)_2\}\{Fe(NO)(Hedta)\}_2]_{n/n}$ = $[Fe(H_2O)_2(\mathbf{4})_2]_{n/n}$ was isolated in the form of large black crystals.

Yield: 0.347 g (0.824 mmol, 82%).

Empirical formula: $\{C_{10}H_{15}Fe_{1.50}N_3O_{10}\}_{n/n}$ (421.02 g mol^{-1}, 0.5 $[\{Fe(H_2O)_2\}\{Fe(NO)(Hedta)\}_2]_{n/n}$ = 0.5 $[Fe(H_2O)_2(\mathbf{4})_2]_{n/n}$).

IR (crystal, ATR): $\tilde{\nu}$/cm^{-1}: 3255(vw), 2968(vw), 1839(w), 1781(m, ν_{NO}), 1572(s, $\nu_{as\,COO}$), 1440(w), 1370(s, $\nu_{s\,COO}$), 1316(m), 1260(vw), 1215(w), 1168(m), 1102(s), 1024(vw), 1002(w), 979(w), 931(m), 861(w), 800(w), 717(m), 685(m).

IR (reaction solution, D_2O, measuring cell with CaF_2 panels): $\tilde{\nu}$/cm^{-1}: 1777(s, ν_{NO}), 1643(vs, $\nu_{C=O}$), 1592(vs, $\nu_{as\,COO}$), 1466(s), 1439(s), 1403(vs), 1384(vs, $\nu_{s\,COO}$), 1321(m), 1289(w), 1269(m), 1234(s), 1218(s), 1205(s).

UV/Vis (crystal): λ/nm: 432 (CT), 623 (d-d).

UV/Vis (reaction solution, H_2O, 3 mmol L^{-1}): λ/nm: 342 (CT), 435 (CT), 634 (d-d).

Raman (reaction solution, H_2O, 62 mmol L^{-1}, laser excitation 488 nm): $\tilde{\nu}$/cm^{-1}: 494 (ν_{Fe-NO}), 1768 (ν_{NO}).

X-ray structure analysis: tv202.

5.6 Further crystallisation experiments

During the research for this thesis, many attempts were made to obtain crystalline Fe/aminecarboxylate/NO species of the stable subclass according to van Eldik's survey.[87] H_3nta, H_2edda, H_4edta, H_3hedtra, Na_3Hedds, H_5dtpa and Na_4AcGlu were used as commercially available chelating agents. All experiments were carried out in aqueous solution (3–6 mL). Acetone or 1,4-Dioxan[169] (3–6 mL) was added as the antisolvent in order to diffuse into the reaction solution. The aminecarboxylate compound (1.0–1.3 mmol) and one of the bases, lithium hydroxide monohydrate, sodium hydroxide, potassium hydroxide, cesium hydroxide monohydrate, rubidium hydroxide, benzyltrimethylammonium hydroxide or cholin hydroxide (1.0–5.0 mmol in each case) were dissolved in water. After stirring the colorless solution for 30 min at room temperature, iron(II) sulfate heptahydrate (0.28 g, 1.0 mmol) was added to it in portions. The slightly green reaction solution was then treated with gaseous nitric oxide (10 min to 15 min) at room temperature. After a few minutes, the characteristic dark green color of the $\{FeNO\}^7$(S = 3/2) chromophore was observable. Further syntheses were carried out in an analogous procedure, whereas bis(triphenylphosphine)iminium chloride (0.10–0.50 mmol) and methanol (1.5–3 mL) were added in order to improve the crystallization tendency of the nitrosyl complexes. All reaction solutions with pH-values of eight and higher (the pH value was measured after the addition of iron(II) sulfate heptahydrate) adopted a slightly red coloring after about one month, indicating the oxidation of iron(II) to iron(III). The reaction mixtures were stored at room temperature under an NO atmosphere for six months. Afterwards, the NO atmosphere was changed to an argon atmosphere and ethanol (6 mL) was added as an additional antisolvent. As the reaction solutions were stable against NO loss upon being subjected to low pressure, the mixtures were concentrated by the slow evaporation of the solvent *in vacuo* in order to induce crystallization. Over a period of one to three years, no crystalline products were obtained.

Because of the strong absorption band of water in the region of the characteristic NO stretching vibration, IR spectra of the dissolved complexes were recorded in D_2O. All syntheses were repeated in up-scaled amounts using D_2O instead of H_2O as the solvent. The different reaction conditions did not affect the NO stretching vibration bands or the UV/Vis absorption bands of the reaction solutions. The spectroscopic data of the Fe/hedtra/NO, Fe/edds/NO and the Fe/dtpa/NO species agreed perfectly with those reported by the van Eldik group.[87] The IR and UV/Vis data of the Fe/AcGlu/NO species are not known in literature.

Fe/hedtra/NO

IR (reaction solution, D_2O, measuring cell with CaF_2 panels): $\tilde{\nu}$/cm^{-1}: 1776(s, ν_{NO}).

UV/Vis (reaction solution, H_2O, 3 mmol L^{-1}): λ/nm: 342 (CT), 433 (CT), 635 (d-d-transition).

Fe/edds/NO

IR (reaction solution, D_2O, ATR): $\tilde{\nu}$/cm^{-1}: 1763(s, ν_{NO}).

UV/Vis (reaction solution, H_2O, 3 mmol L^{-1}): λ/nm: 342 (CT), 440 (CT), 636 (d-d-transition).

Fe/dtpa/NO

IR (reaction solution, D_2O, ATR): $\tilde{\nu}$/cm^{-1}: 1773(s, ν_{NO}).

UV/Vis (reaction solution, H_2O, 3 mmol L^{-1}): λ/nm: 433 (CT), 636 (d-d-transition).

Fe/AcGlu/NO

IR (reaction solution, D_2O, ATR): $\tilde{\nu}$/cm^{-1}: 1791(s, ν_{NO}).

UV/Vis (reaction solution, H_2O, 3 mmol L^{-1}): λ/nm: 342 (CT), 440 (CT), 597 (d-d-transition).

The X-ray analyses of the coordination polymers $[Fe(H_2O)_4(\mathbf{2})_2]_{n/n} \cdot 2\ H_2O$ and $[Fe(H_2O)_2(\mathbf{4})_2]_{n/n}$ reveal a Fe:nta molar ratio of 3:2 instead of the supplied 1:1 proportion. Crystallization experiments were performed with magnesium sulfate (an aquated magnesium ion was expected to adopt the position of the bridging dicationic $[Fe(H_2O)_{4/2}]^{2+}$ moieties) in order to examine whether exact stoichiometric amounts would accelerate the crystallization of the complex polymers. The quantities of the chemicals used are given in Table 5.2 and Table 5.3. The free acid of the aminecarboxylate and the base were stirred in water (3 mL) for 30 min at room temperature. Magnesium sulfate and iron(II) sulfate heptahydrate were mixed and added to the colorless solution in portions. A slightly green solution resulted. After the treatment with gaseous nitric oxide (10 min), the green-black reaction solution was stored under an NO atmosphere and acetone (3 mL) was diffused into the solution for six months. The NO atmosphere was then changed to an argon atmosphere and ethanol (≈ 6 mL) was added as an additional antisolvent. No crystalline product was observed after one and a half years.

Table 5.2: Crystallisation attempts of an Fe/nta/NO species using magnesium sulfate.

	n/mmol $FeSO_4 \cdot 7H_2O$	n/mmol H_3nta	n/mmol $MgSO_4$	n/mmol NaOH	m/g $FeSO_4 \cdot 7H_2O$	m/g H_3nta	m/g $MgSO_4$	m/g NaOH
Exp. 1	0.66	0.66	0.33	1.4	0.18	0.13	0.040	0.057
Exp. 2	1.0	1.0	0.50	2.1	0.28	0.19	0.060	0.086

Table 5.3: Crystallisation attempts of an Fe/edta/NO species using magnesium sulfate.

	n/mmol $FeSO_4 \cdot 7H_2O$	n/mmol H_4edta	n/mmol $MgSO_4$	n/mmol KOH 85%	m/g $FeSO_4 \cdot 7H_2O$	m/g H_4edta	m/g $MgSO_4$	m/g KOH 85%
Exp. 1	0.66	0.66	0.33	2.2	0.18	0.19	0.040	0.12
Exp. 2	1.0	1.0	0.50	3.3	0.28	0.29	0.060	0.19

In order to reproduce the crystalline compound **3**, the crystalline precursor compound **6** · H_2O (0.100 g, 0.297 mmol in each case) was dissolved in water, methanol or in a 1:1 methanol/water mixture (1 mL in each case). The colorless solutions were treated with gaseous nitric oxide, whereupon the characteristic dark green color of the quartet-$\{FeNO\}^7$ chromophor was observable. The mixtures were stored at room temperature under an NO atmosphere and acetone (1 mL in each case) was diffused in the reaction mixtures. After six months, the NO atmosphere was changed to an argon atmosphere and ethanol (2 mL in each case) was added as an additional antisolvent. Analogous experiments were carried out with the colorless raw product that contains the [Fe^{II}(bhedda)] complex (**6**) as well as with the crystalline precursor compound **7** · H_2O in order to synthesize a crystalline Fe/hedtra/NO species. No crystalline product was obtained.

5.7 Synthesis of nitrosyl-iron complexes with amino acids

The quantities of the chemicals used are given in Tables 5.4–5.8. All experiments were carried out in MeCN, DMF or in a DMF/MeCN mixture. The amino acid, the auxiliary ligand (if desired) and the base TEA were suspended in the solvent and iron (II) triflate was added to the mixture in portions. Nitric oxide was bubbled through the yellowish-green suspension (orange when acac was used as an auxiliary ligand, red in the case of bipy or phen) for 10 min to 15 min at room temperature. After a few minutes, a dark reddish-brown solution occurred. This was taken as an indicator for the successful formation of a nitrosyl species. When DMF was used as the solvent, the dark reddish-brown reaction solution adopted a red coloring after a few days, indicating the oxidation of iron(II) to iron(III). Several attempts were made to obtain crystalline nitrosyl-iron species: the reaction mixtures were stored under an NO atmosphere at room temperature and *n*-pentane, acetone or diethyl ether was diffused into the solutions. Moreover, the reaction solutions were layered with *n*-hexane or *n*-pentane (the same volume as the solvent) and stored under an argon atmosphere at room temperature. The mixtures with the auxiliary ligands acac, tmeda, bpy and phen were stable against NO loss upon subjecting them to low pressure. These solutions were concentrated by the slow evaporation of the solvent *in vacuo* and stored under an argon atmosphere at 4°C. A Fe/gly/NO, a Fe/acac/his/NO, a Fe/asp/NO a Fe/asp/tmeda/NO and a Fe/tyr/NO species were obtained as amorphous black solids. These solids were dissolved in MeCN, DMF or in MeCN/DMF mixtures for temperature gradient crystallization. No crystalline product was obtained.

Table 5.4: Crystallization attempts of nitrosyl-iron complexes with amino acids from acetonitrile (MeCN) solution using different antisolvents (AS). P = *n*-pentane, A = acetone, E = diethyl ether.

Amino acid	n/mmol amino acid	n/mmol $Fe(OTf)_2 \cdot 1.9$ MeCN	n/mmol TEA	m/g amino acid	m/g $Fe(OTf)_2 \cdot 1.9$ MeCN	V/mL TEA	V/mL MeCN	V/mL AS
gly	0.46	0.23	0.46	0.035	0.10	0.064	1.0	P 2.5
L-ser	0.12	0.12	0.12	0.012	0.050	0.016	0.30	A 1.0
L-thr	0.30	0.30	0.30	0.036	0.13	0.042	1.0	P 1.5
L-his	0.12	0.12	0.058	0.018	0.050	0.0080	0.50	P 1.5
L-asp	0.30	0.30	0.60	0.040	0.13	0.083	3.0	E 2.0
L-cys	0.32	0.32	0.32	0.039	0.14	0.045	1.0	P 2.0
L-tyr	0.93	0.46	0.93	0.17	0.20	0.13	4.5	E 2.0
L-leu	1.9	0.97	1.9	0.26	0.42	0.27	3.0	A 3.5
L-phe	0.74	0.37	0.74	0.12	0.16	0.10	3.5	-

Table 5.5: Crystallization attempts of nitrosyl-iron complexes with amino acids and the auxiliary ligand acac from various solvents (S). MeCN = acetonitrile, DMF = *N,N*-dimethylformamide.

Amino acid	n/mmol amino acid	n/mmol $Fe(OTf)_2 \cdot 1.9$ MeCN	n/mmol TEA	n/mmol Hacac	m/g amino acid	m/g $Fe(OTf)_2 \cdot 1.9$ MeCN	V/mL TEA	V/mL Hacac	V/mL S
	1.7	1.7	1.3	1.7	0.26	0.73	0.18	0.17	DMF / MeCN 2.5 / 2.5
DL-his	1.0	1.0	0.75	1.0	0.16	0.43	0.10	0.10	DMF / MeCN 1.5 / 1.5
	1.0	1.0	0.75	1.0	0.16	0.43	0.10	0.10	MeCN 3.0
	1.0	1.0	0.75	1.0	0.13	0.43	0.10	0.10	MeCN / DMF 1.5 / 1.5
DL-asp	1.0	1.0	0.75	1.0	0.13	0.43	0.10	0.10	MeCN / DMF 1.5 / 1.5
	0.17	0.17	0.13	0.17	0.022	0.072	0.017	0.017	DMF 0.50
DL-ser	1.0	1.0	0.75	1.0	0.11	0.43	0.10	0.10	MeCN / DMF 1.5 / 1.5
DL-thr	1.0	1.0	0.75	1.0	0.12	0.43	0.10	0.10	MeCN / DMF 1.5 / 1.5

Table 5.6: Crystallization attempts of nitrosyl-iron complexes with amino acids and the auxiliary ligand tmeda from various solvents (S). MeCN = acetonitrile, DMF = *N,N*-dimethylformamide.

Amino acid	n/mmol amino acid	n/mmol $Fe(OTf)_2 \cdot 1.9$ MeCN	n/mmol TEA	n/mmol tmeda	m/g amino acid	m/g $Fe(OTf)_2 \cdot 1.9$ MeCN	V/mL TEA	V/mL tmeda	V/mL S
DL-his	1.7	1.7	0.85	1.7	0.26	0.73	0.12	0.26	DMF / MeCN 2.5 / 2.5
	1.0	1.0	0.50	1.0	0.16	0.43	0.069	0.15	MeCN 6.0
	1.0	1.0	0.50	1.0	0.13	0.43	0.069	0.15	MeCN / DMF 1.5 / 1.5
DL-asp	1.0	1.0	1.0	1.0	0.13	0.43	0.14	0.15	MeCN 3.0
	1.0	1.0	1.0	1.0	0.13	0.43	0.14	0.15	MeCN / DMF 1.5 / 1.5
	0.17	0.17	0.083	0.17	0.022	0.072	0.012	0.025	DMF 0.50
DL-ser	1.0	1.0	0.5	1.0	0.11	0.43	0.069	0.15	MeCN / DMF 1.5 / 1.5
DL-thr	0.17	0.17	0.080	0.17	0.020	0.072	0.012	0.025	MeCN / DMF 0.25 / 0.25

Table 5.7: Crystallization attempts of a nitrosyl-iron species with DL-His and the auxiliary ligand bpy.

n/mmol DL-his	n/mmol $Fe(OTf)_2 \cdot 1.9$ MeCN	n/mmol TEA	n/mmol bpy	m/g DL-his	m/g $Fe(OTf)_2 \cdot 1.9$ MeCN	V/mL TEA	m/g bpy	V/mL MeCN
1.0	1.0	0.50	1.0	0.16	0.43	0.069	0.16	3.0

Table 5.8: Crystallization attempts of a nitrosyl-iron species with DL-His and the auxiliary ligand phen.

n/mmol DL-his	n/mmol $Fe(OTf)_2 \cdot 1.9$ MeCN	n/mmol TEA	n/mmol phen	m/g DL-his	m/g $Fe(OTf)_2 \cdot 1.9$ MeCN	V/mL TEA	m/g phen	V/mL MeCN
1.0	1.0	0.50	1.0	0.16	0.43	0.069	0.18	3.0

Fe/gly/NO

IR (reaction solution, MeCN, ATR): $\tilde{\nu}$/cm^{-1}: 1789(vw,), 1740(vw).

IR (solid, ATR): $\tilde{\nu}$/cm^{-1}: 1799 (vw,), 1731 (vw).

Fe/ser/NO

IR (reaction solution, MeCN, ATR): $\tilde{\nu}$/cm^{-1}: 1803(vw, ν_{NO}).

Fe/acac/ser/NO

IR (reaction solution, MeCN/DMF, ATR): $\tilde{\nu}$/cm^{-1}: 1769 (m, ν_{NO}).

Fe/ser/tmeda/NO

IR (reaction solution, MeCN/DMF, ATR): $\tilde{\nu}$/cm^{-1}: 1779 (m, ν_{NO}).

Fe/thr/NO

IR (reaction solution, MeCN, ATR): $\tilde{\nu}$/cm^{-1}: 1782 (vw, ν_{NO}).

Fe/his/NO

IR (reaction solution, MeCN, ATR): $\tilde{\nu}$/cm^{-1}: 1791 (vw, ν_{NO}).

Fe/acac/his/NO

IR (reaction solution, MeCN/DMF, ATR): $\tilde{\nu}$/cm^{-1}: 1779 (m, ν_{NO}).

IR (solid, ATR): $\tilde{\nu}$/cm^{-1}: 1792 (vw, ν_{NO}).

Fe/his/tmeda/NO

IR (reaction solution, MeCN, ATR): $\tilde{\nu}$/cm^{-1}: 1751 (vw, ν_{NO}).

IR (reaction solution, MeCN/DMF, ATR): $\tilde{\nu}$/cm^{-1}: 1773 (m, ν_{NO}).

UV/Vis (reaction solution, MeCN, 3 mmol L^{-1}): λ/nm: 331 (CT), 440 (CT), 600 (d-d-transition).

Fe/bpy/his/NO

IR (reaction solution, MeCN, ATR): $\tilde{\nu}$/cm^{-1}: 1786 (w, ν_{NO}).

Fe/his/phen/NO

IR (reaction solution, MeCN, ATR): $\tilde{\nu}$/cm^{-1}: 1789 (vw, ν_{NO}).

Fe/asp/NO

IR (reaction solution, MeCN, ATR): $\tilde{\nu}$/cm^{-1}: 1817 (vw, ν_{NO}).

IR (solid, ATR): $\tilde{\nu}$/cm^{-1}: 1818 (vw, ν_{NO}).

Fe/acac/asp/NO

IR (reaction solution, DMF, ATR): $\tilde{\nu}$/cm^{-1}: 1771 (m, ν_{NO}).

IR (reaction solution, MeCN/DMF, ATR): $\tilde{\nu}$/cm^{-1}: 1778 (m, ν_{NO}).

Fe/asp/tmeda/NO

IR (reaction solution, DMF, ATR): $\tilde{\nu}$/cm^{-1}: 1776 (m, ν_{NO}).

IR (solid, ATR): $\tilde{\nu}$/cm^{-1}: 1772 (vw, ν_{NO}).

Fe/cys/NO

IR (reaction solution, MeCN, ATR): $\tilde{\nu}$/cm^{-1}: 1792 (vw,), 1762 (vw).

Fe/tyr/NO

IR (reaction solution, MeCN, ATR): $\tilde{\nu}$/cm^{-1}: 1793 (vw, ν_{NO}).

IR (solid, ATR): $\tilde{\nu}$/cm^{-1}: 1801 (vw, ν_{NO}).

Fe/leu/NO

IR (reaction solution, MeCN, ATR): $\tilde{\nu}$/cm^{-1}: 1796 (vw, ν_{NO}).

Fe/phe/NO

IR (reaction solution, MeCN, ATR): $\tilde{\nu}$/cm^{-1}: 1775 (vw, ν_{NO}).

5.8 Computational methods

DFT calculations were accomplished with the program system TURBOMOLE.[170,171] The starting geometries were taken either from X-ray diffraction or set up manually using the graphical interface TMOLEX.[172,173] Wave functions were calculated at the multipole-accelerated RI-DFT level, using the basis set def2-TZVP[122] and the functionals TPSSh[126], BP86[123,124] or B-97D[125]. All calculations were performed under tight convergence criteria using spin-unrestricted open-shell systems with a quartet spin state. COSMO[127] or COSMO-RS[128,129] was applied for solvent correction. The dispersion correction by Grimme with BJ-damping[174] was used to consider *van-der-Waals* interactions. Frequency analyses were run numerically and excited states were calculated in a TD-DFT approach.[141] Broken symmetry calculations[138,139] were done with the program system ORCA 3.0.3.[175] MPA[134] and NPA[135] analyses were carried out with the program package TURBOMOLE. The QTAIM analyses[136,137] were performed with the program system MULTIWFN[137], the AO-MIX CDA analyses with the program packet AO-MIX[132,133]. The input files for these calculations were obtained from spin-unrestricted single point calculations with the ORCA 3.0.3 program package, whereby the DFT-optimized structures were set as initial geometries.

6 Appendix

6.1 Packing diagrams of the crystal structures

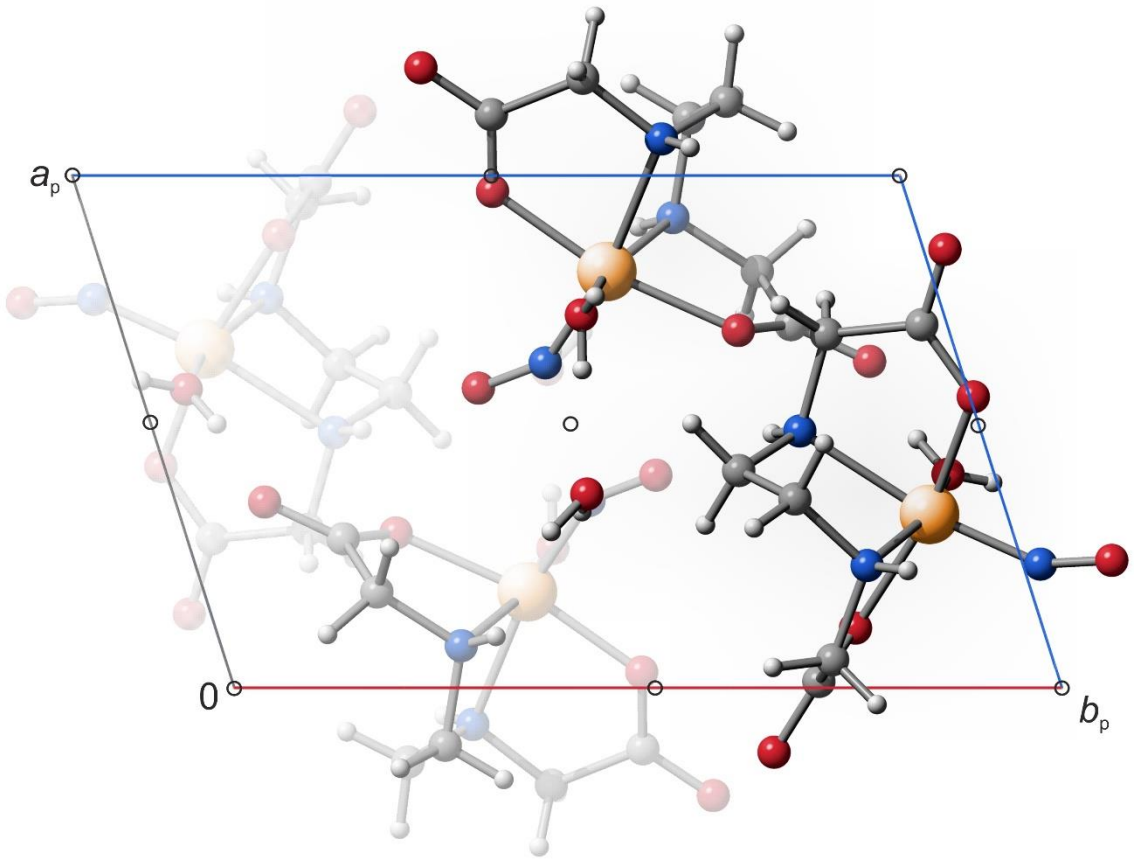

Figure 6.1: Packing diagram of **1b** · ½ H_2O in the triclinic space group $P\bar{1}$ with view along [001]. The symmetry elements of the space group $P\bar{1}$ are overlaid. Atoms: carbon (gray), hydrogen (white), iron (orange), nitrogen (blue), oxygen (red).

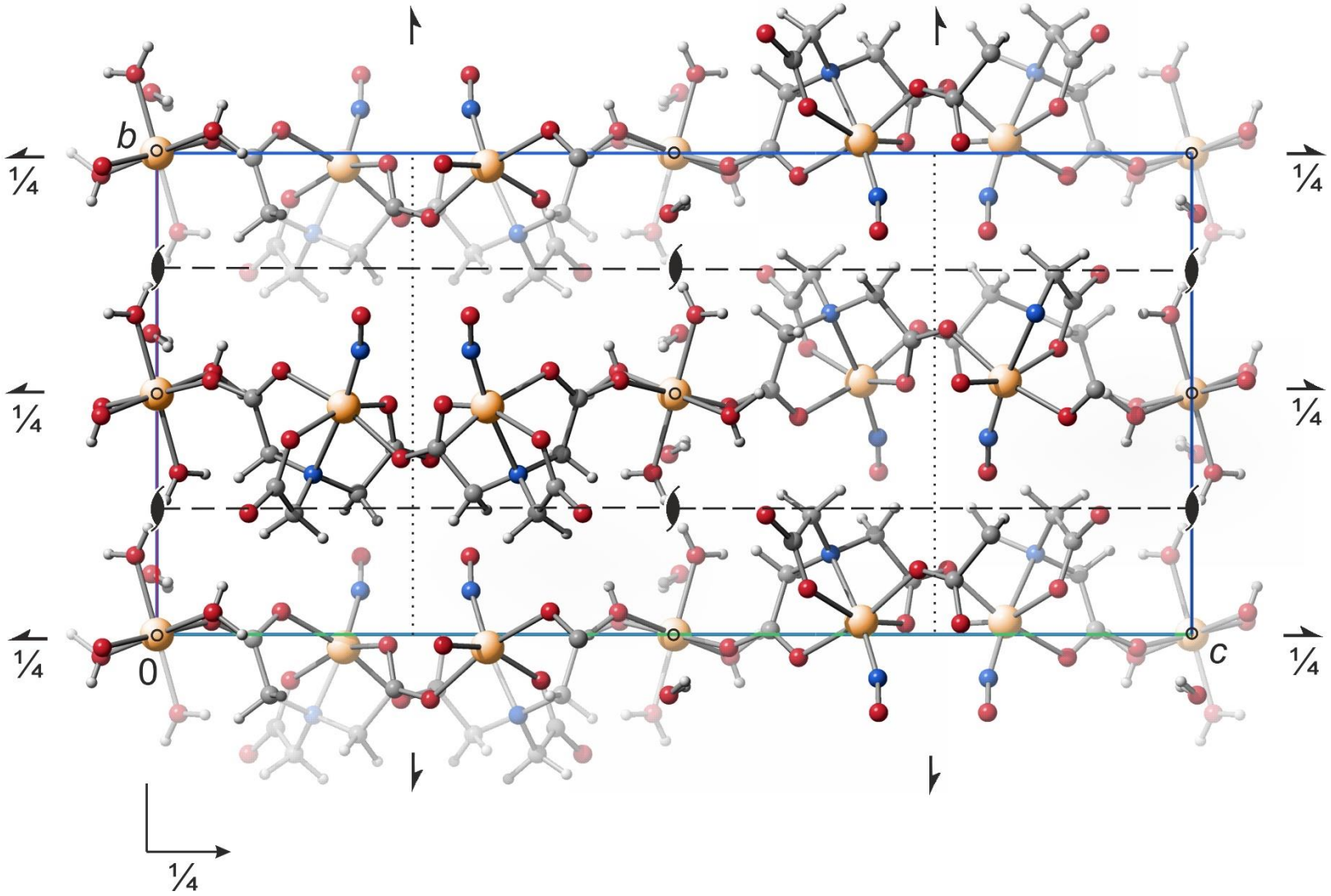

Figure 6.2: Packing diagram of $[Fe(H_2O)_4(\mathbf{2})_2]_{n/n} \cdot 2\ H_2O$ in the orthorhombic space group *Pbca* with view along [100]. The symmetry elements of the space group *Pbca* are overlaid. Atoms: carbon (gray), hydrogen (white), iron (orange), nitrogen (blue), oxygen (red).

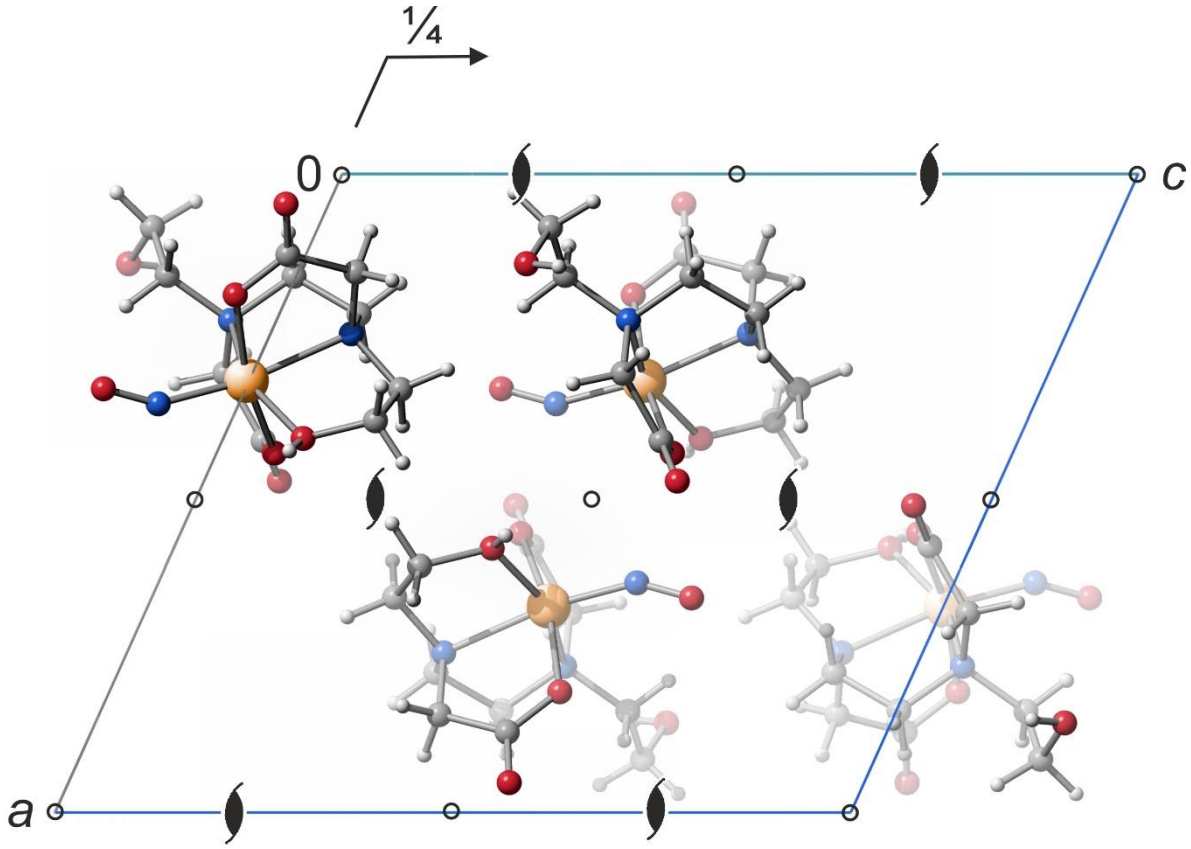

Figure 6.3: Packing diagram of **3** in the in the monoclinic space group $P2_1/c$ with view along [010]. The symmetry elements of the space group $P2_1/c$ are overlaid. Atoms: carbon (gray), hydrogen (white), iron (orange), nitrogen (blue), oxygen (red).

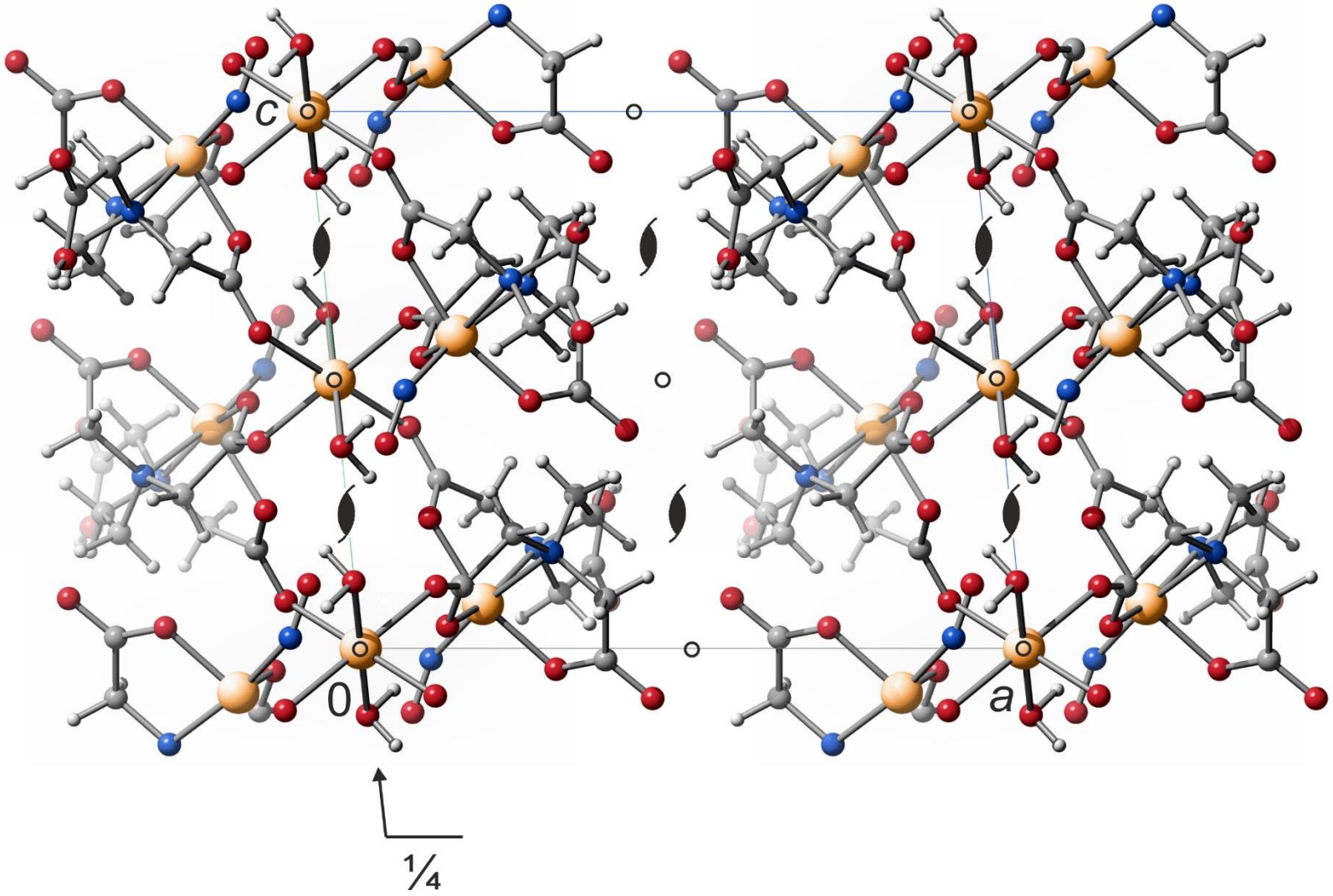

Figure 6.4: Packing diagram of $[Fe(H_2O)_2(\mathbf{4})_2]_{n/n}$ in the in the monoclinic space group $P2_1/c$ with view along [010]. The symmetry elements of the space group $P2_1/c$ are overlaid. Atoms: carbon (gray), hydrogen (white), iron (orange), nitrogen (blue), oxygen (red).

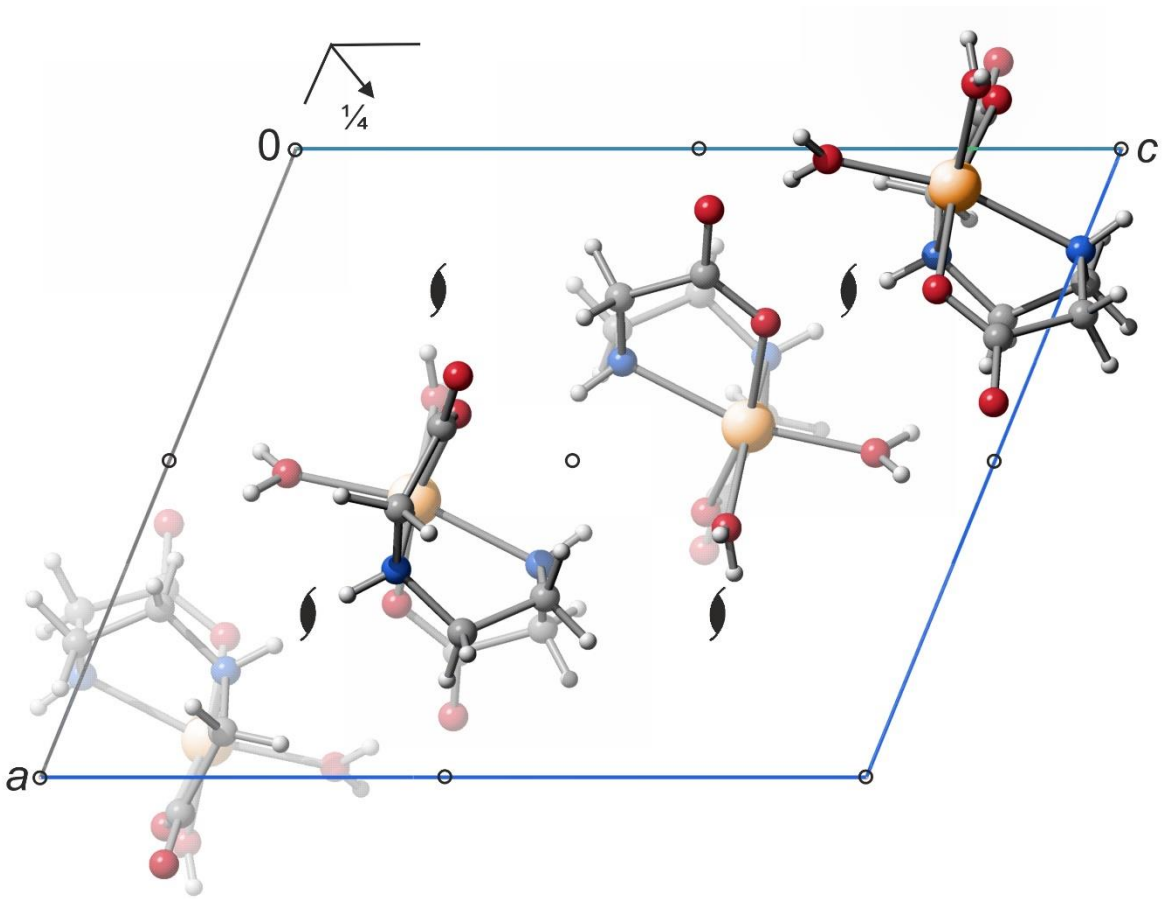

Figure 6.5: Packing diagram of **5b** in the in the monoclinic space group $P2_1/n$ with view along [010]. The symmetry elements of the space group $P2_1/n$ are overlaid. Atoms: carbon (gray), hydrogen (white), iron (orange), nitrogen (blue), oxygen (red).

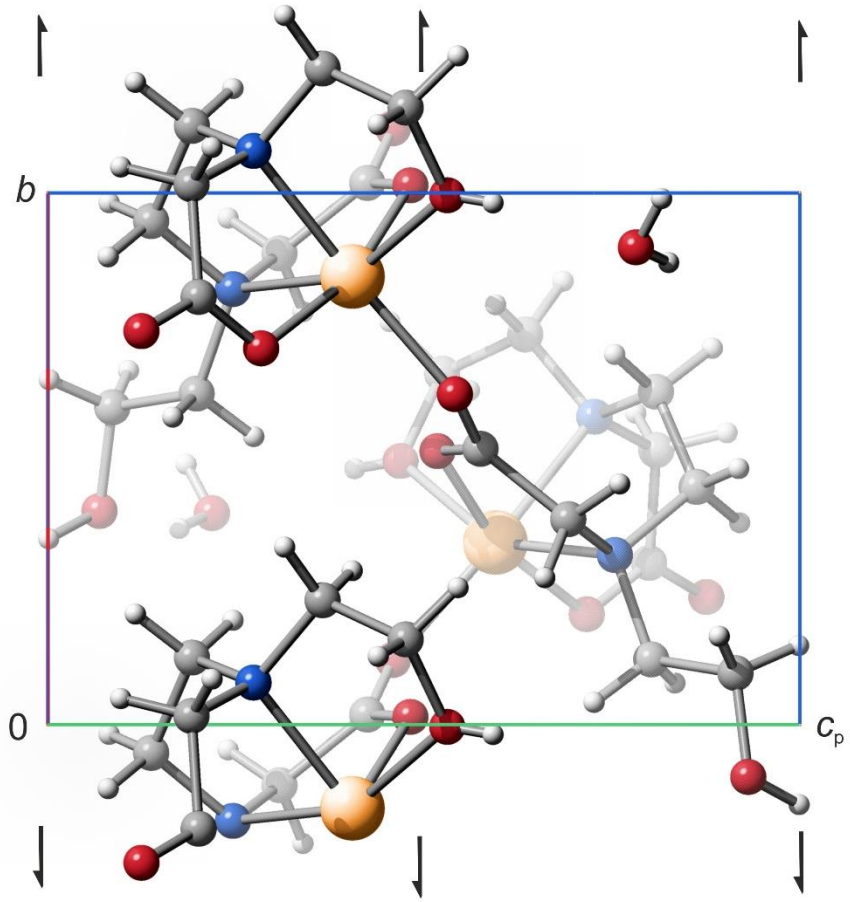

Figure 6.6: Packing diagram of **6** · H_2O in the in the monoclinic space group $P2_1$ with view along [100]. The symmetry elements of the space group $P2_1$ are overlaid. Atoms: carbon (gray), hydrogen (white), iron (orange), nitrogen (blue), oxygen (red).

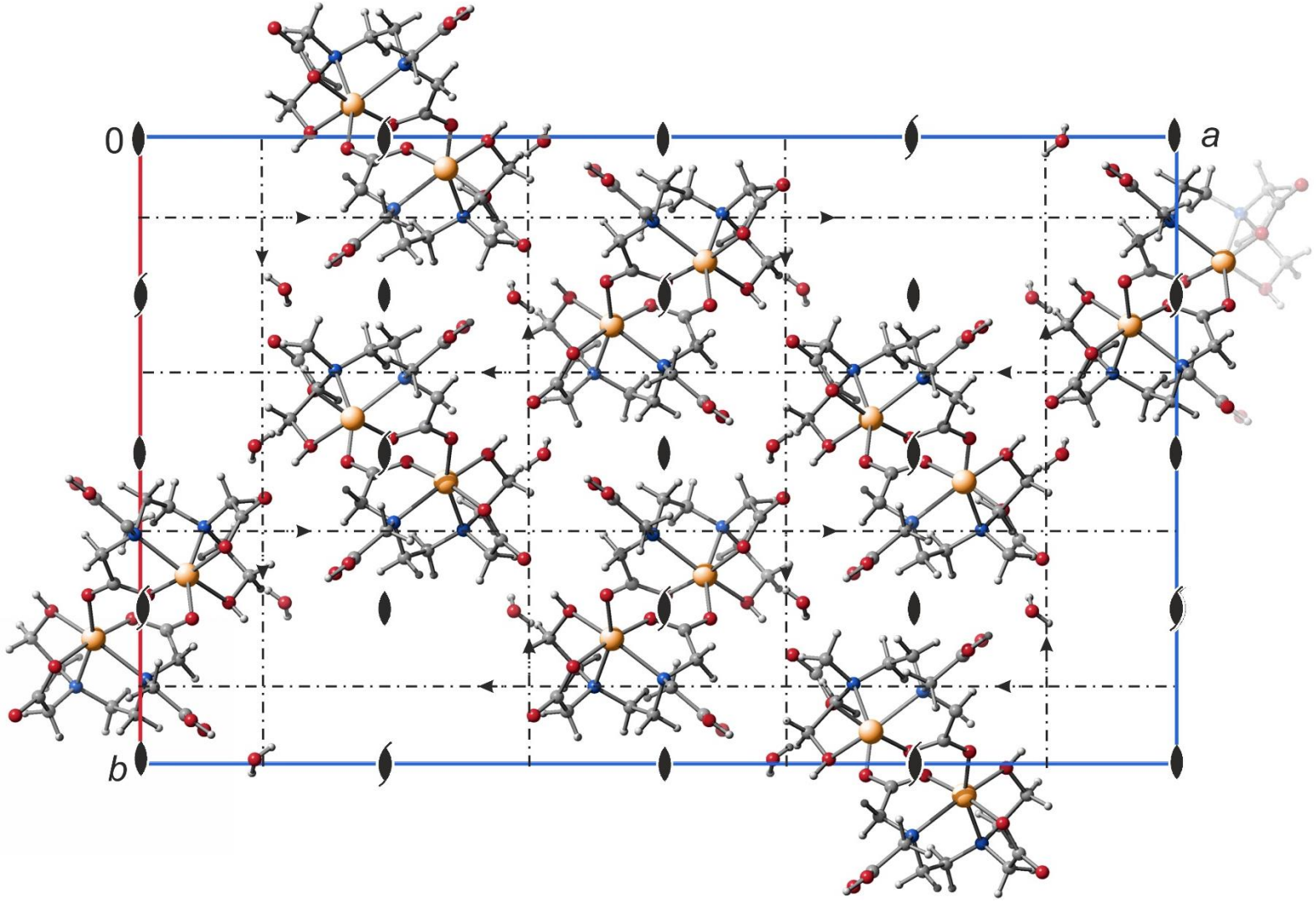

Figure 6.7: Packing diagram of **7** · H_2O in the orthorhombic space group *Fdd*2 with view along [001]. The symmetry elements of the space group *Fdd*2 are overlaid. Atoms: carbon (gray), hydrogen (white), iron (orange), nitrogen (blue), oxygen (red).

6.2 Crystallographic tables

Table 6.1: Crystallographic data of [Fe(edda)(H_2O)(NO)] · ½ H_2O (**1b** · ½ H_2O) and [{$Fe(H_2O)_4$}{Fe(NO)(nta)}$_2$]$_{n/n}$ · 2 H_2O = [$Fe(H_2O)_4$(**2**)$_2$]$_{n/n}$ · 2 H_2O.

compound	[Fe(edda)(H_2O)(NO)] · ½ H_2O (**1b** · ½ H_2O)	[$Fe(H_2O)_4$(**2**)$_2$]$_{n/n}$ · 2 H_2O
netto formula	$C_6H_{13}FeN_3O_{6.50}$	$C_6H_{12}Fe_{1.50}N_2O_{10}$
M_r/g mol^{-1}	287.04	355.95
crystal system	triclinic	orthorhombic
space group	$P\bar{1}$	*Pbca*
a/Å	7.9223(6)	7.6681(8)
b/Å	12.3799(9)	12.2304(15)
c/Å	12.4184(9)	26.315(3)
α/°	104.754(2)	90
β/°	101.383(2)	90
γ/°	103.638(2)	90
V/Å^3	1100.81(14)	2468.0(5)
Z	4	8
ρ/g cm^{-3}	1.732	1.916
μ/mm^{-1}	1.394	1.840
crystal size/mm	0.128 × 0.081 × 0.040	0.200 × 0.050 × 0.020
temperature/K	173(2)	173(2)
diffractometer	Bruker D8Quest	Bruker D8Venture
radiation	MoK_α	MoK_α
anode	rotating anode (TXS)	rotating anode (TXS)
rated input/kW	50	2.5
θ range/°	2.751–25.04	3.075–26.53
reflexes for metric	82	7045
absorption correction	multi-scan	multi-scan
transmission factors	0.6594–0.7452	0.6807–0.7454
reflexes measured	18384	65988
independent reflexes	3870	2551
R_{int}	0.0771	0.1142
mean σ(*I*)/*I*	0.0659	0.0574
reflexes with $I \geq 2\sigma(I)$	2816	1919
x, *y* (weighting scheme)	0.0324, 0.1791	0.0228, 5.2231
hydrogen refinement	[a]	[a]
Flack parameter	-	-
parameters	338	198
restraints	0	0
$R(F_{obs})$	0.0417	0.0410
$R_w(F^2)$	0.0815	0.0823
S	1.043	1.136
shift/error$_{max}$	0.001	0.001
max. electron density/e Å^{-3}	0.459	0.542
min. electron density/e Å^{-3}	−0.407	–0.680

[a] The coordinates of hydrogen atoms bonded to oxygen atoms and nitrogen atoms were refined freely. The other hydrogen atoms were calculated in idealized positions, riding on their parent atoms. U_{iso} was always coupled to the parent atom.

Table 6.2: Crystallographic data of [Fe(bhedda)(NO)] (**3**) and $[Fe(H_2O)_2\{Fe(NO)(Hedta)\}_2]_{n/n}$ = $[Fe(H_2O)_2(\mathbf{4})_2]_{n/n}$.

compound	[Fe(bhedda)(NO)] (**3**)	$[Fe(H_2O)_2(\mathbf{4})_2]_{n/n}$
netto formula	$C_{10}H_{18}FeN_3O_7$	$C_{10}H_{15}Fe_{1.50}N_3O_{10}$
M_r/g mol^{-1}	348.12	421.02
crystal system	monoclinic	monoclinic
space group	$P2_1/c$	$P2_1/c$
a/Å	13.4496(5)	13.5547(5)
b/Å	7.2995(3)	9.7325(4)
c/Å	15.2882(6)	11.0127(4)
α/°	90	90
β/°	114.2367(11)	95.5394(13)
γ/°	90	90
V/Å^3	1368.63(9)	1446.02(10)
Z	4	4
ρ/g cm^{-3}	1.689	1.934
μ/mm^{-1}	1.141	1.589
crystal size/mm	0.100 × 0.030 × 0.020	0.250 × 0.050 × 0.050
temperature/K	173(2)	173(2)
diffractometer	Bruker D8Venture	Bruker D8Venture
radiation	MoK$_\alpha$	MoK$_\alpha$
anode	rotating anode (TXS)	rotating anode (TXS)
rated input/kW	2.5	2.5
θ range/°	3.150–27.50	3.020–27.17
reflexes for metric	8332	6211
absorption correction	multi-scan	multi-scan
transmission factors	0.7002–0.7456	0.6746–0.7455
reflexes measured	24600	18231
independent reflexes	3158	3200
R_{int}	0.0399	0.0383
mean σ(I)/I	0.0257	0.0272
reflexes with $I \geq 2\sigma(I)$	2669	2730
x, y (weighting scheme)	0.0274, 1.2541	0.0323, 1.7839
hydrogen refinement	[a]	[a]
Flack parameter	-	-
parameters	196	225
restraints	0	0
$R(F_{obs})$	0.0288	0.0299
$R_w(F^2)$	0.0678	0.0715
S	1.066	1.037
shift/error$_{max}$	0.001	0.001
max. electron density/e Å^{-3}	0.459	1.456
min. electron density/e Å^{-3}	–0.239	–0.388

[a] The coordinates of hydrogen atoms bonded to oxygen atoms were refined freely. The other hydrogen atoms were calculated in idealized positions, riding on their parent atoms. U_{iso} was always coupled to the parent atom.

Table 6.3: Crystallographic data of $[Fe^{II}(edda)(H_2O)_2]$ (**5b**) and $[Fe^{II}(bhedda)] \cdot H_2O$ (**6** · H_2O).

compound	$[Fe^{II}(edda)(H_2O)_2]$ (**5b**)	$[Fe^{II}(bhedda)] \cdot H_2O$ (**6** · H_2O)
netto formula	$C_6H_{14}FeN_2O_6$	$C_{10}H_{20}FeN_2O_7$
M_r/g mol^{-1}	266.04	336.13
crystal system	$P2_1/n$	$P2_1$
space group	monoclinic	monoclinic
a/Å	10.9071(3)	9.2749(5)
b/Å	7.5083(2)	7.1006(3)
c/Å	13.2820(4)	10.9111(6)
α/°	90	90
β/°	112.1251(9)	113.0863(15)
γ/°	90	90
V/Å^3	1007.62(5)	661.03(6)
Z	4	2
ρ/g cm^{-3}	1.754	1.689
μ/mm^{-1}	1.509	1.175
crystal size/mm	0.100 × 0.100 × 0.080	0.100 × 0.080 × 0.020
temperature/K	173(2)	173(2)
diffractometer	Bruker D8Venture	Bruker D8Venture
radiation	MoK_α	MoK_α
anode	rotating anode (TXS)	rotating anode (TXS)
rated input/kW	2.5	2.5
θ range/°	2.071–27.50	2.029–26.41
reflexes for metric	5986	9937
absorption correction	multi-scan	multi-scan
transmission factors	0.6955–0.7456	0.6869–0.7454
reflexes measured	11432	16822
independent reflexes	2299	2670
R_{int}	0.0331	0.0332
mean σ(I)/I	0.0275	0.0325
reflexes with $I \geq 2\sigma(I)$	2022	2627
x, y (weighting scheme)	0.0094, 1.1532	0.0529, 0.0476
hydrogen refinement	[a]	[a]
Flack parameter	-	0.023(6)
parameters	160	195
restraints	0	4
$R(F_{obs})$	0.0240	0.0263
$R_w(F^2)$	0.0582	0.1066
S	1.080	1.586
shift/error$_{max}$	0.001	0.002
max. electron density/e Å^{-3}	0.413	0.649
min. electron density/e Å^{-3}	−0.369	–0.758

[a] The coordinates of hydrogen atoms bonded to oxygen atoms and nitrogen atoms were refined freely. The other hydrogen atoms were calculated in idealized positions, riding on their parent atoms. U_{iso} was always coupled to the parent atom.

Table 6.4: Crystallographic data of $[Fe^{II}(Hhedtra)] \cdot H_2O$ (**7** · H_2O).

compound	$[Fe^{II}(Hhedtra)] \cdot H_2O$ (**7** · H_2O)
netto formula	$C_{10}H_{18}FeN_2O_8$
M_r/g mol^{-1}	350.11
crystal system	orthorhombic
space group	*Fdd*2
a/Å	36.366(3)
b/Å	21.9743(15)
c/Å	6.9742(5)
α/°	90
β/°	90
γ/°	90
V/Å^3	5573.2(7)
Z	16
ρ/g cm^{-3}	1.669
μ/mm^{-1}	1.124
crystal size/mm	0.170 × 0.060 × 0.050
temperature/K	173(2)
diffractometer	Bruker D8Venture
radiation	MoK_α
anode	rotating anode (TXS)
rated input/kW	2.5
θ range/°	2.908–26.11
reflexes for metric	9914
absorption correction	multi-scan
transmission factors	0.6479–0.7453
reflexes measured	34506
independent reflexes	2692
R_{int}	0.0808
mean σ(*I*)/*I*	0.0342
reflexes with $I \geq 2\sigma(I)$	2540
x, *y* (weighting scheme)	0.0369, 5.9986
hydrogen refinement	[a]
Flack parameter	0.000(9)
parameters	203
restraints	1
$R(F_{obs})$	0.0278
$R_w(F^2)$	0.0670
S	1.074
shift/error$_{max}$	0.001
max. electron density/e Å^{-3}	0.464
min. electron density/e Å^{-3}	−0.287

[a] The coordinates of hydrogen atoms bonded to oxygen atoms were refined freely. The other hydrogen atoms were calculated in idealized positions, riding on their parent atoms. U_{iso} was always coupled to the parent atom.

7 Bibliography

[1] N. G. Connelly, T. Damhus, R. M. Hartshorn, A. T. Hutton, *Nomenclature of Inorganic Chemistry*, RSC Publishing, 1. Edition, **2005**, 182−183.

[2] M. C. Etter, J. C. MacDonald, J. Bernstein, *Acta Crystallogr., Sect. B* **1990**, *46*, 256–262.

[3] J. Bernstein, R. E. Davis, L. Shimoni, N.-L. Chang, *Angew. Chem. Int. Ed.* **1995**, *34*, 1555–1573; J. Bernstein, R. E. Davis, L. Shimoni, N.-L. Chang, *Angew. Chem.* **1995**, *15*, 1689–1708.

[4] M. Wolf, *Synthesis, Characterization and Quantum-Chemical Analysis of {FeNO}^{7} and {Fe(NO)$_2$}^{9} Compounds*, Dissertation, LMU Munich, **2016**.

[5] P. J. Crutzen, *Q. J. R. Meteorol. Soc.* **1970**, *96*, 320–325.

[6] H. Johnston, *Science* **1971**, *173*, 517–522.

[7] P. Brimblecombe, D. H. Stedman, *Nature* **1982**, *298*, 460–462.

[8] D. Wink, Y. Vodovotz, J. Laval, F. Laval, M. W. Dewhirst, J. B. Mitchell, *Carcinogenesis* **1998**, *19*, 711–721.

[9] D. Koshland, Jr., *Science* **1992**, *258*, 1861.

[10] E. Culotta, D. Koshland, Jr., *Science* **1992**, *258*. 1862–1865.

[11] R. F. Furchgott, *Angew. Chem. Int. Ed.* **1999**, *38*, 1870–1880; R. F. Furchgott, *Angew. Chem.* **1999**, *111*, 1990−2000.

[12] L. J. Ignarro, *Angew. Chem. Int. Ed*. **1999**, *38*, 1882−1892; L. J. Ignarro, *Angew. Chem.* **1999**, *111*, 2002−2013.

[13] F. Murad, *Angew. Chem. Int. Ed.* **1999**, *38*, 1856–1868; F. Murad, *Angew. Chem.* **1999**, *111*, 1976−1989.

[14] J. Bradbury, *Lancet* **1998**, *352*, 1287.

[15] S. Khatua, A. Majumdar, *J. Inorg. Biochem.* **2015**, *142*, 145–153.

[16] C. Fionda, M. P. Abruzzese, A. Santoni, M. Cippitelli, *Curr. Med. Chem.* **2016**, *23*, 2618–2636.

[17] P. Cabrales, J. M. Friedman, *Antioxid. Redox Signaling* **2013**, *18*, 2284–2297.

[18] E. R. Derbyshire, M. A. Marletta, *Annu. Rev. Biochem.* **2012**, *81*, 533–559.

[19] T. L. Poulos, *Chem. Rev.* **2014**, *114*, 3919–3962.

[20] A. Modin, H. Björne, M. Herulf, K. Alving, E. Weitzberg, J. O. N. Lundberg, *Acta Physiol. Scand.* **2001**, *171*, 9–16.

[21] E. Martin, V. Berka, I. Sharina, A. L. Tsai, *Biochemistry* **2012**, *51*, 2737–2746.

[22] B.-K. Yoo, I. Lamarre, J.-L. Martin, F. Rappaport, M. Negrerie, *PNAS* **2015**, *112*, E1697-E1704.

[23] M. Russwurm, D. Koesling, *EMBO J.* **2004**, *23*, 4443–50.

[24] M. A. Herzik, R. Jonnalagadda, J. Kuriyan, M. A. Marletta, *PNAS* **2014**, *111*, E4156–E4164.

[25] D. Basudhar, L. A. Ridnour, R. Cheng, A. H. Kesarwala, J. Heinecke, D. A. Wink, *Coord. Chem. Rev.* **2016**, *306*, 708–723.

[26] F. A. Walker, *J. Inorg. Biochem.* **2005**, *99*, 216–236.

[27] W. Flores-Santana, C. Switzer, L. A. Ridnour, D. Basudhar, D. Mancardi, S. Donzelli, D. D. Thomas, K. M. Miranda, J. M. Fukuto, D. A. Wink, *Arch. Pharmcol. Res.* **2009**, *32*, 1139–1153.

[28] R. F. Eich, T. Li, D. D. Lemon, D. H. Doherty, S. R. Curry, J. F. Aitken, A. J. Mathews, K. A. Johnson, R. D. Smith, G. N. Phillips, Jr., J. S. Olson, *Biochemistry* **1996**, *35*, 6976–6983.

[29] J. R. Lancaster, Jr., *Nitric Oxide* **1997**, *1*, 18–30.

[30] J. R. Lancaster, Jr., *Future Sci. OA* **2015**, *1*, FSO59.

[31] O. Wilhelm, *Improvements in the Manufacture of Nitric Acid and Nitrogen Oxides*, **1902**, GB190200698 (A).

[32] A. F. Holleman, E. Wiberg, *Lehrbuch der Anorganischen Chemie*, 102nd Edition, Walter de Gruyter, Berlin, New York, **2007**, 707–712.

[33] F. J. Lovas, E. Tiemann, *J. Phys. Chem. Ref. Data* **1974**, *3*, 609–770.

[34] J. A. McCleverty, *Chem. Rev.* **2004**, *104*, 403–418.

[35] I. G. Zacharia, W. M. Deen, *Ann. Biomed. Eng.* **2005**, *33*, 214–222.

[36] K. Ray, T. Petrenko, K. Wieghardt, F. Neese, *Dalton Trans.* **2007**, 1552.

[37] F. Roncaroli, M. Videla, L. D. Slep, J. A. Olabe, *Coord. Chem. Rev.* **2007**, *251*, 1903–1930.

[38] J. McCracken, P. J. Cappillino, J. S. McNally, M. D. Krzyaniak, M. Howart, P. C. Tarves, J. P. Caradonna, *Inorg. Chem.* **2015**, *54*, 6486–6497.

[39] J. H. Enemark, R. Feltham, *Coord. Chem. Rev.* **1974**, *13*, 339–406.

[40] Y. Zhang, W. Gossman, E. Oldfield, *J. Am. Chem. Soc.* **2003**, *125*, 16387–16396.

[41] M. S. Liao, M. J. Huang, J. D. Watts, *J. Phys. Chem. B* **2013**, *117*, 10103–10114.

[42] A. P. Hunt, N. Lehnert, *Acc. Chem. Res.* **2015**, *48*, 2117–2125.

[43] T. Hino, Y. Matsumoto, S. Nagano, H. Sugimoto, Y. Fukumori, T. Murata, S. Iwata, Y. Shiro, *Science* **2010**, *330*, 1666–1670.

[44] H. Shoun, S. Fushinobu, L. Jiang, S.-W. Kim, T. Wakagi, *Philos. Trans. R. Soc. B Biol. Sci.* **2012**, *367*, 1186–1194.

[45] Y. Shiro, *Biochim. Biophys. Acta - Bioenerg.* **2012**, *1817*, 1907–1913.

[46] T. C. Berto, A. L. Speelman, S. Zheng, N. Lehnert, *Coord. Chem. Rev.* **2013**, *257*, 244–259.

[47] A. L. Speelman, N. Lehnert, *Acc. Chem. Res.* **2014**, *47*, 1106–1116.

[48] P. Maas, T. Van De Sandt, *Biotechnol. Prog.* **2003**, *19*, 1323–1328.

[49] P. van der Maas, L. Harmsen, S. Weelink, B. Klapwijk, P. Lens, *J. Chem. Technol. Biotechnol.* **2004**, *79*, 835–841.

[50] H. Niu, D. Y. C. Leung, *Environ. Rev.* **2010**, *18*, 175–189.

[51] Y. Xia, Y. Shi, Y. Zhou, N. Liu, W. Li, S. Li, *Energy Fuels* ***2014***, *28*, 3332−3338.

[52] N. Liu, Y. Jiang, L. Zhang, Y. Xia, B. Lu, B. Xu, W. Li, S. Li, *Energy Fuels* **2014**, *28*, 7591–7598

[53] C. de Salas, M. R. Heinrich, *Green Chem.* **2014**, *16*, 2982–2987.

[54] N. Klueglein, F. Picardal, M. Zedda, C. Zwiener, A. Kappler, *Geobiology* **2015**, *13*, 198–207.

[55] Y. Xia, J. Zhao, M. Li, S. Zhang, S. Li, W. Li, *Environ. Sci. Technol.* **2016**, *50*, 3846–3851.

[56] W. Li, J. Zhao, L. Zhang, Y. Xia, N. Liu, S. Li, S. Zhang, *Scientific Reports* **2016**, *6*, Article number: 18876.

[57] F. He, X. Deng, M. Chen, *Chemosphere* **2017**, *168*, 623–629.

[58] C. D. Brown, M. L. Neidig, M. B. Neibergall, J. D. Lipscomb, E. I. Solomon, *J. Am. Chem. Soc.* **2007**, *129*, 7427–7438.

[59] M. Ray, A. P. Golombek, M. P. Hendrich, G. P. A. Yap, L. M. Liable-Sands, A. L. Rheingold, A. S. Borovik, *Inorg. Chem.* **1999**, *38*, 3110–3115.

[60] T. C. Berto, M. B. Hoffman, Y. Murata, K. B. Landenberger, E. E. Alp, J. Zhao, N. Lehnert, *J. Am. Chem. Soc.* **2011**, *133*, 16714–16717.

[61] Y. Zhang, M. A. Pavlosky, C. A. Brown, T. E. Westre, B. Hedman, K. O. Hodgson, E. I. Solomon, *J. Am. Chem. Soc.* **1992**, *114*, 9189–9191.

[62] C. A. Brown, M. A. Pavlosky, T. E. Westre, Y. Zhang, E. I. Solomon, B. Hedman, K. O. Hodgson, *J. Am. Chem. Soc.* **1995**, *117*, 715–732.

[63] T. A. Jackson, E. Yikilmaz, A. F. Miller, T. C. Brunold, *J. Am. Chem. Soc.* **2003**, *125*, 8348–8363.

[64] J. Li, A. Banerjee, P. L. Pawlak, W. W. Brennessel, F. A. Chavez, *Inorg. Chem.* **2014**, *53*, 5414–5416.

[65] S. Ye, J. C. Price, E. W. Barr, M. T. Green, J. M. Bollinger, C. Krebs, F. Neese, *J. Am. Chem. Soc.* **2010**, *132*, 4739–4751.

[66] G. Schenk, M. Y. M. Pau, E. I. Solomon, *J. Am. Chem. Soc.* **2004**, *126*, 505–515.

[67] A. R. Diebold, C. D. Brown-Marshall, M. L. Neidig, J. M. Brownlee, G. R. Moran, E. I. Solomon, *J. Am. Chem. Soc.* **2011**, *133*, 18148–18160.

[68] K. Nakahara, T. Tanimoto, K. I. Hatano, K. Usuda, H. Shoun, *J. Biol. Chem.* **1993**, *268*, 8350–8355.

[69] E. Obayashi, S. Takahashi, Y. Shiro, *J. Am. Chem. Soc.* **1998**, *120*, 12964–12965.

[70] R. Silaghi-Dumitrescu, D. M. Kurtz, L. G. Ljungdahl, W. N. Lanzilotta, *Biochemistry* **2005**, *44*, 6492–6501.

[71] D. M. Kurtz, Jr., *Dalt. Trans.* **2007**, *37*, 4115–4121.

[72] A. Daiber, T. Nauser, N. Takaya, T. Kudo, P. Weber, C. Hultschig, H. Shoun, V. Ullrich, *J. Inorg. Biochem.* **2002**, *88*, 343–352.

[73] C. Riplinger, F. Neese, *ChemPhysChem* **2011**, *12*, 3192–3203.

[74] P. Moënne-Loccoz, *Nat. Prod. Rep.* **2007**, *24*, 610–620.

[75] S. Chakraborty, J. Reed, J. T. Sage, N. C. Branagan, I. D. Petrik, K. D. Miner, M. Y. Hu, J. Zhao, E. E. Alp, Y. Lu, *Inorg. Chem.* **2015**, *54*, 9317–9329.

[76] H. Kumita, K. Matsuura, T. Hino, S. Takahashi, H. Hori, Y. Fukumori, I. Morishima, Y. Shiro, *J. Biol. Chem.* **2004**, *279*, 55247–55254.

[77] H. Matsumura, S. Chakraborty, J. Reed, Y. Lu, P. Moënne- Loccoz, *Biochemistry* **2016**, *55*, 2091–2099.

[78] M. R. A. Blomberg, P. E. M. Siegbahn, *Biochemistry* **2012**, *51*, 5173–5186.

[79] T. Hayashi, J. D. Caranto, D. A. Wampler, D. M. Kurtz, P. Moënne-Loccoz, *Biochemistry* **2010**, *49*, 7040–7049.

[80] T. Hayashi, J. D. Caranto, H. Matsumura, D. M. Kurtz, P. Moënne-Loccoz, *J. Am. Chem. Soc.* **2012**, *134*, 6878–6884.

[81] S. Zheng, T. C. Berto, E. W. Dahl, M. B. Hoffman, A. L. Speelman, N. Lehnert, *J. Am. Chem. Soc.* **2013**, *135*, 4902–4905.

[82] A. A. A. Attia, R. Silaghi-Dumitrescu, *Eur. J. Inorg. Chem.* **2014**, *35*, 6061–6065.

[83] A. L. Speelman, *Investigation of the Electronic Structure and Reactivity of Non-Heme Iron Nitrosyl and Nitroxyl Complexes*, Dissertation, University of Michigan, **2016**.

[84] D. Littlejohn, S. G. Chang, *J. Phys. Chem.* **1982**, *86*, 537–540.

[85] D. Littlejohn, S. G. Chang, *Ind. Eng. Chem. Res.* **1987**, *26*, 1232–1234.

[86] A. Wanat, T. Schneppensieper, G. Stochel, R. van Eldik, E. Bill, K. Wieghardt, *Inorg. Chem.* **2002**, *41*, 4–10.

[87] T. Schneppensieper, S. Finkler, A. Czap, R. van Eldik, M. Heus, P. Nieuwenhuizen, C. Wreesmann, W. Abma, *Eur. J. Inorg. Chem.* **2001**, 491–501.

[88] T. Schneppensieper, A. Wanat, G. Stochel, R. Van Eldik, *Inorg. Chem.* **2002**, *41*, 2565–2573.

[89] M. Wolak, R. Van Eldik, *Coord. Chem. Rev.* **2002**, *230*, 263–282.

[90] T. Schneppensieper, A. Wanat, G. Stochel, S. Goldstein, D. Meyerstein, R. van Eldik, *Eur. J. Inorg. Chem.* **2001**, 2317–2325.

[91] R. Sander, *Atmos. Chem. Phys.* **2015**, *15*, 4399–4981.

[92] H.-Y. Cheng, S. Chang, P.-Y. Tsai, *J. Phys. Chem. A* **2004**, *108*, 358–361.

[93] E. Broclawik, A. Stępniewski, M. Radoń, *J. Inorg. Biochem.* **2014**, *136*, 147–153.

[94] M. Radoń, E. Broclawik, K. Pierloot, *J. Phys. Chem. B* **2010**, *114*, 1518–1528.

[95] J. Conradie, K. H. Hopmann, A. Ghosh, *J. Phys. Chem. B* **2010**, *114*, 8517–8524.

[96] J. Conradie, A. Ghosh, *Inorg. Chem.* **2011**, *50*, 4223–4225.

[97] F. C. Lo, Y. W. Li, I. J. Hsu, C. H. Chen, W. F. Liaw, *Inorg. Chem.* **2014**, *53*, 10881–10892.

[98] E. Victor, M. A. Minier, S. J. Lippard, *Eur. J. Inorg. Chem.* **2014**, 5640–5645.

[99] E. Victor, S. Kim, S. J. Lippard, *Inorg. Chem.* **2014**, *53*, 12809–12821.

[100] F. Te Tsai, Y. C. Lee, M. H. Chiang, W. F. Liaw, *Inorg. Chem.* **2013**, *52*, 464–473.

[101] A. Majumdar, S. J. Lippard, *Inorg. Chem.* **2013**, *52*, 13292–13294.

[102] H. Park, M. M. Bittner, J. S. Baus, S. V. Lindeman, A. T. Fiedler, *Inorg. Chem.* **2012**, *51*, 10279–10289.

[103] G. Villar-Acevedo, E. Nam, S. Fitch, J. Benedict, J. Freudenthal, W. Kaminsky, J. A. Kovacs, *J. Am. Chem. Soc.* **2011**, *133*, 1419–1427.

[104] F. Te Tsai, P. L. Chen, W. F. Liaw, *J. Am. Chem. Soc.* **2010**, *132*, 5290–5299.

[105] D. P. Klein, V. G. Young, W. B. Tolman, L. Que, *Inorg. Chem.* **2006**, *45*, 8006–8008.

[106] B. Weber, H. Görls, M. Rudolph, E. G. Jäger, *Inorg. Chim. Acta* **2002**, *337*, 247–265.

[107] M. Li, D. Bonnet, E. Bill, F. Neese, T. Weyhermüller, N. Blum, D. Sellmann, K. Wieghardt, *Inorg. Chem.* **2002**, *41*, 3444–3456.

[108] C. Hauser, T. Glaser, E. Bill, T. Weyhermüller, K. Wieghardt, *J. Am. Chem. Soc.* **2000**, *122*, 4352–4365.

[109] A. L. Feig, M. T. Bautista, S. J. Lippard, *Inorg. Chem.* **1996**, *35*, 6892–6898.

[110] Y. M. Chiou, L. Que, *Inorg. Chem.* **1995**, *34*, 3270–3278.

[111] C. R. Randall, Y. Zang, A. E. True, L. Que, J. M. Charnock, C. D. Garner, Y. Fujishima, C. J. Schofield, J. E. Baldwin, *Biochemistry* **1993**, *32*, 6664–6673.

[112] K. Pohl, K. Wieghardt, B. Nuber, J. Weiss, *J. Chem. Soc. Dalt. Trans.* **1987**, 187–192.

[113] A. L. Speelman, N. Lehnert, *Angew. Chem. Int. Ed.* **2013**, *52*, 12283–12287.

[114] A. C. Mcquilken, Y. Ha, K. D. Sutherlin, M. A. Siegler, K. O. Hodgson, B. Hedman, E. I. Solomon, G. N. L. Jameson, D. P. Goldberg, *J. Am. Chem. Soc.* **2013**, *135*, 14024–14027.

[115] M. Wolf, P. Klüfers, *Eur. J. Inorg. Chem.* **2017**, *17*, 2303–2312.

[116] T. E. Westre, A. DiCicco, A. Filipponi, C. R. Natoli, B. Hedman, E. I. Solomon, K. O. Hodgson, *J. Am. Chem. Soc.* **1994**, *116*, 6757–6768.

[117] D. Schurr, J. Guhathakurta, S. Simon, G. Rinke, R. Dittmeyer, *Chem. Eng. Technol.* **2017**, *40*, 1400–1407.

[118] J. Guhathakurta, D. Schurr, G. Rinke, R. Dittmeyer, S. Simon, *J. Sens. Sens. Syst.* **2017**, 223–236.

[119] K. Haase, U. D. Kück, J. Thöming, C. J. Kähler, *Chem. Eng. Technol.* **2017**, *40*, 1502–1511.

[120] T. G. Wensel, C. F. Meares, *Biochemistry* **1983**, *22*, 6247–6284.

[121] P. Kubelka, *J. Opt. Soc. Am.* **1948**, *38*, 448–457.

[122] F. Weigend, R. Ahlrichs, *Phys. Chem. Chem. Phys.* **2005**, *7*, 3297–3305.

[123] A. D. Becke, *Phys. Rev. A* **1988**, *38*, 3098–3100.

[124] J. P. Perdew, *Phys. Rev. B* **1986**, *33*, 8822–8824.

[125] S. Grimme, *J. Comput. Chem.* **2006**, *28*, 73–86.

[126] J. Tao, J. P. Perdew, V. N. Staroverov, G. E. Scuseria, *Phys. Rev. Lett.* **2003**, *91*, 146401–1464014.

[127] A. Klamt, G. Schüürmann, *J. Chem. Soc., Perkin Trans. 2* **1993**, 799–805.

[128] S. Sinnecker, A. Rajendran, A. Klamt, M. Diedenhofen, F. Neese, *J. Phys. Chem. A* **2006**, *110*, 2235–2245.

[129] A. Klamt, M. Diedenhofen, *J. Phys. Chem. A* **2015**, *119*, 5439–5445.

[130] A. E. Ozel, S. Akyuz, *J. Struct. Chem.* **2005**, *46*, 1077−1081.

[131] N. Sun, L. V. Liu, A. Dey, G. Villar-Acevedo, J. A. Kovacs, M. Y. Darensbourg, K. O. Hodgson, B. Hedman, E. I. Solomon, *Inorg. Chem.* **2011**, *50*, 427–436.

[132] S. I. Gorelsky, AOMix 2.8: *Program for Molecular Orbital Analysis*, **1997**–**2013**.

[133] S. I. Gorelsky, A. B. P. Lever, *J. Organomet. Chem.* **2001**, *635*, 187–196.

[134] R. S. Mulliken, *J. Chem. Phys.* **1955**, *23*, 1833–1840.

[135] A. E. Reed, R. B. Weinstock, F. Weinhold, *J. Chem. Phys.* **1985**, *83*, 735–746.

[136] F. Cortés-Guzmán, R. F. W. Bader, *Coord. Chem. Rev.* **2005**, *249*, 633–662.

[137] T. Lu, F. Chen, *J. Comput. Chem.* **2012**, *33*, 580–592.

[138] S. Sinnecker, F. Neese, L. Noodleman, W. Lubitz, *J. Am. Chem. Soc.* **2004**, *126*, 2613–2622.

[139] C. van Wüllen, *J. Phys. Chem. A* **2009**, *113*, 11535–11540.

[140] T. Soda, Y. Kitagawa, T. Onishi, Y. Takano, Y. Shigeta, H. Nagao, Y. Yoshioka, K. Yamaguchi, *Chem. Phys. Lett.* **2000**, *319*, 223–230.

[141] E. Runge, E. K. U. Gross, *Phys. Rev. Lett.* **1984**, *52*, 997–1000.

[142] N. Clark, A. Martell, *Inorg. Chem.* **1988**, *27*, 1297–1298.

[143] K. Micskei, *J. Chem. Soc., Dalton Trans.* **1987**, 255–257.

[144] F. R. Fronczek, S. N. Collins, J.-Y. Chan, *Acta Crystallogr., Sect. E* **2001**, *57*, i26–i27.

[145] J. K. Beattie, S. P. Best, B. W. Skelton, A. H. White, *J. Chem. Soc., Dalton Trans.* **1981**, 2105–2111.

[146] A. Grirrane, A. Pastor, C. Mealli, A. Ienco, P. Rosa, R. Prado-Gotor, A. Galindo, *Inorg. Chim. Acta* **2004**, *357*, 4215–4219.

[147] A. K. Powell, J. M. Charnock, A. C. Flood, C. D. Garner, M. J. Ware, W. Clegg, *J. Chem. Soc., Dalt. Trans.* **1992**, 203–207.

[148] K. A. Abboud, C. Xu, R. S. Drago, *Acta Crystallogr. Sect. C Cryst. Struct. Commun.* **1998**, *54*, 1270–1273.

[149] R. Meier, F. W. Heinemann, *Inorg. Chim. Acta* **2002**, *337*, 317–327.

[150] H.-M. Huang, H.-B. Yang, X.-Y. Li, F.-F. Ren, *Acta Crystallogr. Sect. E* **2009**, *65*, m87–m88.

[151] R. Shannon, *Acta Crystallogr., Sect. A* **1976**, *32*, 751–767.

[152] B. M. Aas, *{FeNO}^{7}-Nitrosyleisen-Verbindungen vom „braune-Ring"-Typ*, Master's thesis, LMU Munich, **2013–2014**.

[153] T. Mizuta, J. Wang, K. Miyoshi, *Bull. Chem. Soc. Jpn.* **1993**, *66*, 2547–2551.

[154] T. Mizuta, J. Wang, K. Miyoshi, *Inorg. Chim. Acta* **1995**, *230*, 119–125.

[155] M. D. Clay, C. a Cosper, F. E. Jenney, M. W. W. Adams, M. K. Johnson, *PNAS* **2003**, *100*, 3796–3801.

[156] Y. Jiang, T. Hayashi, H. Matsumura, L. H. Do, A. Majumdar, S. J. Lippard, P. Moënne-Loccoz, *J. Am. Chem. Soc.* **2014**, *136*, 12524–12527.

[157] S. Lu, E. Libby, L. Saleh, G. Xing, J. M. Bollinger, P. Moënne-Loccoz, *J Biol Inorg Chem* **2004**, *9*, 818–827.

[158] Mestrelab Research S.L., *MestReNova 8.1.1-11591*, Santiago de Compostela, ESP, **2013**.

[159] JASCO Corporation, *Spectra Manager 2.07.00*, **2002–2008**.

[160] Origin Pro V8.5.1, *Data Analysis and Graphing Software*, **1991−2011**.

[161] G. M. Sheldrick, *Acta Crystallogr. Sect. A* **2008**, *64*, 112–122.

[162] G. M. Sheldrick, *Acta Crystallogr. Sect. C* **2015**, *71*, 3–8.

[163] C. B. Hübschle, G. M. Sheldrick, B. Dittrich, *J. Appl. Crystallogr.* **2011**, *44*, 1281–1284.

[164] C. F. Macrae, P. R. Edgington, P. McCabe, E. Pidcock, G. P. Shields, R. Taylor, M. Towler, J. Van De Streek, *J. Appl. Crystallogr.* **2006**, *39*, 453–457.

[165] C. F. Macrae, I. J. Bruno, J. A. Chisholm, P. R. Edgington, P. McCabe, E. Pidcock, L. Rodriguez-Monge, R. Taylor, J. Van De Streek, P. A. Wood, *J. Appl. Crystallogr.* **2008**, *41*, 466–470.

[166] L. J. Farrugia, *J. Appl. Crystallogr.* **2012**, *45*, 849–854.

[167] E. Keller, *SCHAKAL99: A Fortran Program for the Graphical Representation of Molecular and Crystallographic Models*, **1999**.

[168] K. S. Hagen, *Inorg. Chem.* **2000**, *39*, 5867–5869.

[169] B. Spingler, S. Schnidrig, T. Todorova, F. Wild, *CrystEngComm* **2012**, *14*, 751–757.

[170] *TURBOMOLE V6.6 2014*, a development of University of Karlsruhe and Forschungszentrum Karlsruhe GmbH, **1989–2007**, TURBOMOLE GmbH, since 2007; available from http://www.turbomole.com.

[171] R. Ahlrichs, M. Bär, M. Häser, H. Horn, C. Kölmel, *Chem. Phys. Lett.* **1989**, *162*, 165–169.

[172] COSMOlogic GmbH & Co. KG, *TmoleX 4.0.1*, Leverkusen, GER, **2014**.

[173] C. Steffen, K. Thomas, U. Huniar, A. Hellweg, O. Rubner, A. Schroer, *J. Comput. Chem.* **2010**, *31*, 2967–2970.

[174] S. Grimme, S. Ehrlich, L. Goerigk, *J. Comput. Chem.* **2011**, *32*, 1456–1465.

[175] F. Neese, *Wiley Interdiscip. Rev. Comput. Mol. Sci.* **2012**, *2*, 73–78.

Publikationen:

B. M. Aas, D. Beck, L. J. Daumann: Mehr als nicht unschuldig – NO in der Bioanorganik, *Nachr. Chem.* **2018**, *66*, 114–117, DOI:10.1002/nadc.20184070506.

B. M. Aas, P. Klüfers: The Structural Chemistry of Stable High-Spin Nitrosyl–Iron(II) Compounds with Aminecarboxylato Co-Ligands in Aqueous Solution, *Eur. J. Inorg. Chem.* **2017**, *17*, 2313–2320, DOI: 10.1002/ejic.201601330.

M. Wolf, B. M. Aas, P. Klüfers; Front Cover: High-Spin Nitrosyl–Iron(II) Compounds, *Eur. J. Inorg. Chem*. **2017**, *17*, 2301, DOI: 10.1002/ejic.201700382.

Poster:

B. M. Aas, P. Klüfers: Strukturchemie stabiler *high-spin*-Nitrosyleisen-Verbindungen mit Amincarboxylaten in wässriger Lösung, *13. Koordinationschemie-Treffen* **2017**, Potsdam.

B. M. Aas, A. In-Iam, P. Klüfers: In Multiphase Reaction Media – *in-situ* Characterizable Nitrosyl Iron Complexes with Controllable Reactivity, *Jahreskolloquium DFG SPP 1740 „Reaktive Blasenströmungen“* **2016**, Berlin.

B. M. Aas, A. In-Iam, P. Klüfers: In Multiphase Reaction Media – *in-situ* Characterizable Nitrosyl Iron Complexes with Controllable Reactivity, *Jahreskolloquium DFG SPP 1740 „Reaktive Blasenströmungen“* **2015,** Hamburg-Harburg.

Vorträge:

B. M. Aas, P. Klüfers: In Multiphase Reaction Media – *in-situ* Characterizable Nitrosyl Iron Complexes with Controllable Reactivity, *Jahreskolloquium DFG SPP 1740 „Reaktive Blasenströmungen“* **2015,** Hamburg-Harburg.

B. M. Aas, P. Klüfers: Fe–NO-Complexes in Multiphase Flows, *Workshop „Chemical Reaction Systems“ DFG SPP 1740 „Reaktive Blasenströmungen“* **2014**, München.

An dieser Stelle möchte ich allen danken, die mich im Laufe meiner Promotion begleitet haben und ohne die diese Arbeit nicht möglich gewesen wäre:

Ich bedanke mich bei meinem Doktorvater Herrn Prof. Dr. Peter Klüfers für die herzliche Aufnahme in seinen Arbeitskreis, die interessante Themenstellung sowie für die ausgezeichnete Betreuung und die zahlreichen Diskussionen auf dem Gebiet der Nitrosyleisen-Chemie.

Weiterhin bin ich Herrn Prof. Dr. Hans-Christian Böttcher zu großem Dank verplichtet. Nicht nur für die Übernahme des Zweitgutachtens, sondern auch für seine stets freundliche und hilfsbereite Art.

Für Ihre Mitwirkung in der Promotionskommission danke ich Prof. Dr. Lena Daumann, Prof. Dr. Konstantin Karaghiosoff, Prof. Dr. Achim Hartschuh und Prof. Dr. Wolfgang Beck.

Lida Holowatyi-den Toom danke ich für die unermüdliche Hilfe bei allen organisatorischen Dingen, das Korrekturlesen der vorliegenden Arbeit und meiner Publikation sowie für ihre lustige und zuvorkommende Art.

Christine Neumann danke ich für den steten Nachschub an Laborgeräten sowie für die zahlreichen nützlichen Tipps zu diversen chemischen Arbeitstechniken.

Ich danke der DFG für die finanzielle Unterstützung im Rahmen des SPP1740. Den Koordinatoren in diesem Schwerpunktprogram danke ich für die einwandfreie Organisation sämtlicher Zusammentreffen. Bei Daniela und Katharina möchte ich mich außerdem für die schöne ingenieurstechnische Zusammenarbeit bedanken, die es mir ermöglicht hat, etwas über meinen „chemischen Tellerrand“ hinaus zu schauen.

Dr. Markus Wolf danke ich für die Einführung in das Gebiet der Nitrosyleisen-Verbindungen und in die anfänglich etwas verwirrende Welt der DFT Rechnungen.

Weiterhin bedanke ich mich bei den fleißigen Korrekturlesern meiner Arbeit: Dr. Markus Wolf, Sebastian Brück, Helen Funk, Areenan In-Iam, Tobias Riggenmann, Dr. Anna Gallien, Daniel Beck, Dr. Anja Belz und Dr. Andreas Peruf.

Allen Mitgliedern des Arbeitskreises, die ich während meiner Promotion kennen lernen durfte, danke ich für die immerwährende hilfsbereite und freundschaftliche Atmosphäre und für die lustige und schöne Zeit auch außerhalb des Labors. Besonderer Dank geht dabei an meine Laborkollegen Dr. Xaver Wurzenberger, Georg Monsch, Jan Heinemann, Christine Neumann und Areenan In-Iam.

Dem Analytik-Team möchte ich für die Messung meiner Proben danken. Außerdem danke ich Herrn Dr. Peter Mayer, Sandra Albrecht, Dr. Anja Belz, Dr. Christine Sturm, Areenan In-Iam, Daniel Beck und Helen Funk für die röntgenkristallographischen Messungen meiner Kristalle.

Herzlichen Dank auch an meine Praktikanten Christina Buchecker, Lukas Brunner, Patrick Grassl und Kerstin Rickmeyer für ihre gewissenhafte und fleißige Mitarbeit.

Meiner „Chemie-Schwester“ Laura Ascherl danke ich für die schöne gemeinsame Zeit während des Studiums und der Promotion.

Meiner Familie, insbesondere meinem Papa, danke ich für die bedingungslose Unterstützung auf dem Weg zu dieser Dissertation.

Meinem Freund Herrn Dr. Andreas Peruf danke ich für die wunderschönen letzten acht Jahre. Ohne dich wäre das alles nicht möglich gewesen. Ich freue mich auf unsere gemeinsame Zukunft.